Aviation Emission Inventory

A contemporized bottom-up emission inventory for the year 2019

Delft University of Technology

Rik Kroon

Delft University of Technology

TU Delft

Aviation Emission Inventory

A contemporized bottom-up emission inventory for the year 2019

by

Rik Kroon

in partial fulfillment of the requirements
for the degree of Master of Science
at the Delft University of Technology,
to be defended publicly on Wednesday December 7, 2022 at 14.00 PM.

Student number: 4644220

Thesis Committee:

Prof. Dr. V. Grewe	TU Delft/DLR, chair
Prof. Dr. A. Gangoli Rao	TU Delft, supervisor
Dr. F. Yin	TU Delft, supervisor

Cover Image: 747 with visible emissions (obtained from insideclimatenews.org)

TU Delft

Abstract

This report covers all major steps to establish an aviation emission inventory for 2019. This emission inventory is set up based on four consecutive steps. The first step is to gather all required data in the information model and this also includes some pre-processing of data to make it as complete as possible. The second step is to estimate the point performance of the aircraft at multiple waypoints along the trajectory based on the Base of Aircraft Data (BADA). This also allows for fuel consumption estimation. The third step uses the point performance data to estimate emissions under the respective flight condition. The last step addresses introduced uncertainties based on the different models. From a first principle perspective the uncertainty on a fleet wide scale (and for short and long haul flights) is found concerning the fuel consumption and various emission species (for example nitrogen oxides and carbon monoxide) using a Monte Carlo simulation.

The trajectory data is obtained from *flightradar24* in which gaps were identified where the type of aircraft, origin airport or destination airport were missing. Complementing of the database is based around the provided flight numbers and call signs. Based on airline data a variety of assumptions is made relating to payload fraction (69%) and increase in flight distance (8%) compared to the great circle distance. The trajectory is estimated using the rate of climb and descent provided in BADA. The emission model then uses constant emission indices, the boeing fuel flow method 2 (BFFM2) and the DLR method to compute all emissions according to:

- Constant emission index: carbon dioxide (corrected for emission index of carbon monoxide), water vapor and sulfur oxide.
- BFFM2: carbon monoxide, unburned hydrocarbons and nitrogen oxides.
- DLR: black carbon emission.

The uncertainty analysis, finally, covers airline operational uncertainty, model uncertainty and engine aging uncertainty to find an average increase in fuel consumption of 4.2%. Due to the influence of fuel flow, other emission species are increased with a different fraction.

Due to computational limitations it has been decided to analyze one week, which will be representative of the entire year. Based on this analysis an annual fuel consumption of $272\ Tg$ is simulated with corresponding carbon dioxide emission of $857\ Tg$. In addition, a nitrogen oxide emission of $5.3\ Tg$ is found. All emission species are mainly emitted on the northern hemisphere on three geographical locations: north America, Europe and south-east Asia. The strongest recommendation is to include military flights and non-jet aircraft in the analysis (mainly turboprop aircraft). In addition, to decrease the dependency on data of a single week, it is advised to obtain more computational power to allow for analysis of multiple representative weeks preferably in both ICAO specified seasons.

Finally it is recommended to extend the uncertainty analysis to cover more individual uncertainties such as the uncertainty in cruise altitude (based on airline routing) and to find more research on the uncertainty of sulfur content in kerosene.

Acknowledgements

With the completion of this thesis a fantastic time has come to an end at Delft University of Technology. A time where the university, and its academic staff, have shaped me both as a person and as an engineer. Even though the last few years have not been easy due to the influence of the covid pandemic, I am very grateful for all the provided opportunities.

Most important of all, I would like to extend my gratitude to my daily supervisors: Prof. Dr. A. Gangoli Rao and Dr. F. Yin. From the very beginning of this thesis I felt encouraged and inspired by their vision on this topic. In addition, from the very first meeting, the confidence they have placed in me has provided me with substantial freedom which has been an invaluable asset in conducting this thesis.

In addition, I would like to thank my brother, sister and my parents for their continuous support, both concerning the thesis work and on a personal level. Without their trust and backing, motivation to conduct all academic work would have been lacking.

Lastly, I would like to thank all friends from Delft, and outside of it, for the interesting discussions, the relaxing nights out when necessary and their indispensable support.

Rik Kroon
Delft, November 2022

Contents

Nomenclature

Abbreviations

Abbreviation	Definition
AIC	Aircraft-incuded Cloudiness
AEM	Advanced Emission Model
BADA	Base of Aircraft Data
BC	Black carbon
BFFM2	Boeing Fuel Flow Method 2
CCD	Climb, cruise and descent
CI	Confidence Interval
CO	Carbon monoxide
CO_2	Carbon dioxide
DLR	Deutsches Zentrum für Luft- und Raumfahrt
EASA	European Union Aviation Safety Agency
EEA	European Environment Agency
EIA	Energy Information Administration
ESF	Energy Share Factor
FAA	Federal Aviation Administration
FOA	First Order Approximation
HC	Unburned hydrocarbons
H_2O	Water vapor
IATA	International Air Transport Association
ICAO	International Civil Aviation Organization
IPCC	Intergovernmental Panel on Climate Change
ISA	International Standard Atmosphere
LTO	Landing and Take-Off
MIT	Massachusetts Institute of Technology
NO_x	Nitrogen oxides
NVPM	Non-volatile particulate matter
OAG	Official Airline Guide
O_{3s}	Long lived ozone
O_{3s}	Short lived ozone
PDF	Probability Density Function
PTF	Performance Table File
RQL	Rich-burn/Quick-mix/Lean-burn
SO_x	Sulfur oxides
TEM	Total Energy Method
US	United States

Symbols

Symbol	Definition	Unit
a	Variable for statistical distributions	[-]
b	Variable for statistical distributions	[-]
c	Variable for statistical distributions	[-]
C	Concentration	[ppm]
d	Distance	[nm]

Symbol	Definition	Unit
D	Drag	[N]
E	Expectation	[-]
EI	Emission Index	[kg/kg]
f_{BC}	Black carbon multiplication factor	[-]
f_{empty}	Fraction relating MTOM and OEM	[-]
$\frac{F}{F_{00}}$	Thrust setting	[-]
$f_{payload}$	Fraction relating actual payload mass and maximum payload mass	[-]
g_0	Gravitational acceleration	[m/s^2]
h	Altitude	[ft]
H	Parameter for Boeing Fuel Flow Method 2 associated with humidity	[-]
l	Left border of domain	[-]
LHV_{fuel}	Lower Heating Value kerosene	[MJ/kg]
m	Mass	[kg]
m	Mode	[-]
M	Mach number	[-]
$MTOM$	Maximum Take-Off Mass	[kg]
$MZFM$	Maximum Zero Fuel Mass	[kg]
$\dot{m}$	Mass flow	[kg/s]
n	Number of simulations	[-]
$n_{particles}$	Number of particles per gram black carbon	[$/g$]
OEM	Operating Empty Mass	[kg]
P	Pressure	[Pa]
pH	Aciditiy level	[-]
P_v	Saturated vapor pressure	[Pa]
P_3	Combustor inlet pressure	[Pa]
$\dot{Q}$	Volumetric flow rate per unit mass of fuel	[m^3/kgs]
r	Right border of domain	[-]
REI	Reference Emission Index	[kg/kg]
RF	Radiative Forcing	[W/m^2]
ROC	Rate Of Climb	[ft/min]
$ROCD$	Rate Of Climb/Descent	[ft/min]
ROD	Rate Of Descent	[ft/min]
RPK	Revenue Passenger Kilometer	[$px \cdot km$]
SAR	Specific Air Range	[km]
$s_i(h)$	Forcing factor	[W/m^2]
SN	Smoke Number	[-]
t	Time	[s]
T	Temperature	[$^\circ$]
TAS	True Air Speed	[kts]
T_{fl}	Flame temperature	[K]
Th	Thrust	[N]
TOM	Take-off Mass	[kg]
$TSFC$	Thrust Specific Fuel Consumption	[g/kNs]
T_3	Combustor inlet temperature	[K]
Var	Variance	[-]
W_f	Fuel flow at considered altitude	[kg/s]
W_{ff}	Fuel flow at sea level	[kg/s]
x	Denotation of a certain species	[-]
x	Variable for statistical distributions	[-]
X	Random variable	[-]
$\bar{x}$	Mean multiplier	[-]

Symbol	Definition	Unit
$z_{critvalue}$	Statistical variable related to the required confidence interval	[-]
β	Bypass ratio for mixed turbofan engines	[-]
β	Parameter associated with calculation of saturated vapor pressure	[-]
γ	Adiabatic index	[-]
δ	Ratio of temperature	[-]
$\eta_{acceleration}$	Efficiency related to aircraft acceleration	[-]
η_{comp}	Compressor isentropic efficiency	[-]
θ	Ratio of pressure	[-]
μ	Mean	[-]
π	Engine overall pressure ratio	[-]
σ	Standard deviation	[-]
ϕ	Equivalence ratio	[-]
ϕ	Relative humidity	[-]
ω	Specific humidity	[-]

List of Figures

List of Tables

1

Introduction

The aviation industry has been one of the fastest growing transportation industries, growing from 109 billion revenue passenger kilometer (RPK) per year in 1960 to 8269 billion RPK per year in 2018 [1]. This growth has been synonymous with an increase in anthropogenic climate impact as the increases in efficiency do not outweigh the growth of the sector. With other (also non-transport) sectors starting to become more sustainable, the percentual share of aviation emissions is expected to increase significantly to 22% in 2050 [2]. To model the emissions of aviation, the concept of emission inventories has been developed: emission inventories estimate the emission of, in this case, aviation by means of trajectory estimation and point/trajectory performance estimation. For aviation in particular the applied methodology is of great importance as the emission altitude and geographic location significantly affect the climatological impact of the emission species [3]. The objective of this thesis is therefore to develop a comprehensive model which allows the capture of three dimensional emission information to allow scientists to draw climatological impact assessment conclusions.

One comprehensive emission inventory for the year 2005 that has been conducted is a study at MIT by N.W. Simone in 2013 [4]. Simone predicts an annual fuel consumption of $180.6\ Tg$ with 90% confidence between $136.1 - 232.9\ Tg$. This is considered a very large uncertainty and prevents politicians to create effective climate legislation as the scale of emissions is very uncertain. In addition, this uncertainty in fuel consumption imposes additional uncertainty on all emission species as they are all strongly dependent on the fuel consumption. It is therefore essential to decrease the uncertainty associated with the fuel burn. The resultant fuel burn from Simone 2013's study, geographically, is presented in Figure 1.1. The figure shows that most fuel is burned in three locations: north America, Europe and south-east Asia with routes between these locations showing significant fuel burn as well.

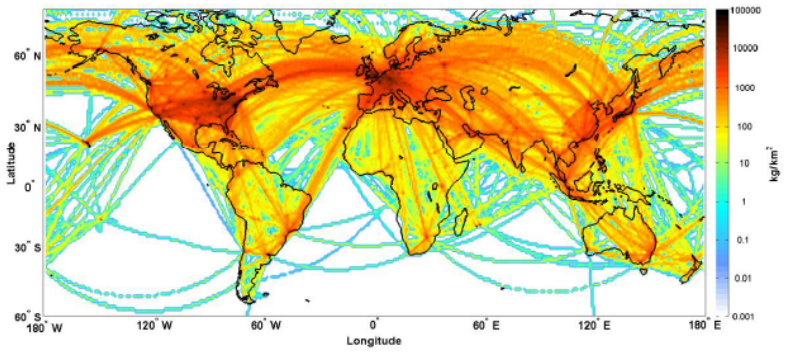

Figure 1.1: Global fuel burn from scheduled civil aviation in 2005 (figure obtained from *Development of a Rapid Global Aircraft Emissions Estimation Tool with Uncertainty Quantification* [4]).

For various emission species the location of emission, both vertical and lateral, affects the climate/air quality. Various species, such as nitrogen oxides [5], have an ecological/local air quality impact close to the location of emission. In addition, due to, historically, relative recent increases in prosperity in Asia, the emission distribution in Figure 1.1 tends to change significantly over time as prosperity is closely correlated to the number of flight movements [6]. Such change consequently affects the associated local and global impact of emissions. It is therefore important to keep aviation emission inventories as up-to-date as possible.

The objective of this research is to create an updated emission inventory for climate assessment of aviation using new and updated methods to model aircraft and engine performance. To fulfill this objective the following research question is formulated: How can current aviation emission inventories be improved and, consequentially, what are the updated aviation emission inventories for different air traffic scenarios taking into account different aircraft categories? To answer this main question, three research sub-questions are formulated:

- What research can be used off the shelf and be complemented by this research in order to increase reliability of the data?
- How can the uncertainty analysis be improved and the confidence in the results be increased?
- Taking into account the updated emission inventory model, what are the quantity and distribution of emissions of aviation?

This report is structured as follows. Chapter 2 describes the information required as a starting point for emission inventory assessment. Chapter 3 presents the applied methodology to estimate point performance (such as fuel consumption at waypoints along a flight trajectory) and flight trajectory. In addition the fuel flows and ambient conditions estimated by the trajectory calculation are a starting point for the emission prediction. Then, in Chapter 4, the methodology to estimate emissions at every way point of the flight is outlined. After that, in Chapter 5, the uncertainty analysis is performed starting from a simplified physical basis until the overall uncertainty has been found. This chapter is concluded by showing the result of all individual uncertainties combined. Following is Chapter 6, which presents the verification and validation of all applied models and uncertainties. The penultimate chapter, Chapter 7, provides all results of the applied methods and makes a direct comparison to previous emission inventories and fuel sales. Finally, a conclusion is drawn and a critical reflection on this research is presented in Chapter 8.

2

Information model

The information model captures the foundation of an emission inventory. For the purpose of this emission inventory data has been obtained from *flightradar24*[1]. Amongst others, the most important data captured are: the departure airport, the arrival airport and the type of aircraft. Unfortunately, no four dimensional data points along the route are provided, hence no intermediate speeds or altitudes can be computed [7].

2.1. Structure of the emission inventory

To fully understand all elements of the emission inventory a short overview is presented in this section. This section thus aims to present the underlying structure of Chapter 2, Chapter 3, Chapter 4 and Chapter 5. The emission inventory is composed of four elements (similar to work performed by Simone et al. [4], C. J. Eyers et al. [7], S.L. Baughcum et al. [8], W. Fan et al. [9], D.K. Wasiuk et al. [10], J. Li et al. [11] and B. Owen et al. [12]):

- **Information model:** the information model brings all the information required for the analysis. On a per-flight-basis the bare minimum required elements are the departure point, the arrival point and the type of aircraft.
- **Performance model:** the performance model uses the data from the information model to estimate the point performance at every point of the trajectory. This trajectory, in turn, is modelled as the great circle distance corrected with the en-route multiplier: the fractual increase in travelled distance compared to the great circle distance. Based on these point performances an estimation can be made on the fuel consumption of the complete flight. The estimation starts with point performance estimation at the departure point for the landing and take-off (LTO) segment until climbout has finished at $3000\ ft$ above the elevation of the departure airport. The actual flight segment then starts which finishes $3000\ ft$ above the elevation of the arrival airport. Similarly, the LTO segment at the arrival airport is then computed. The performance model requires many assumptions, such as the payload factor and the increase in distance compared to the great circle distance.
- **Emission model:** the emission model uses the estimated flight trajectory and point performance to find the associated emissions of all flight phases. Some emission calculations are easy as they are directly proportional to the fuel burn (such as carbon dioxide and water vapor), while other emission species are largely dependent on thrust settings and ambient conditions (such as nitrogen oxides and carbon monoxide). The LTO emissions can be obtained from the ICAO emission databank, however the in-flight emissions require estimation. Various models are required for this analysis to use sea level emission data and extrapolate it to the required atmospheric conditions [13].
- **Uncertainty analysis:** the uncertainty analysis should capture all uncertainties associated with the used models, the origin of the data and the choices made during this thesis. Intuitively, the aim is to minimize the uncertainties. Uncertainty analysis for aviation emission inventories has been performed before, but the obtained uncertainties were rather large. Fur-

[1] `https://www.flightradar24.com/` (accessed 05-09-2022)

thermore, this research from 2005 (by Lee et al. [14]) is considered dated.

Note that these models are highly integrated with one another. A simplified schematic of this process is presented in Figure 2.1. Please note that an elaborate version is presented later as more insight is provided in the individual elements.

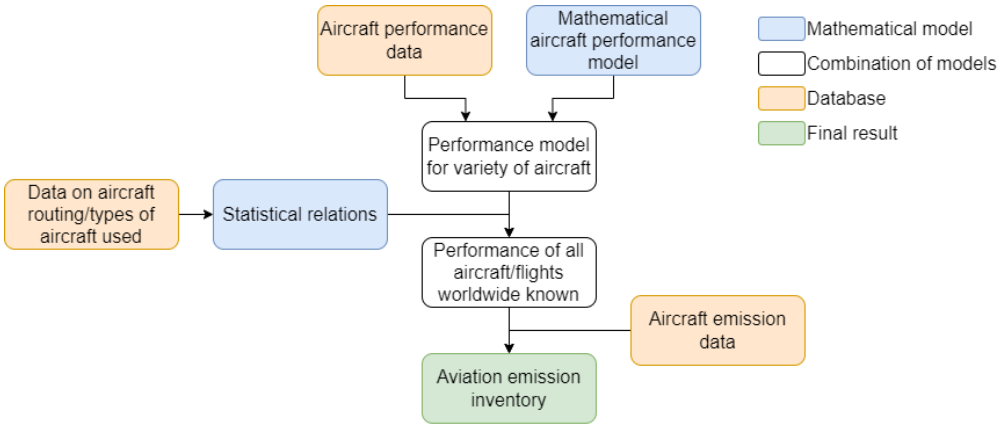

Figure 2.1: Basic flow chart of the various elements of an aviation emission inventory.

2.2. Types of aircraft

Before more information is presented about databases, it is important to understand what type of aviation can be modelled. In general, four types of aviation are distinguished, which can be subdivided in other categories as well [7]:

- Military aviation: military helicopters, cargo planes and fighter jets.
- General aviation: piston aircraft with no more than 10 seats.
- Private aviation (private jets): business jets with no more than 20 seats often powered by turbofan or turbojet engines.
- Commercial aviation:
  - Turboprops: aircraft powered by at least two turboprop engines.
  - Regional jets: jets powered by turbofan or turbojet engines with no more than 100 seats.
  - Large jets: the majority of commercial aviation, these aircraft fly longer distances with at least 100 seats.

Quantifying military aviation emissions is a difficult process due to the lack of reliable military aviation trajectory information and the lack of data on emissions of military engines [15]. In the US the military is responsible for a decreasing fraction of fossil fuel use [15] but, as of 2009, about 20% of jet fuel in the US is consumed by military aircraft [16]. The main reason for the fractional decrease is the closing of marine/air force bases [15]. Waitz et al. [15], however, argue that the main impacts of military aviation are noise related, rather than emission related. It is decided to compute military aviation emissions in the same way as for civil aviation where information is provided. As there is not enough information available, these flights by military aircraft will not be taken into account (as many military flights are not recorded by *flightradar24* [17]).

Emissions of general aviation are easier to compute as the flights are tracked by *flightradar24*. Unfortunately, this will be shown later in the report, the database governing engine emissions does not cover piston engines. This means that emission estimation for these aircraft is not possible. In addition, *opensky* provides a similar database compared to *flightradar24* and in this database it is found that only 6% [18] of the flights are made up of general aviation. Therefore, not taking these flights into account does not create a significant uncertainty due to the fact that the emissions will make up a far smaller fraction than the 6% because of the smaller emission impact of these aircraft.

Business jets are often based on commercial aircraft (from Boeing, Airbus, Bombardier and Embraer website), this allows one to use databases of the regular airliners. Furthermore, the family

of engines used on these aircraft are covered by the required databases as they need to be certified for civil aviation. Business jets can therefore be covered in a similar way as the rest of the jets.

Lastly, turboprops cannot be modelled using the associated emission database as the ICAO emission databank is limited to jet engines. These turboprop engines are often smaller aircraft and do not make up a significant part of emissions in most recent Eurocontrol estimations [19].

2.3. Database

As briefly mentioned previously, the database of flights is obtained from *flightradar24*. This database contains roughly 52 million flights per annual which is a too large number for all flights to be analyzed. For this purpose the concept of representative weeks is introduced: a representative week is a seven day period for which the characteristics of all flights in this week is representative for a longer period of time. Logically, increasing the number of representative weeks, thus making every week responsible for a part of the year, increases the computational time significantly.

2.3.1. Requirements for the representative week

Several requirements are put forward to which the representative week must adhere to:

- The representative week shall not occur in a holiday period (i.e. summer on the northern hemisphere or holiday period end of December/beginning of January).
- The mean number of flight movements throughout the year shall be as close as possible (without violating any of the other requirements) to the number of flights in the representative week.
- The representative week shall not be taken from a week where a switch is made between summer and winter schedules for airlines (according to IATA[2] summer schedule starts last Sunday of March until the last Saturday of October) as this provides a too large fluctuation in traffic patterns for the rest of the requirements to uphold.

2.3.2. Daily traffic variation

Commercial daily aviation demand varies widely throughout the year. In order to find a representative week for the entire year, a good overview of the traffic variation is required. The number of daily commercial aircraft movements is presented in Figure 2.2. Note that this is the 7-day moving average. Only commercial flights were used for this analysis. The underlying reason for this decision is that the majority of emissions is caused by commercial aviation according to Eurocontrol [19].

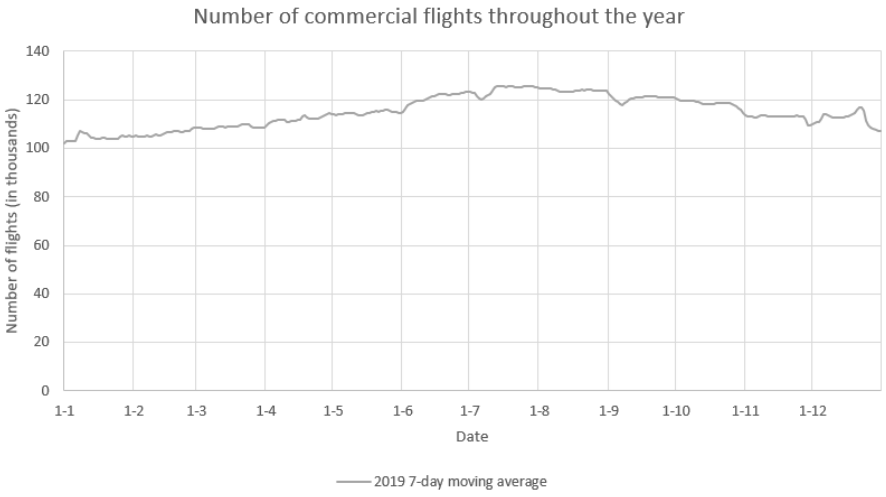

Figure 2.2: 7-day-moving-average of daily commercial flights worldwide (based on *flightradar24* data).

Note that strong variations in traffic can occur in a week within the same month (such as during

[2] `https://www.iata.org/` (accessed 05-09-2022)

Christmas, around the beginning of July and the end of August). The variations over the entire year are not very large, with minimum number of commercial daily movements of 100,000 beginning of January and maximum of 125,000 halfway July. Preferably, based on the above diagram, the representative week(s) should not be chosen at minimum or maximum traffic, i.e. not from January, June, July and August.

2.3.3. Number of flights per month

In order to identify the representative week, an overview of the number of commercial flights per month is presented in Table 2.1 with their representative share compared to the total number of commercial flights in the year 2019.

Table 2.1: Number of commercial flights per month in 2019 (based on *flightradar24* data).

Month	Number of commercial flights 2019	Percentage of total [%]
January	$3,237,745$	7.71
February	$2,971,193$	7.08
March	$3,372,054$	8.03
April	$3,362,958$	8.01
May	$3,553,438$	8.47
June	$3,625,576$	8.64
July	$3,848,744$	9.17
August	$3,842,034$	9.15
September	$3,617,796$	8.62
October	$3,674,918$	8.76
November	$3,386,662$	8.07
December	$3,476,720$	8.28
Total	$41,969,838$	100

From both figures (Figure 2.2 and Table 2.1) a strong demand is observed during June, July and August. This demand is followed by a small reduction in demand in the months September and October. The end of the year then shows a peak in demand due to the Christmas/New Year holiday. The least popular period then follows in February. This trend is roughly similar every year, although the presented data is limited to the year of 2019 as this is the year under investigation in this thesis.

2.3.4. Selection of representative week

In order to gain an understanding of the variation of commercial flight movements throughout the year, Figure 2.3 is presented. Please note that only the weeks which were completely in 2019 are presented. In other words, none of the weeks contain a day on which New Year's Eve took place which is why the total number of occurrences sums up to 51 weeks.

In addition to the data provided in Figure 2.3 the mean and median of all data is presented in Table 2.2. Based on an analysis of all commercial flights in 2019 per week and on the formulated requirements, week 21 of 2019 is chosen (Monday May 20 - Sunday May 26) as the only representative week for computational purposes. The number of commercial flights in this week is also presented in the table.

Table 2.2: Statistics on commercial flight weeks in 2019.

Parameter	Value
Mean	$806,631$
Median	$800,627$
Number of commercial flights chosen week	$808,637$

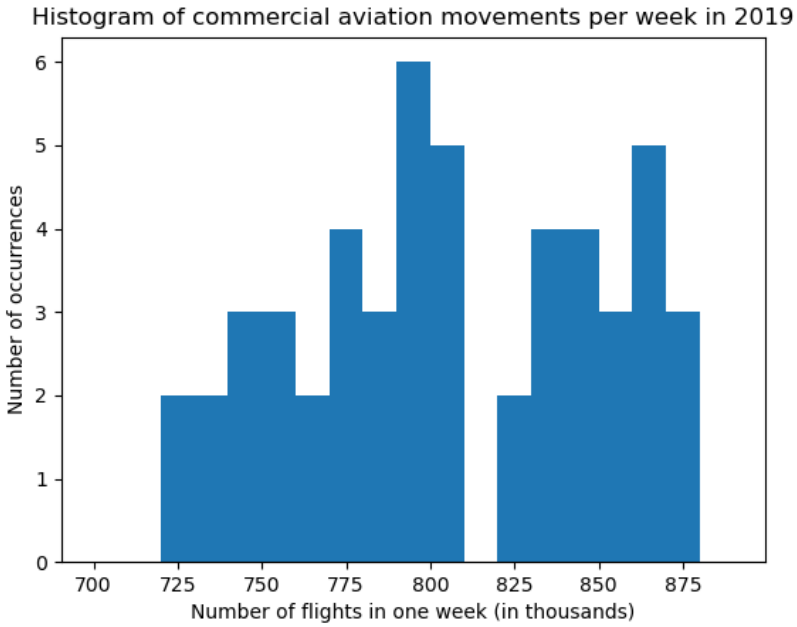

Figure 2.3: Histogram of number of commercial flights in a full week in 2019.

2.4. Incompleteness of database

Visually checking data in the database, it has been found that some information, including absolutely required information such as aircraft type, departure airport and arrival airport, are missing. A methodology is set up to complement the database. First, a database program is selected to be able to analyze all flights quickly. The selected program is *sqlite3*[3] since it functions well within the *Python* environment. Since *Python* will also be used for the other models this is of predominant importance. Three elements are required for the analysis of a single flight: departure airport, arrival airport and the aircraft type. Complementation of the database is thus focused on obtaining these three elements for every single flight. A flowchart of the process is presented in Figure 2.4 after which a thorough explanation of it is provided.

The first step is to convert all files to the required format (.db file). This file is duplicated and renamed. This duplicated file will function as the file which contains all data for the representative week. This is hence also the first step, to delete all lines which are not within the bounds of the representative week.
The next step is to delete all lines where no required data (including flight number) is available. In other instances, the flight number will be used to complement data from similar flights in the database but if this is unavailable this is not possible.
Next, the flights where the origin and the destination are the same airport are deleted. For these flights no estimation can be made about the length of the flight. A visual check also shows that these flights are mainly general aviation flights for which the emission is not considered substantial (as mentioned previously in the report of Eurocontrol).
Complementation of the representative week database is then initiated. Based on the three required elements various scenarios for the data of a single flight are available:

- **All data is complete**: no action is taken and next flight is selected.
- **No required data is available**: based on the flight number the first flight where all required data is available is selected and complemented to the required line.
- **Departure and destination airports not available**: based on the flight number and the aircraft type the first instance of the combination is used to complement the original line.
- **Aircraft type not available**: the flight number is used to find a similar flight from which the

[3] `https://docs.python.org/3/library/sqlite3.html` (accessed 11-11-2022)

aircraft type is deduced.
- **Arrival airport not available**: the flight number and departure airport are used to find the arrival airport. The reason the departure airport is also used is that triangle flights often use the same flight number for the three stretches of flight [20].
- **Departure airport not available**: the flight number and arrival airport are used to find the departure airport. The line of reasoning is the same as mentioned in the previous point.

Note that a combination of the above (such as type of aircraft and departure airport missing) can also occur. This is also taken into account by the program and both are complemented if possible. If no similar flight is found, the data will remain the same and will not be altered.
The last step is, again, to delete the lines where the origin and destination are the same.

Visually checking the database it can be seen that on the 'borders', i.e. the switch from one day to the other, *flightradar24* causes some confusion. There is no 'hard' border meaning that flights from the previous day and the current day are mixed around for thousands of lines. To reduce the probability that lines are missed, the representative week obtained before deleting flights starts roughly on May 13 and lasts until roughly June 2. This makes a total of approximately three million flights between these two dates. Statistics about altering of the database are presented in Table 2.3.

Table 2.3: Statistics on altering of the database.

Parameter	**Value**
Number of flights deleted because not correct date	$2,004,667$
Number of flights deleted because not enough data	908
Number of flights deleted because departure airport is destination airport	$38,466$
No complementation: all data complete	$781,597$
Complementation required: all data missing	443
Complementation required: departure and arrival airport missing	$22,082$
Complementation required: aircraft type missing	$3,511$
Complementation required: departure airport missing	$21,305$
Complementation required: arrival airport missing	$50,441$
Complementation required: no other flight found	$99,648$
Number of lines deleted because departure airport is destination airport	$40,119$

Please note that this is the analysis performed purely for complementing of the database. At a later stage a similar table is provided which will present other flights that need to be left out because the performance of the aircraft type is unknown, the airports are not recognized or similar reasons.

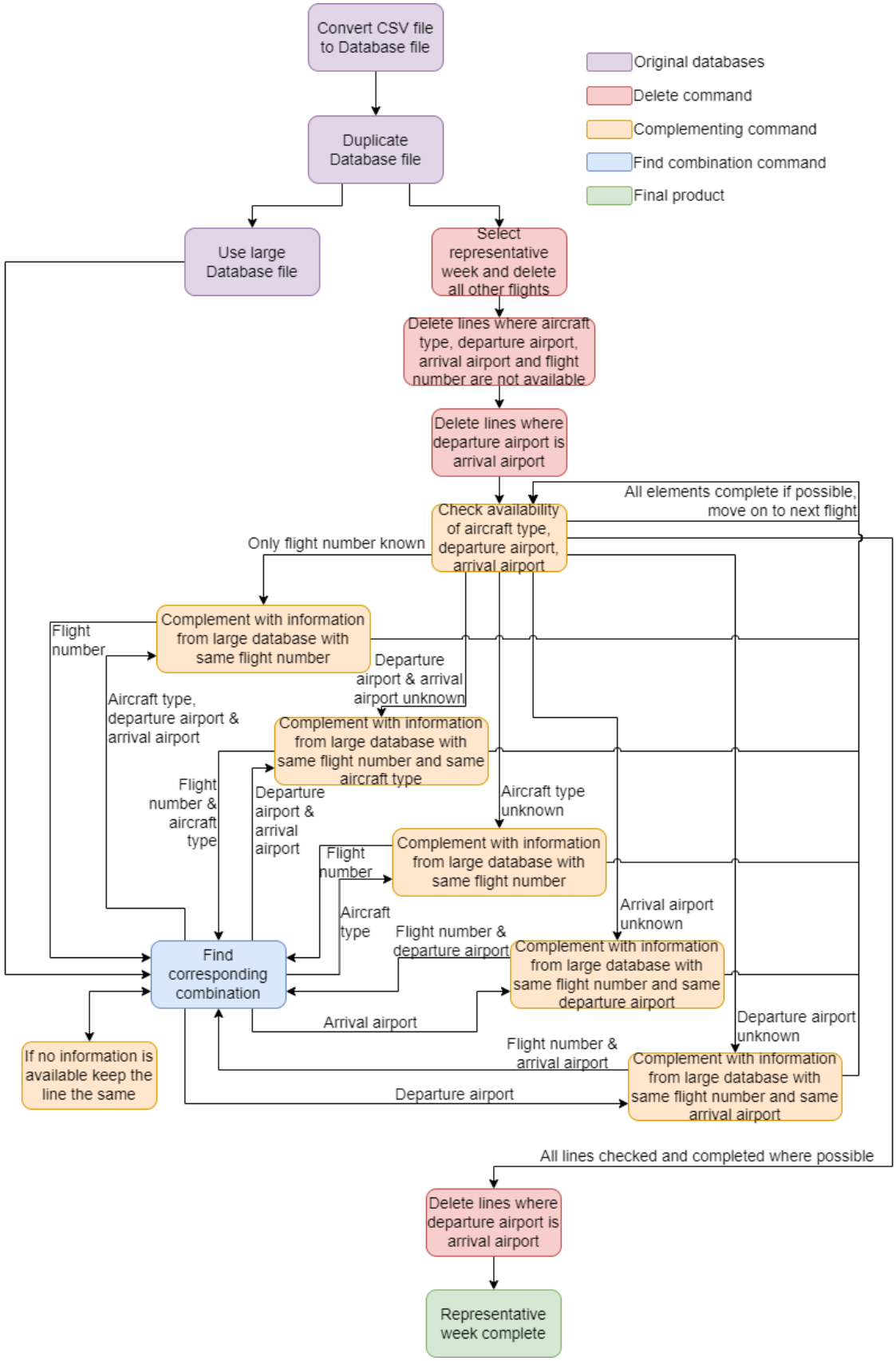

Figure 2.4: Flow chart of complementation of the database.

3

Performance model

The performance model uses inputs from the information model to calculate aircraft performance and fuel burn at each way point throughout the flight trajectory. More information, compared to all inputs from the information model, for this model is required such as the performance during the landing and take-off (LTO) cycles and a database with the locations of airports. Before any additional information is given it is important to mention that the point performance of an aircraft is dependent on three elements: aircraft weight, altitude and airspeed [21].

3.1. Additional inputs

Four more inputs are required in addition to the data from the information model: point performance of variety of aircraft, performance during LTO cycles, geographical information of airports and estimation of aircraft operational parameters. Based on these parameters the trip fuel of a certain trajectory can be estimated and the output from the performance model can be utilized in the emission model.

3.1.1. Point performance

To estimate the fuel consumption of a total flight the complete trajectory is divided in several sections: ground departure, take-off and climbout, climb, cruise, descent, approach and ground arrival. At every section the point performance of the aircraft is estimated based on aircraft mass, airspeed and altitude, by using an aircraft performance database. Various aircraft performance databases are available but the most often used database is the Base of Aircraft Data (BADA) [7]. This database is created by Eurocontrol for the purpose of trip fuel estimation and uses *.txt* files for aircraft (performance) data. Another well-known tool to estimate aircraft fuel consumption for an entire trajectory is PianoX[1], this tool is also able to provide the fuel flow at various points. It is a tool which is often used for validation purposes and for performance estimation. Unfortunately, it is not widely documented what the computational methods are behind the program but its functioning is barely questioned. The last tool that has been found is openAP [22], which is largely based on empirical/statistical relationships and has been developed by J. Sun [22] (a researcher at TU Delft). Substantial efforts have been placed in verifying and validating the openAP model specifically for the Airbus A320 [22]. This program has not been used by a lot of researchers but it functions very well within the *Python* environment. The data within this database is also limited to the fuel flow and emission data. This means that typical air speeds at certain altitudes are not mentioned whereas these are mentioned in the BADA database. This makes trajectory estimation, based on BADA, easier.

Unfortunately PianoX does not allow users to incorporate the database into other external programs, such as *matlab*, *Python* or similar programs. Nevertheless a comparison has been made between the three databases with two random datapoints per aircraft (for ten different aircraft) varying altitude, airspeed and mass. This comparison is presented in Figure 3.1 and Figure 3.2

[1] `https://www.lissys.uk/PianoX.html` (accessed 15-11-2022)

where BADA is taken as a baseline performance program. Note that the blue line presents a $y = x$ relationship.

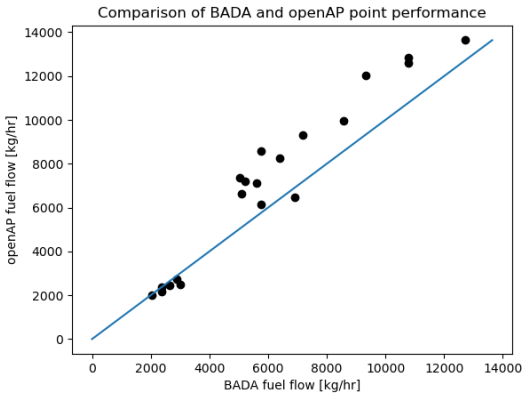

Figure 3.1: Point performance comparison between BADA and openAP.

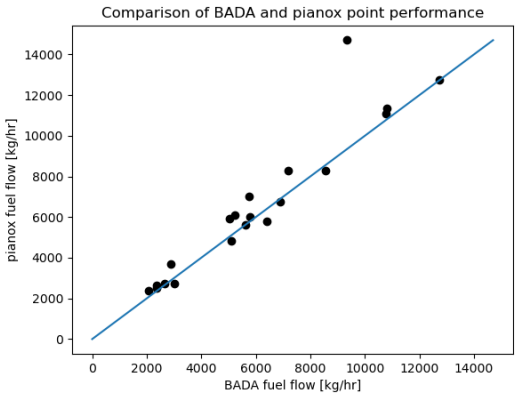

Figure 3.2: Point performance comparison between BADA and PianoX.

From the above figures one is able to conclude that the fuel flow under similar conditions is, on average, underestimated by BADA compared to openAP or PianoX. This is also illustrated in Table 3.1 where the average increase in fuel flow is presented for the various performance models.

Table 3.1: Average increase in fuel flow with baseline BADA.

Parameter	Fuel flow increase compared to *BADA* [%]
openAP increase	14.8
PianoX increase	8.8

The numbers presented in the above table are considered a substantial deviation ($> 5\%$). Referring to the diagrams one can see that there is one outlier in Figure 3.2. Even if this outlier is discarded, the increase in fuel flow of PianoX with respect to BADA is still 6.3%.

The decision is made to use BADA as the performance model database. The line of reasoning is that it is often updated, many similar researches use the database and BADA offers more than just the performance database (more elaboration on this in a later section).

3.1.2. Flight distance increase compared to great circle distance

The information model simply provides the departure and arrival airport, hence no other trajectory information is known. Furthermore, it is general knowledge that aircraft often do not fly this great circle distance [14] (i.e. the shortest distance between two points). It is therefore interesting to see how much farther planes fly compared to their great circle distance.

Access has been provided to various flight plannings of a well-known airline to obtain the trip fuel, flown air distance and the payload mass. This air distance has been compared to the great circle distance of the airport combinations from the flight planning database for a variety of flights. Accordingly, the so-called en-route multiplier was derived: the fractional increase in travelled distance between two points due to not flying over the great circle distance. This analysis has been performed for many of the carrier's aircraft: Embraer E190, Boeing 737-800, Airbus A330-300, Boeing 777-300ER, Boeing 787-9 and Boeing 787-10. Furthermore, four flights per aircraft type are provided. The en-route multiplier for all considered fights is presented in Figure 3.3. This figure clearly presents the distribution of en-route multipliers, clearly all flight distances are close to the great circle distance.

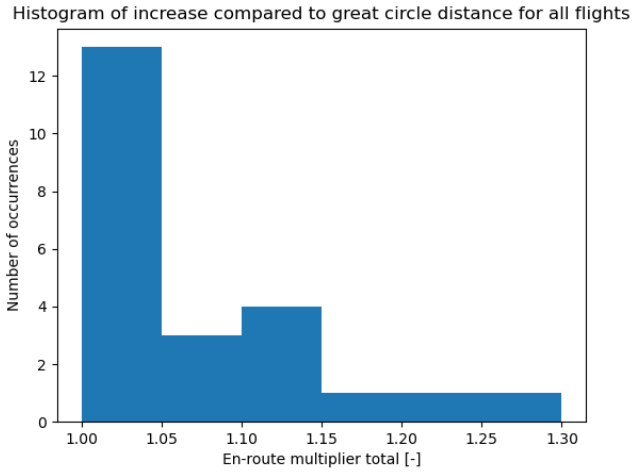

Figure 3.3: En-route multiplier for all considered routes and aircraft.

To quantify the real effect of the en-route multiplier it makes more sense to distinguish between short haul (in this research considered below $1000\ nm$) and long haul aircraft. The underlying reason is that the LTO cycles make up a larger fraction of the trajectory for short haul flights compared to long haul flights. Logically these cycles add distance to the trajectory which fractionally increases short haul flights more than long haul flights. The histograms which distinguish between short haul and long haul are presented in Figure 3.4 and Figure 3.5.

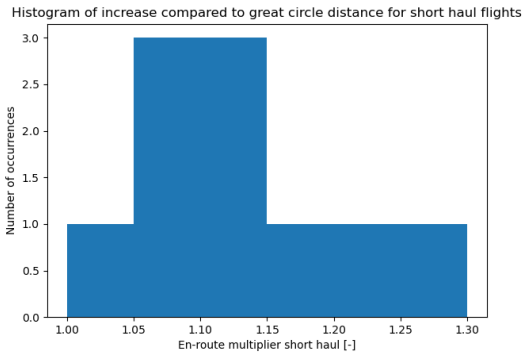

Figure 3.4: En-route multiplier for short haul flights.

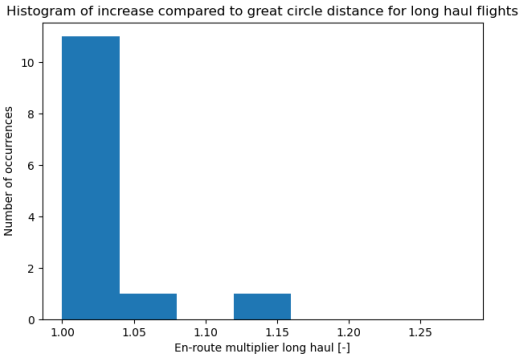

Figure 3.5: En-route multiplier for long haul flights.

In the above figures clear distributions can be seen such as a distribution close to a normal distribution for short haul flights. Furthermore, the explanation concerning the LTO cycle playing a dominant role for short haul flights is proven numerically as the en-route multipliers for long haul aircraft are lower than for short haul aircraft. Note that the distinguishment has been specifically made for the length of a trajectory rather than for an aircraft type as long haul aircraft are occasionally used on short haul stretches. This also occurred in the dataset as the Airbus A330-300 was used on a short haul stretch twice: Dammam - Muscat and Kigali - Entebbe. The averages of the data are also presented in Table 3.2.

The low standard deviation of the long haul flights is clearly in line with the data presented in Figure 3.5. The higher standard deviation for short haul flights is a logical result since the importance of the LTO trajectory increases as the trajectory length decreases. This also means that very small distance short haul flights have a very large effect on the standard deviation of the en-route

Table 3.2: Average increase in trajectory length compared to great circle distance.

Type of flight	Mean en-route multiplier [-]	Associated σ [-]
Short haul	1.130	0.070
Long haul	1.039	0.031
Overall	1.08	0.068

multiplier.

3.1.3. Airport database

Another step to be made in the performance model is the conversion from airport IATA/ICAO code to the geographical location on Earth in terms of latitude, longitude and elevation. A database has been found which has previously been used for another aviation emission inventory by Simone et al. [23]. The mentioned emissions inventory has been performed in 2013 so it is assumed that no significant changes have been made concerning locations of airports or no major airports have been added. This will be verified in a later section. By testing, it has been found that the database is extensive (as about 95% of the flights in the database can be analyzed based on the airport pairs), but for reference's sake all airports are presented in Figure 3.6.

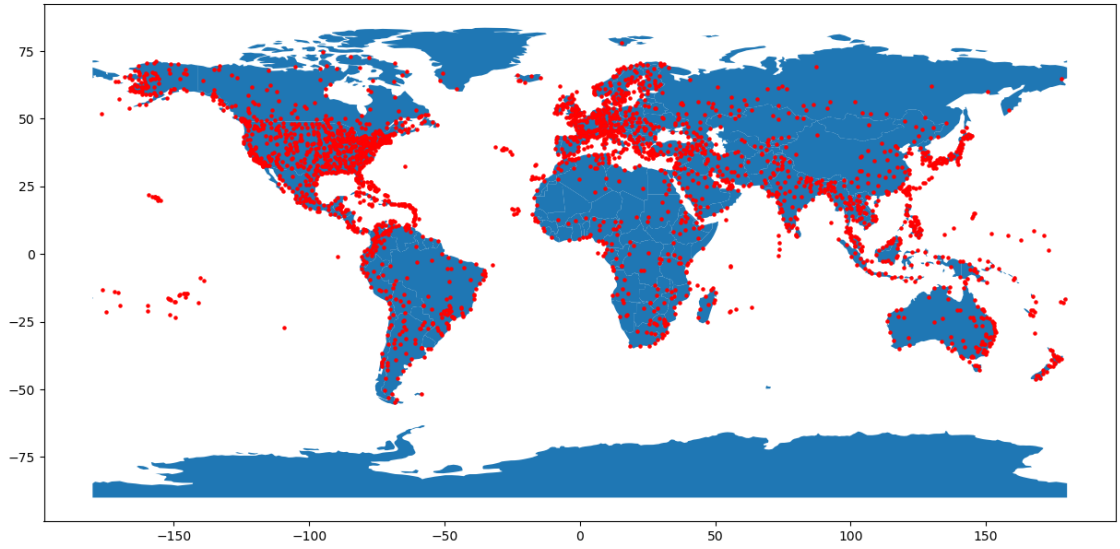

Figure 3.6: All considered airports in the corresponding database.

Smaller airports in the Pacific, the Atlantic, Alaska and northern Canada are also considered. The total number of considered airports is $2,656$. When the emission inventory, from which this database is obtained, was written, the airports in this database formed 99% of all flights in the Official Airline Guide (OAG). It is expected that no significant shift to other airports has occurred in recent years.

3.1.4. Payload mass and empty mass

One significant advantage of BADA is the fact that the data is not limited to point performance data, but masses, types of engines and other data are also provided. For the purpose of this thesis, the mass of an aircraft m_{tot} is divided in three categories: empty weight OEM, payload mass $m_{payload}$ and fuel weight m_{fuel}, i.e.:

$$m_{tot} = OEM + m_{payload} + m_{fuel} \tag{3.1}$$

The fuel mass varies based on the variation of the total weight throughout the flight. An accurate estimation hence needs to be made of the empty mass of an aircraft and the payload mass

of an aircraft. Please note that the empty mass of an aircraft is a standard value which can easily be found online. Unfortunately, this value is not specified in the BADA database and hence, for automation purposes, needs to be deduced from a value which is provided in the database. Various values have been compared but the best fit is found for a fraction of the maximum take-off mass, i.e.:

$$OEM = f_{empty} \cdot MTOM \tag{3.2}$$

where f_{empty} is found to be $f_{empty} = 0.500$ based on an analysis of nine aircraft types (ranging from small single aisles to very large twin aisles) with a standard deviation $\sigma = 0.025$.

Estimation of the payload mass of a specific flight is more difficult as this can fluctuate depending on the occupancy and the popularity of certain routes. The maximum payload mass of an aircraft type is a given in BADA and will be used in a similar manner as the operating empty mass was computed. The validation data from a well-known carrier is used to create a histogram of obtained payload multipliers. This histogram is presented in Figure 3.7.

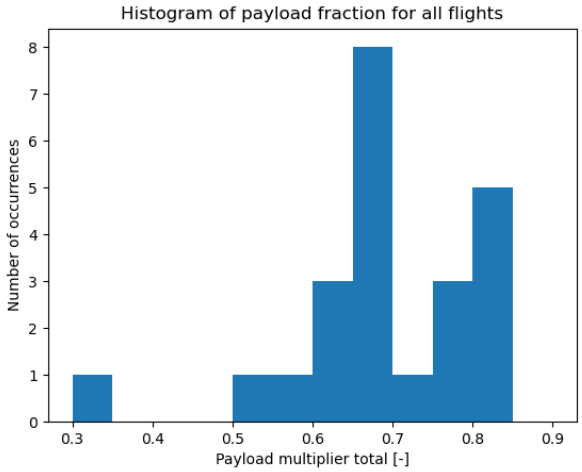

Figure 3.7: Payload multiplier for all considered routes and aircraft.

On average the payload factor, the fractional payload compared to the maximum allowable payload, is $f_{payload} = 0.69$. A distinguishment is made, again, between the short haul and the long haul flights to see what the results are. This is presented in Figure 3.8 and Figure 3.9.

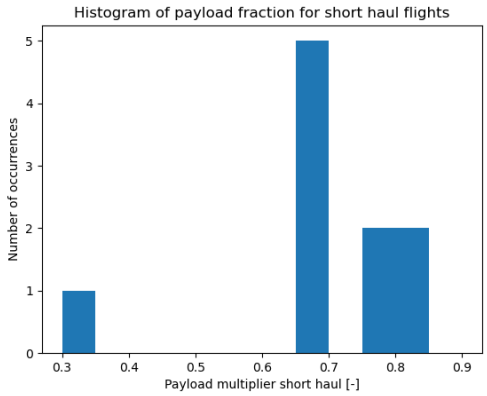

Figure 3.8: Payload multiplier for short haul flights.

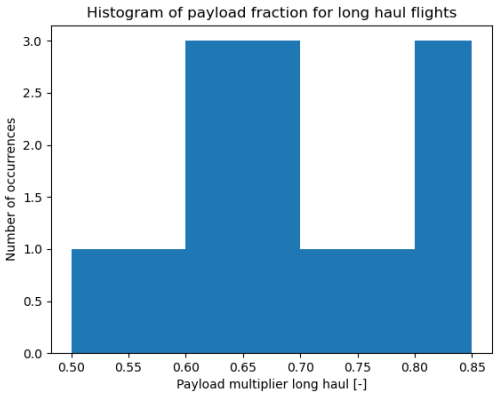

Figure 3.9: Payload multiplier for long haul flights.

The averages are not significantly different in these figures, as also presented in Table 3.3. An important remark should be made as the two previously mentioned flights (the Airbus A330-300 flights) are very short. These two flights have a payload fraction of $f_{payload} = 0.307$ and

$f_{payload} = 0.655$ respectively which is considered low. Since twin aisle aircraft are barely used on these kinds of routes, these two flights are over-represented for their effects in this small database. The result is presented at the bottom of the table, and it is observed that the payload multiplier increases significantly while the associated standard deviation is reduced significantly. The total result is presented in Table 3.3.

Table 3.3: Average payload weight as a fraction of the maximum allowable payload.

Type of flight	Mean payload multiplier [-]	Associated σ [-]
Short haul	0.689	0.148
Long haul	0.690	0.104
Overall	0.690	0.122
Short haul excluding A330-300 flights	0.741	0.065

There is still uncertainty associated to the empty weight of an aircraft for several reasons. Some aircraft models have freighter and passenger versions. The passenger versions have a significantly higher empty weight due to fittings such as seats, galleys and lavatories. For the payload weight there is also associated uncertainty. Researchers in a previous project (*Aero2k* [7]) have conducted a sensitivity analysis where the payload factor of 60.9% was varied with ± 10%. This showed a sensitivity of less than 3% in terms of fuel burn [24]. The assumptions for nominal conditions are therefore considered valid.

3.1.5. ICAO emissions database

In addition to the BADA performance software, used above an altitude of $3000\ ft$, the LTO cycles need to be taken into account. For the purpose of this, ICAO [25] has produced an overview for a variety of data, such as fuel flow rate and emission indices, specified per engine for four thrust settings at mean sea-level. Furthermore, ICAO also specifies the time an aircraft spends within one of these flight phases. The thrust settings and their associated flight phase and time are presented in Table 3.4.

Table 3.4: Thrust setting and associated flight phase and flight time.

Flight phase	Thrust setting [%]	Time [s]
Idle	7	1560
Approach	30	240
Climbout	85	132
Take-off	100	42

Idle time can be divided between taxi-out and taxi-in time where ICAO specifies a taxi-out time of $1140\ s$ and a taxi-in time of $420\ s$.

The database contains many jet engines with varying specifications. This also means that many models of a single engine family are contained in the database. For the purpose of this thesis, the first found engine with a corresponding name to the aircraft engine model is selected for its emissions and fuel flow parameters. If no match is found, the program will continue searching, reducing the length of the engine name by 1 every iteration. In practical terms, for a Boeing 787-10, this means that BADA specifies the GEnx-1B76 engine. The program finds GEnx-1B76/P2 as the best match. Similarly, for the Airbus A321 neo, with engine model Leap-1A32, the selected engine model from the ICAO databank is the LEAP-1A35A/33/33B2/32/30 as the match is found when the reduction in engine name length becomes LEAP-1A3.

The emission and fuel flows in the ICAO database are all reference information at sea level. Therefore, only for the LTO sections of flight, the assumption is made that the airports are located at sea level. This still means that the climb segment starts $3000\ ft$ above sea level, as will be discussed later. This assumption is valid as LTO fuel consumption is less than 10% of total fuel consumption [7]. Furthermore, the 200 busiest airports, according to *Aero2k*, had an average

elevation of $654\ ft$ [7] (weighted for the number of departures) and were responsible for about 65% of departures in the mentioned database.

3.2. Functioning of the performance model

This section aims to present the basic flow of the performance model and how all elements are integrated.

3.2.1. Content of BADA performance table

The BADA performance database provides a variety of data for every phase of the flight. The following is true and provided for a variety of altitudes:

- For climb, the airspeed is specified and the rate of climb ROC for a variety of aircraft masses is specified. Furthermore, the fuel flow is specified for the nominal aircraft mass.
- For cruise, the airspeed is specified and the fuel flow for three aircraft masses is specified: low, nominal and high.
- For descent, the airspeed is mentioned, the rate of descent (ROD) is specified and the fuel flow is provided, all for nominal aircraft mass.

An example of a performance table is presented in Figure 3.10.

BADA PERFORMANCE FILE 98/03/12

AC/Type: F28___

Last BADA Revision: 3.0
Source OPF File: 3.0 98/03/12
Source APF file: 3.0 98/03/12

Speeds: CAS(LO/HI) Mach
climb - 250/270 0.65
cruise - 250/300 0.70
descent - 250/280 0.70

Mass Levels [kg]
low - 20880
nominal - 24000
high - 33000

Temperature: ISA
Max Alt. [ft]: 35000

FL	CRUISE TAS [kts]	CRUISE fuel [kg/min] lo	CRUISE fuel [kg/min] nom	CRUISE fuel [kg/min] hi	CLIMB TAS [kts]	CLIMB ROCD [fpm] lo	CLIMB ROCD [fpm] nom	CLIMB ROCD [fpm] hi	CLIMB fuel [kg/min] nom	DESCENT TAS [kts]	DESCENT ROCD [fpm] nom	DESCENT fuel [kg/min] nom
0					127	2760	2860	2370	108.1	108	900	19.5
5					128	2710	2820	2330	106.4	108	910	19.5
10					129	2670	2780	2290	104.6	114	890	19.4
15					135	2800	2880	2360	103.3	125	850	19.4
20					136	2760	2830	2320	101.6	157	820	19.4
30	261	19.5	20.8	25.8	159	3270	3260	2650	100.0	230	1070	19.3
40	265	19.5	20.9	25.8	193	3960	3820	3070	99.3	233	1080	19.2
60	272	19.6	21.0	26.0	272	5170	4570	3410	98.3	240	1110	19.1
80	280	19.7	21.1	26.1	280	4810	4250	3140	91.7	280	1380	19.0
100	289	19.8	21.2	26.3	289	4460	3930	2880	85.4	289	1410	18.8
120	356	26.4	27.4	31.2	321	4220	3720	2730	80.9	332	1770	18.7
140	366	26.5	27.5	31.3	330	3860	3390	2460	75.1	342	1810	18.6
160	377	26.5	27.6	31.5	340	3500	3060	2200	69.7	353	1840	18.4
180	388	26.6	27.7	31.6	351	3150	2750	1940	64.6	363	1870	18.3
200	400	26.7	27.8	31.8	362	2820	2450	1690	59.8	375	1900	18.1
220	412	26.8	27.9	31.9	373	2510	2160	1460	55.3	386	1930	18.0
240	423	26.6	27.7	31.9	385	2210	1890	1230	51.2	398	1950	17.9
260	419	24.9	26.1	30.7	389	2500	2120	1320	47.1	411	1980	17.7
280	416	23.4	24.8	29.7	386	2210	1850	1070	43.2	416	2570	17.6
300	412	22.1	23.6	29.0	383	1950	1600	840	39.7	412	2430	17.5
320	408	20.9	22.6	28.5	379	1710	1380	630	36.6	408	1890	17.3
340	405	20.0	21.7	28.2	376	1510	1180	430	34.0	405	1830	17.2
360	401	19.1	21.1	28.2	372	1330	1010	240	31.7	401	1780	17.1
380	401	18.6	20.7	28.5	372	1120	810	70	29.9	401	1640	16.9
400	401	18.1	20.5	27.7	372	1010	690	0	28.5	401	1640	16.8

Figure 3.10: Example of a performance table file (PTF) for the Fokker F-28 aircraft (figure obtained from Eurocontrol [26]).

The model relies on aircraft dynamic modelling equations which, fundamentally, are focused on elements in the Total Energy Method, also known as the TEM. The TEM relates the time derivative of the work done by the aircraft's forces to the time derivative of the aircraft's kinetic and potential energy as presented in Equation 3.3:

$$(Th - D)TAS = mg_0\frac{dh}{dt} + mTAS\frac{d(TAS)}{dt} \tag{3.3}$$

where Th represents the thrust in [N], D represents the drag in [N], g_0 is the gravitational acceleration in [m/s^2] and TAS the true airspeed in [m/s]. Based on the TEM, an equation is formulated to compute the rate of climb/descent, $ROCD$, as presented in Equation 3.4:

$$ROCD = \frac{(Th - D)V_{TAS}}{mg_0}\left[1 + \left(\frac{V_{TAS}}{g_0}\right)\left(\frac{dV_{TAS}}{dh}\right)\right]^{-1} \tag{3.4}$$

where the term in square brackets is often referred to as the energy share factor (ESF) as it relates the power of the aircraft during ascent/descent to its acceleration. For more information related to the BADA model and its underlying physical principles and aerodynamics please refer to a report by A. Nuic et al. [27].

Relating to the performance table files, some of the data is only provided for nominal aircraft mass, this means that no interpolation can be made depending on the aircraft mass for these flight phases. Some aircraft are not directly supported by the BADA software. For most of these instances a list of representative aircraft are formulated to allow users to still perform aircraft performance investigations for these aircraft.

Interestingly enough the airspeed is provided for all flight levels, instead of it being a variable. This makes estimation of the trajectory easier as the air speed becomes an output rather than an input. In real life, airlines determine the air speed on several parameters, most important of which is the cost index [28] where the time related cost is compared to the fuel cost. This means that for certain routes a lower/higher air speed is desirable in terms of cost. When aircraft fly at the air speed which minimizes fuel burn per unit distance (also known as the maximum specific air range (SAR)) the fuel consumption rate is relatively insensitive to small perturbations in air speed [7]. The assumption of using the associated air speed referenced in BADA is therefore considered valid.

3.2.2. Performance model flow

Broadly speaking, the performance model's flow is as follows:

Initial take-off mass (TOM) estimation

1. From the departure and arrival airport, the great circle distance is found which is corrected using the en-route multiplier.
2. From the aircraft type, its performance file (the performance table), its OEM, the engine type and its payload mass are retrieved.
3. From the engine type, the fuel flows for the associated thrust settings are found.
4. Estimation of the cruise altitude is done based on the maximum cruise altitude reduced with a constant altitude as aircraft do not fly their maximum cruise altitude.
5. The corresponding cruise fuel flow to the associated cruise altitude is found.
6. Using the airspeed from BADA the trip time is estimated from which easily the trip fuel is estimated.
7. The reserve fuel is calculated as 5% of the trip fuel.
8. The lowest fuel flow from the performance table (i.e. minimum mass and lowest cruise altitude) is found for diversion and holding: for flights longer than 180 minutes $200\ nm$ diversion and $30\ min$ holding is considered, for flights shorter $100\ nm$ diversion and $45\ min$ holding as stated per regulations.
9. The takeoff mass is the summation of the empty mass, the payload mass, the trip fuel, the reserve fuel, the hold fuel and the diversion fuel. This can never exceed the maximum take-off mass ($MTOM$).

Departure LTO cycle

10. The departure fuel, part idle, takeoff and climbout, is estimated using ICAO data.

Climb phase

11. The climb phase is divided in several segments. The climb phase is initiated when climbout is completed ($3000\ ft$ above departure airport elevation). The rate of climb (ROC), airspeed (TAS) and fuel flow are calculated using the BADA database.
12. The ROC at the beginning of a segment is used to determine the time spent in this segment. Furthermore, the fuel flow at the beginning of a segment is used to estimate the fuel mass required to overcome this segment.
13. A correction is applied to account for acceleration during climb as the BADA data is point performance data. The fuel due to acceleration of a certain segment is calculated based on the airspeed at the beginning and the end of the segment and the aircraft's mass at the beginning of the segment:

$$m_{fuel,acceleration,i} = \frac{0.5 \cdot m_i \cdot \left(TAS_{i+1}^2 - TAS_i^2\right)}{LHV_{fuel} \cdot \eta_{acceleration}} \tag{3.5}$$

where m_i and TAS_i denote the mass in [kg] and airspeed in [m/s] at the beginning of the segment, TAS_{i+1} represents the airspeed at the end of the segment, LHV_{fuel} is the lower heating value of the fuel in [MJ/kg] and $\eta_{acceleration}$ is the efficiency of accelerating the aircraft (taking into account, amongst others, efficiency of propulsion). Note that the equation resembles the change in kinetic energy in terms of fuel mass.

14. At the end of every climb segment the mass of the aircraft, the altitude and the airspeed are updated.
15. Climb ends when the maximum altitude is reached or the ROC does not exceed $500\ fpm$ to avoid extremely long segments of climb. This value has been determined based on visually checking various performance files to find a logical minimum rate of climb.

Cruise distance

16. The cruise distance is calculated based on the corrected great circle distance, the horizontal distance travelled in climb and an estimation of the descent distance [4]:

$$d_{descent} = \frac{3 \cdot (h_{end,cruise} - (h_{arrivalairport} + 3000))}{1000} \tag{3.6}$$

This descent distance is simply a linear function taking into account a standard descent angle.

Cruise phase

17. The cruise phase is divided in several segments depending on the length of the flight. At the beginning of every segment it is first checked whether the plane can climb (if the $ROC > 500\ fpm$). If climb is possible, the steps from the climb phase are used until the rate of climb is deemed insufficient ($ROC < 500\ fpm$).
18. The time of a segment is calculated based on the airspeed and the length of a segment.
19. If climb is not possible the fuel flow is determined at the beginning of the section and based on this fuel flow the fuel mass of the entire section is computed.
20. At the end of every cruise segment, the mass of the aircraft, the altitude and the airspeed are updated.

Descent phase

21. The descent phase finishes at $3000\ ft$ above elevation of the arrival airport (as then the approach phase starts).
22. Descent is divided in several segments. The rate of descent (ROD) at the beginning of every segment is used to calculate the time of every segment.
23. Based on the fuel flow at the beginning of every section the fuel required for that section is calculated.

24. At the end of every descent segment the mass of the aircraft, the altitude and the airspeed are updated.

Arrival LTO cycle

25. The approach fuel, and taxi-in fuel are calculated based on ICAO data.

Graphically, although in simplified format, the procedure described above is presented in Figure 3.11.

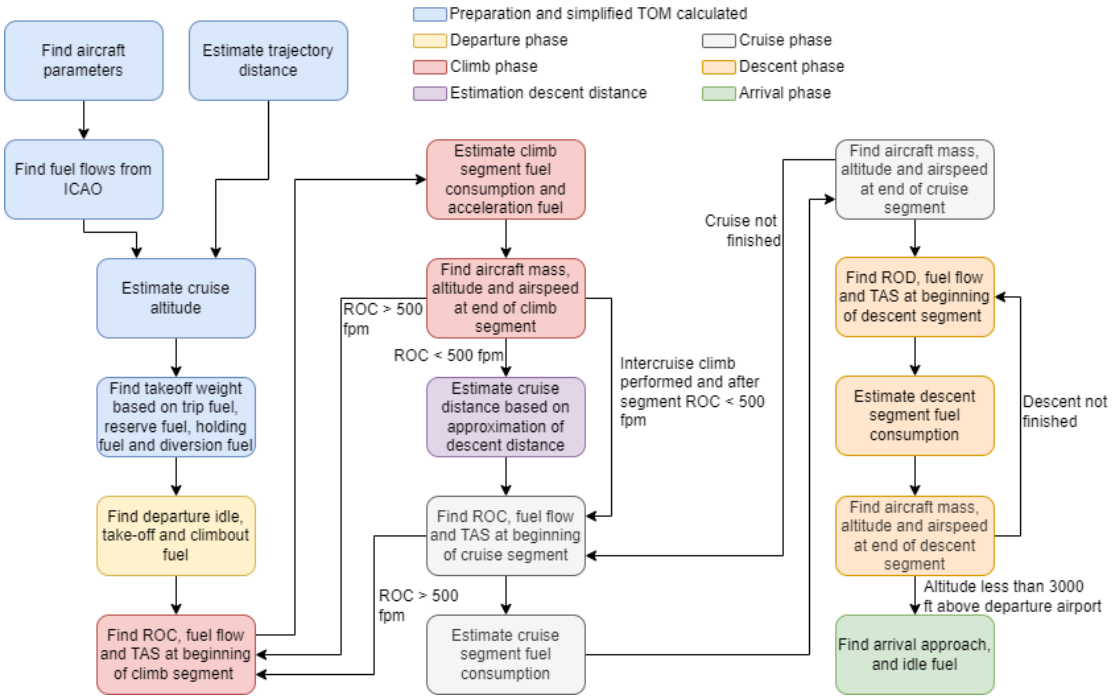

Figure 3.11: Flowchart of the functioning of the performance model.

4

Emission model

After the performance of the aircraft has been estimated, the next step is to compute the emissions for every flight phase. First the importance of these emissions is discussed, after which the methodology to compute the emissions is described.

4.1. Importance

Before estimating the quantity of emissions it is fundamental to understand their importance. In this research seven emission species are considered: carbon dioxide, carbon monoxide, unburned hydrocarbons, nitrogen oxides, sulphur oxides, water vapor and black carbon. This summarizes all of the emission species discussed in the reference literature (work performed by Simone et al. [4], C. J. Eyers et al. [7], S.L. Baughcum et al. [8], W. Fan et al. [9], D.K. Wasiuk et al. [10], J. Li et al. [11] and B. Owen et al. [12]). For the purpose of understanding the impact of various emission species, it is also important to understand how global warming takes place. Global warming occurs because there is a positive difference between the quantity of incoming and outgoing radiation, called radiative forcing (RF) [29]. The process of global warming, and its effects, is presented in Figure 4.1.

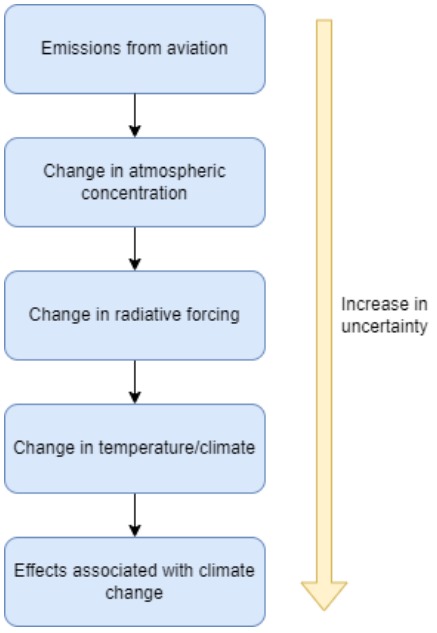

Figure 4.1: Causes and effects of global warming (figure inspired by *Impact of Uncertainties on the Climate-Optimized Aircraft Design* [29]).

Fundamentally, the process of warming happens as follows. Burning fuel emits various emis-

sion species. Due to the change in atmospheric composition, more outgoing longwave radiation is captured, i.e. less radiation is scattered back into space. This creates a net positive radiative forcing. According to the Stefan-Boltzman law, governing the radiation caused by a body of a certain temperature, global warming occurs which consequentially affects the climate [30]. This warming effect also impacts biodiversity and entire ecosystems [31].

4.1.1. Emission effects

Emission species have effects both on the climate and on air quality. To understand the impact of insufficient air quality, according to the World Health Organization approximately 600,000 children under the age of five die every year because of air pollution [32].

It is well-known that carbon dioxide plays an important role in the greenhouse effect [33], which is responsible for the current climate change crisis. Carbon dioxide concentrations have increased from about $300\ ppm$ to $410\ ppm$ [33] due to human influence. Mankind has never been subject to these large concentrations of carbon dioxide during its evolution. Researchers therefore suggest that toxicity effects [34] [35] could come into play with the rising levels of carbon dioxide [36] [37].

The effects of carbon monoxide emissions are also well-known. In terms of climate effects, carbon monoxide is responsible for the phenomenon acid rain [38] which, amongst other effects, decreases nutrients for plants. It therefore has an important influence on the functioning of ecosystems. Locally, depending on the concentration, carbon monoxide causes carbon monoxide poisoning which reduces the quantity of oxygen reaching organs and tissues [39].

Unburned hydrocarbons consist mainly of aldehydes and aromatic hydrocarbon (compounds) [40]. Depending on the concentration, these emission species can restrict photosynthesis in plants. Furthermore, if exposed for a longer period of time, mammals can get cancer from these species [40]. Lastly, if chemical reactions take place in the atmosphere nitrous oxides can be produced which can affect human organs.

Nitrogen oxides are byproducts of combustion taking place at high temperatures [41]. Its effect on the environment are ozone layer depletion (depending on the emission altitude) and the species cause acid rain due to chemical processes taking place in the atmosphere [41]. Furthermore, nitrogen oxides trigger plant growth of some plant species, therefore eradicating other species which might be of great value to the biodiversity [42]. Lastly, in terms of human health, nitrogen oxides can lengthen viral infections and can cause adverse effects on human lungs [42].

Sulfur oxides have both environmental and health effects. Environmentally, sulfur oxides can cause acid rain which has a direct effect on ecosystems by lowering the pH. This can result in mass fish mortality due to large shifts in pH [43]. Health effects associated with sulfur oxides are respiratory diseases and irritation of nose and throat [43]. Repeated exposure to very high levels could lead to premature death.

Water vapor is a known greenhouse gas [44], although of lower importance than carbon dioxide. Furthermore, water vapor tends to form contrails (depending on the particle emission and the Schmidt-Appleman criterion [45]), which both have a negative and positive effect on the greenhouse effect: due to an increase in albedo area, more light is reflected back into space but on the other hand more heat is trapped due to the mentioned greenhouse effect [44]. Health is not significantly impacted by an increase in water vapor emissions.

Black carbon emissions are caused by combustion processes, both natural and anthropogenic. After emission, black carbon emissions can travel large distances and finally are washed away by precipitation [46]. Black carbon has both a warming and a cooling effect: due to the formation of clouds the albedo effect decreases the atmospheric temperature while the absorption of radiation leads to atmospheric warming [46]. Black carbon is so small it is easily inhaled. Black carbon is associated with asthma, low birth rates, heart attacks and lung cancer [47].

4.1.2. Effect of altitude

An element which is significantly different for aviation (compared to ground bound methods of transportation) is the influence of altitude on the climate impact of emission species. This is illustrated in Figure 4.2 which presents the forcing factor, $s_i(h)$, of various atmospheric species formed by chemical processes due to emission of nitrogen oxide and the aviation induced contrails. In this diagram O_{3s} represents the short lived ozone, O_{3l} represents the long lived ozone while AIC is an abbreviation for the aircraft-induced cloudiness [29]. The forcing factor "accounts for the variation in RF per unit emission at a particular altitude, normalized by the fleet-wide average RF" [48]. Note that the AIC is taken into account with the red line.

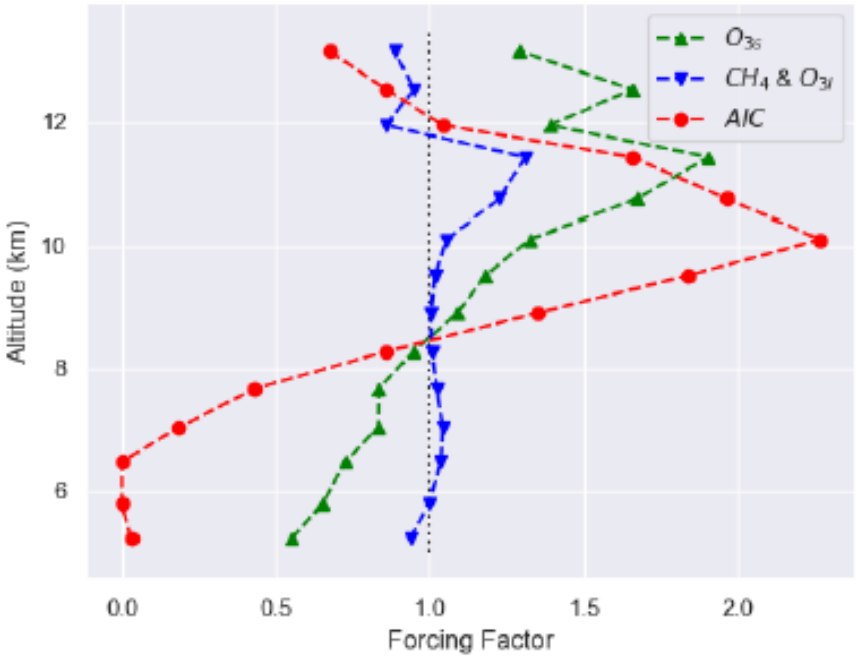

Figure 4.2: Effect of altitude on forcing factor for various species (figure obtained from *Impact of Uncertainties on the Climate-Optimized Aircraft Design* [29]).

In addition, Figure 4.3 presents the increase/decrease in radiative forcing compared to a reference case. REACT4C is a project where the baseline emissions and climate impact are calculated and a shift in flight level (both lower and higher flight level) is used to estimate the change in climate impact due to a change in altitude.

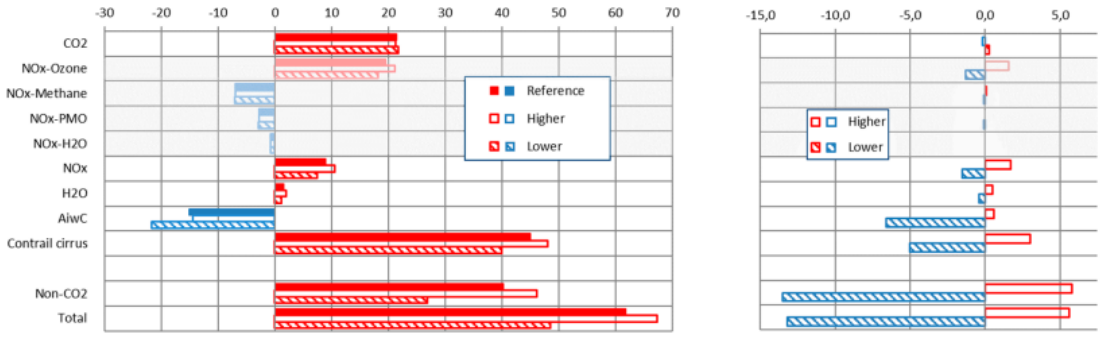

Figure 4.3: Effect of radiative forcing [mW/m^2] due to aviation, on the left the absolute case and on the right a comparison is made with baseline being the regular flight altitude (figure obtained from *Mitigation of Non-CO2 Aviation's Climate Impact by Changing Cruise Altitudes* [3]).

These two figures amplify the fact that a thorough understanding is required on the altitude at

which emission occurs. For climate scientists to make accurate predictions, it is therefore essential that the output of the emission model is a three-dimensional grid of all emission taking place.

4.2. Methodology of emission calculation

To estimate aviation emissions the concept of emission index (EI) is very suitable. An emission index is the quantity of emission per unit of fuel burned. Various methodologies are available for emission index estimation. The most common applied methodology is the Boeing Fuel Flow Method 2 (BFFM2) [49] for nitrogen oxide emission calculation. Another method for nitrogen oxide emission calculations, which is applied more often on an individual flight basis, is the p3-T3 method [50]. A large advantage of the BFFM2 over the p3-T3 method is the fact that the BFFM2 does not utilize proprietary engine information. The information used in the BFFM2 and for p3-T3 methodology is provided by ICAO in their Aircraft Engine Emissions Databank, with the exception that proprietary engine information is required in addition to the ICAO data for the p3-T3 method. The decision is therefore made to use the BFFM2 to compute emission indices. Note that the uncertainty of this model is addressed later. Lastly, it is important to mention that the emission index of some species is independent of the flight phase (such as sulfur oxides or water vapor). After obtaining the emission index, the emissions are simply computed using Equation 4.1, discretized over the entire flight:

$$m_x = \int_{t_{depart}}^{t_{arrival}} \dot{m}_{fuel}(t) EI(x,t) dt = \sum_{t_{depart}}^{t_{arrival}} \dot{m}_{fuel}(t) EI(x,t) \Delta t \tag{4.1}$$

where x denoted a certain emission species and t denotes the time of a certain flight phase.

4.2.1. Constant emission indices

The chemical formula of kerosene is $C_{12}H_{23}$ [51] (note that impurities in the fuel are discussed later). If this fuel is perfectly combusted this gives the following chemical reaction:

$$4C_{12}H_{23} + 71O_2 \longrightarrow 48CO_2 + 46H_2O \tag{4.2}$$

From the chemical equilibrium (and the molar masses) the emission index of carbon dioxide can be found (for perfect combustion):

$$EI(CO_2) = \frac{m_{CO_2}}{m_{C_{12}H_{23}}} = \frac{48 \cdot 44.0}{4 \cdot 167.3} = 3.156 kg/kg \tag{4.3}$$

Due to the fact that kerosene contains some very minor impurities, the emission index is regularly taken as $EI(CO_2) = 3.155\ kg/kg$ [9]. For water vapor a similar approach is conducted:

$$EI(H_2O) = \frac{m_{H_2O}}{m_{C_{12}H_{23}}} = \frac{46 \cdot 18.0}{4 \cdot 167.3} = 1.237 kg/kg \tag{4.4}$$

This is identical to the normally used emission index of water vapor, $EI(H_2O) = 1.237\ kg/kg$ [8].

For sulfur oxides the emission index is dependent on the quality of the fuel in terms of sulfur content. Regularly the emission index is taken as $EI(SO_x) = 0.8\ g/kg$ [11] [9] [8].

4.2.2. Non-constant emission indices

Other emission indices change as a function of the thrust setting and the ambient conditions. The selected method for this is the Boeing Fuel Flow Method 2 for all regular emissions but for black carbon the DLR fuel flow method [52] is selected as the BFFM2 does not provide means to compute these emission indices. Underneath, both methodologies are outlined.

Boeing Fuel Flow Method 2

This method is applied to find the unburned hydrocarbon emission, the carbon monoxide emission and the nitrogen oxides emission. Please note that all equations describing the BFFM2 in this subsubsection are obtained from research by W. Fan et al. [9], F. Jelinek et al. [13] and M. Schaefer et al. [53]. The basic functioning of the BFFM2 is presented in Figure 4.4.

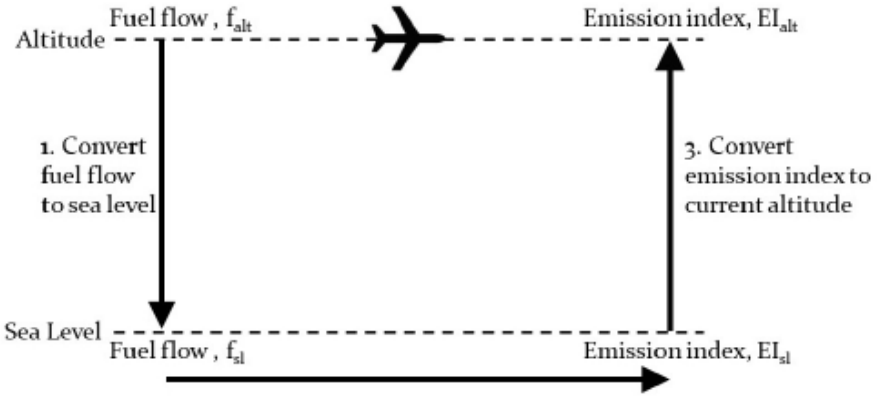

Figure 4.4: Functioning of the Boeing Fuel Flow Method 2 (figure obtained from *Analysis of Aircraft Emissions Based on Flight Trajectory* [54]).

First a correction is applied to the fuel flows from the ICAO database to incorporate the effect of airframe integration as can be seen in Table 4.1.

Table 4.1: Thrust settings and associated airframe integration correction coefficients [53].

Flight phase	Thrust setting [%]	Correction coefficient [-]
Idle	7	1.1
Approach	30	1.02
Climbout	85	1.013
Take-off	100	1.01

The fuel flow at the considered altitude needs to be converted to sea-level conditions first. This is presented in Equation 4.5, 4.6 and 4.7:

$$W_f = \frac{W_{ff}}{\theta_{amb}^{3.8} \exp{(0.2M^2)}} \delta_{amb} \tag{4.5}$$

$$\theta_{amb} = \frac{(T_{amb} + 273.15)}{288.15} \tag{4.6}$$

$$\delta_{amb} = \frac{P_{amb}}{101325} \tag{4.7}$$

In the above equations W_f is the fuel flow (in kg/s) at the considered altitude, W_{ff} is the fuel flow (in kg/s) at sea level, T_{amb} is the ambient temperature (in °C) at the considered altitude, P_{amb} is the ambient pressure (in Pa) at the altitude and finally M represents the flown Mach number.

Based on the fuel flow per engine predicted by the *BADA* software the reference emission index can be obtained by means of interpolation. Regular interpolation is used for nitrogen oxides while bilinear interpolation is used for unburned hydrocarbons and carbon monoxide (presented in Figure 4.5).

The interpolation yields a reference emission index at sea-level which needs to be converted back to the considered altitude. The required equations for unburned hydrocarbons and carbon monoxide are presented in Equation 4.8 and Equation 4.9:

$$EI(HC) = REI(HC) \frac{\theta_{amb}^{3.3}}{\delta_{amb}^{1.02}} \tag{4.8}$$

$$EI(CO) = REI(CO) \frac{\theta_{amb}^{3.3}}{\delta_{amb}^{1.02}} \tag{4.9}$$

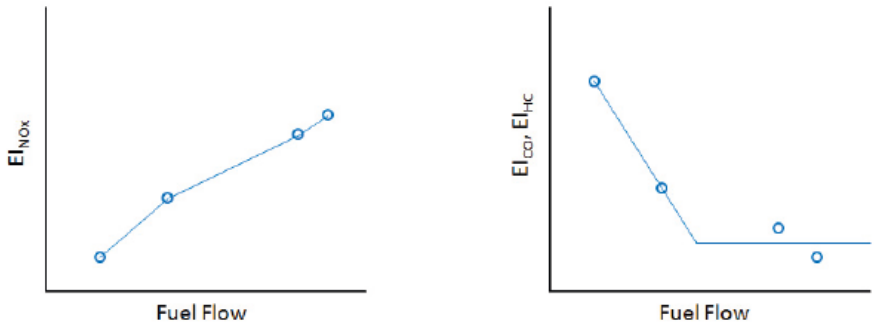

Figure 4.5: Regular interpolation of emission index (left) and bilinear fit (right) (figure obtained from *Overview on fuel flow correlation methods for the calculation of NO_x, CO and HC emissions and their implementation into aircraft performance software* [53]).

Carbon monoxide emission only occurs in case of incomplete combustion which has a direct effect on the emission of carbon dioxide (as the carbon atoms all come from the fuel). Therefore a correction is made on the emission index of carbon dioxide based on the difference of molar masses between these two species [7]:

$$EI(CO_2) = EI(CO_{2,ideal}) - \frac{44}{28} \cdot EI(CO) \tag{4.10}$$

with $EI(CO_{2,ideal}) = 3.155\ kg/kg$ as mentioned previously.

For nitrogen oxides the process is more difficult as presented in Equation 4.11:

$$EI(NO_x) = REI(NO_x) \exp(H) \left(\frac{\theta_{amb}^{3.3}}{\delta_{amb}^{3.02}}\right)^{-0.5} \tag{4.11}$$

where the value of H is computed using:

$$H = -19 \times (\omega - 0.0063) \tag{4.12}$$

where parameter ω, the specific humidity, is computed as follows:

$$\omega = \frac{0.62198(\phi)P_v}{P_{amb} - (\phi)P_v} \tag{4.13}$$

Note that ϕ represents the relative humidity at cruise altitude (taken as a constant in the *ICAO* databank: $\phi = 0.6$ [50]). The value of P_v, the saturated vapor pressure, is calculated using Equation 4.14:

$$P_v = (0.014504) \times 10^{\beta} \tag{4.14}$$

where β is calculated using Equation 4.15:

$$\begin{aligned}\beta = 7.90298 \left(1 - \frac{273.16}{T_{amb} + 273.16}\right) + 3.00571 + (5.02808) \log \left(\frac{273.16}{T_{amb} + 273.16}\right) \\ + \left(1.3816 \times 10^{-7}\right) \left[1 - 10^{11.344\left(1 - \frac{T_{amb}+273.16}{273.16}\right)}\right] \\ + \left(8.1328 \times 10^{-3}\right) \left[10^{3.49149\left(1 - \frac{373.16}{T_{amb}+273.16}\right)-1}\right]\end{aligned} \tag{4.15}$$

Some special cases and exceptions can occur, such as a fuel flow below idle. For these special cases please consult research by M. Schaefer et al. [53]. In addition, it is mentioned that the BFFM2 is not applicable for computation of lean burn technology engines as it often overestimates the emission index of NO_x [55]. The method is more suitable for previous generation engines such as RQL combustors [55].

Unfortunately, no other suitable methods are found which utilize non-proprietary engine information. Therefore a comparison is made between the GEnx engine's predicted NO_x emission by p3-T3 methods (Figure 4.6) and the predicted BFFM2 emission index under the same circumstances (Figure 4.7). This engine is typically used on the Boeing 787 series, which is the largest aircraft series at this moment with this kind of lean burn technology engines [56].

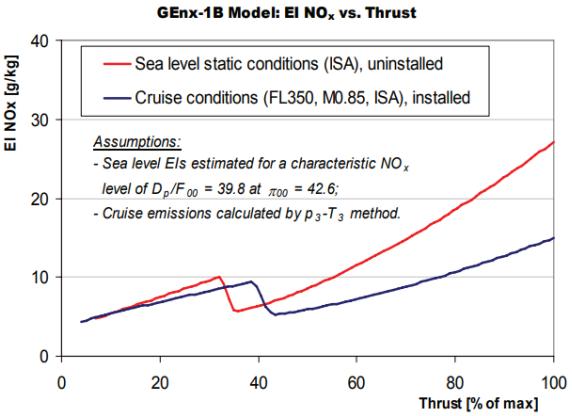

Figure 4.6: Emission index of NO_x estimated by p3-T3 methodology for GEnx-1B engine (figure obtained from *Development of a Forecast Model for Global Air Traffic Emissions* [57]).

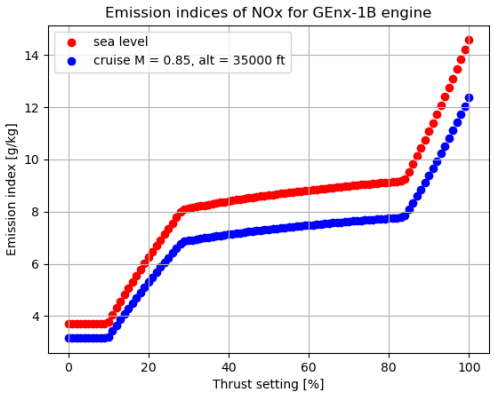

Figure 4.7: Emission index of NO_x estimated by BFFM2 methodology for GEnx-1B engine.

The red line in Figure 4.7 is simply the interpolated values from the *ICAO* databank. These are measured values and are therefore validation data. For thrust settings above 60% the estimated emission index of nitrogen oxides obtained using the p3-T3 method is almost double that compared to the BFFM2 for sea level conditions, for cruise conditions the match is significantly better but a minor overestimation for p3-T3 is still visible. This means that the p3-T3 method, in this instance, overestimates the emission of nitrogen oxides. This is contrary to the expected result as an overestimation of emission index of a traditional method was expected for these new technology combustors. Performing accuracy assessment of aviation emission estimation could be a large project on its own and therefore, even though this can be considered anecdotal evidence, it is decided that the BFFM2 can also be used for the lean burn combustor technology engines.

One can easily observe that the two figures do not look similar. This is simply caused by the prescribed method to be carried out in the BFFM2 where linear interpolation occurs for the emission index of NO_x. Furthermore, only four data points are provided in the ICAO database whereas more points would have been beneficial for the accuracy of estimation. Especially the gap between the 30% and 85% thrust setting is considered very large. The drop in emission index at $\pm 30\%$ thrust in Figure 4.6 is modelled more accurately when the interpolation method is changed from linear to quadratic as presented in Figure 4.8. This drop, however, is shifted to the right too much which is caused by the emission index point at 30% thrust setting. As the BFFM2 clearly defines linear interpolation, this method is uphold, but it is recommended to conduct studies into BFFM2 alterations such as changing interpolation methods.

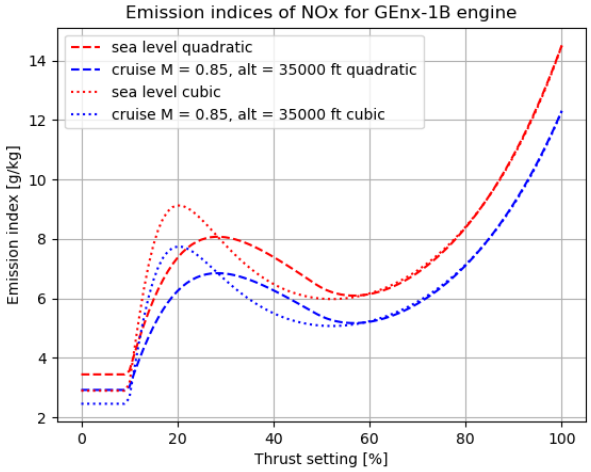

Figure 4.8: Emission index of NO_x estimated by BFFM2 methodology for GEnx-1B engine with quadratic and cubic interpolation.

FOA and DLR method

Petzold et al. [58] discuss that the black carbon emission is largely dependent on the combustor exit temperature. In 1999, for the global aviation fleet, the average emission index of black carbon, $EI(BC)$ was found to be $EI(BC) = 0.038\ g/kg$ [58]. Estimating black carbon emissions can be done based on a method similar to the p3-T3 method as performed by Agarwal et al. [59]. Similar to the regular p3-T3 method, proprietary engine information is required for this and is therefore not useful for automation in an emission inventory. A method by Peck et al. [60] has been developed which uses the fuel flows and the smoke numbers from the ICAO databank to estimate the black carbon emission index. This method is largely based on the DLR method [52] and the FOA2.0/FOA3.0 (First Order Approximation) method [61] [62]. The simplified process of estimation the black carbon emission index is presented in Figure 4.9.

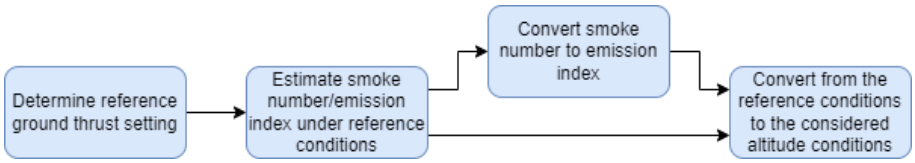

Figure 4.9: Estimation of the emission index of black carbon (figure adapted from *An algorithm to estimate aircraft cruise black carbon emissions for use in developing a cruise emissions inventory* [60]).

Please note that the following equations are all obtained from research by J. Peck et al. [60]. The first step is to find the pressure and temperature at the considered cruise altitude (according to the ISA) and find the total temperature (see Equation 4.16) and pressure (see Equation 4.17):

$$T_{t,cruise} = T_{cruise}\left(1 + \frac{\gamma - 1}{2}M^2\right) \tag{4.16}$$

$$p_{t,cruise} = p_{cruise}\left(1 + \frac{\gamma - 1}{2}M^2\right)^{\gamma/(\gamma-1)} \tag{4.17}$$

The article's next step is to assume a cruise thrust setting $[F/F_{00}]_{cruise}$ of typically 65%, assumed constant during the entire cruise flight. This is considered too arbitrary for the purpose of the emission inventory and therefore an alternative method is developed. Equation 4.5 is used to convert the fuel flow from the cruise altitude to reference sea-level conditions. This reference fuel flow is then used to interpolate the thrust setting based on the four ICAO thrust settings and fuel flows. This method hence provides the value of $[F/F_{00}]_{cruise}$. This allows one to find the value of

p_3, the compressor pressure, as the value of π_{00} is obtained from the ICAO emissions databank:

$$\frac{p_3}{p_{t,cruise}} = 1 + \left[\frac{F}{F_{00}}\right]_{cruise} (\pi_{00} - 1) \tag{4.18}$$

After that, the combustor inlet temperature, T_3, is estimated:

$$\frac{T_3}{T_{t,cruise}} = 1 + \frac{1}{\eta_{comp}} \left\{ \left(\frac{p_3}{p_{t,cruise}} \right)^{\frac{\gamma-1}{\gamma}} - 1 \right\} \tag{4.19}$$

An average compressor efficiency of $\eta_{comp} = 0.85$ is used. The reference compressor pressure is then computed as follows:

$$\frac{p_{3,ref}}{p_{ground}} = \left\{ 1 + \eta_{comp} \left(\frac{T_{3,ref}}{T_{ground}} - 1 \right) \right\}^{\frac{\gamma}{\gamma-1}} \tag{4.20}$$

The ground reference thrust setting is estimated by using Equation 4.21:

$$\left[\frac{F}{F_{00}}\right]_{ref} = \frac{\frac{p_{3,ref}}{p_{ground}} - 1}{\pi_{00} - 1} \tag{4.21}$$

The next step is another deviation from the article. More recent versions of the ICAO databank contain an emission index databank of black carbon emissions. Therefore it is first checked to see whether the engine model is available in this sheet. If the engine model is available the emission indices are taken from the sheet. If these are not available, the line of the article is followed to obtain the smoke numbers at the four thrust settings of the engine model. Interpolation is performed to find the smoke number SN_{ref} at the reference thrust setting. This is then converted to the mass emission index by using Equation 4.22:

$$EI(BC_{ref}) = 14.8 \times SN_{ref} \tag{4.22}$$

The next step is to convert the emission index to the black carbon concentration $C_{BC,ref}$ by dividing the volumetric flow rate per unit mass of fuel burn following Equation 4.23:

$$C_{BC,ref} = \frac{EI(BC_{ref})}{\dot{Q}_{ref}} \tag{4.23}$$

where the volumetric flow rate per unit mass of fuel burned at a certain thrust setting ($\dot{Q}$) is calculated using Equation 4.24:

$$\dot{Q} = 86.37 \exp\left(-0.9136 \left[\frac{F}{F_{00}}\right] \right) (1 + \beta) + 0.877 \tag{4.24}$$

Note that in Equation 4.24 $\beta = 0$ for unmixed turbofan engines and β is the bypass ratio for mixed turbofan engines.

The reference black carbon concentration $C_{BC,ref}$ can then be converted to the cruise black carbon concentration using the DLR correlation [58]:

$$C_{BC} = C_{BC,ref} \left(\frac{\phi}{\phi_{ref}} \right)^{2.5} \left(\frac{p_3}{p_{3,ref}} \right)^{1.35} \left(\frac{\exp(-\frac{20{,}000}{T_{fl}})}{\exp(-\frac{20{,}000}{T_{fl,ref}})} \right) \tag{4.25}$$

where T_{fl} is the flame temperature, and estimated using Equation 4.26 [63]:

$$T_{fl} = 2281 \left(p_3^{0.009375} + 0.000178 p_3^{0.055} (T_3 - 298) \right) \tag{4.26}$$

It is mentioned that the equivalence ratio, under both cruise and reference conditions, can be assumed as 1, i.e. $\phi = \phi_{ref} = 1$ as the primary combustion zone is operated at near-stochiometric

conditions. The last step is to convert the black carbon concentration at the cruise altitude to the mass emission index at that cruise altitude:

$$EI(BC) = C_{BC}\dot{Q} \tag{4.27}$$

The mass of black carbon at every altitude and flight condition is known but the number of black carbon particles is not. The number of particles per gram of black carbon emission is very much dependent on the flight altitude [7]. This is presented in Figure 4.10.

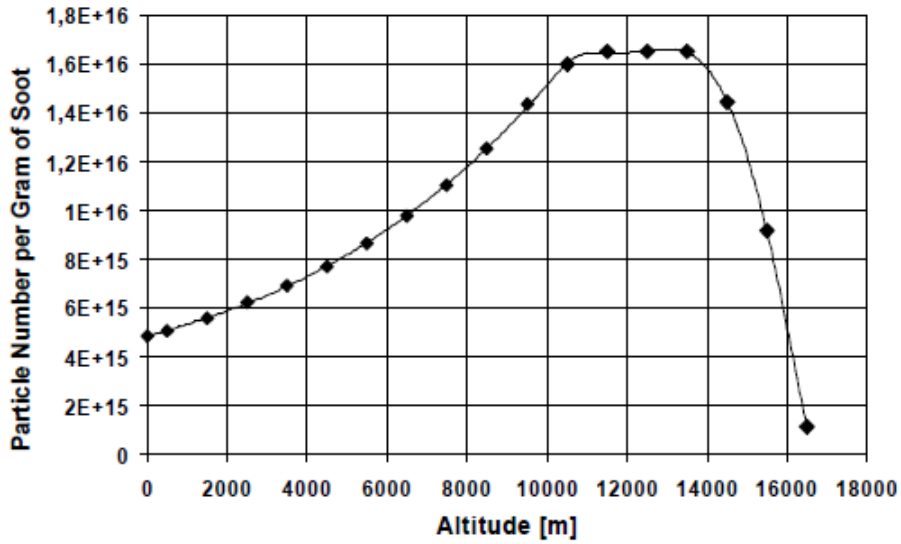

Figure 4.10: Number of soot particles per gram of black carbon emission (figure obtained from *AERO2k Global Aviation Emissions Inventories for 2002 and 2025* [7]).

Based on the figure, the following equation is deduced describing the number of black carbon particles per gram of black carbon emission as a function of altitude:

$$n_{particles} = -0.00000026h^5 + 0.02735h^4 - 679h^3 + 0.093 \cdot 10^8 h^2 + 0.91 \cdot 10^{11} h + 5 \cdot 10^{15} \tag{4.28}$$

where $n_{particles}$ represents the number of particles in a gram of black carbon emission and h represents the altitude in ft.

4.3. Flow chart

The flow chart of the performance model in Figure 3.11 is altered based on the additions in the emission model. For simplification purposes the preparation and simplified take-off-mass calculations are taken out of the flow diagram. The updated flow chart is presented in Figure 4.11.

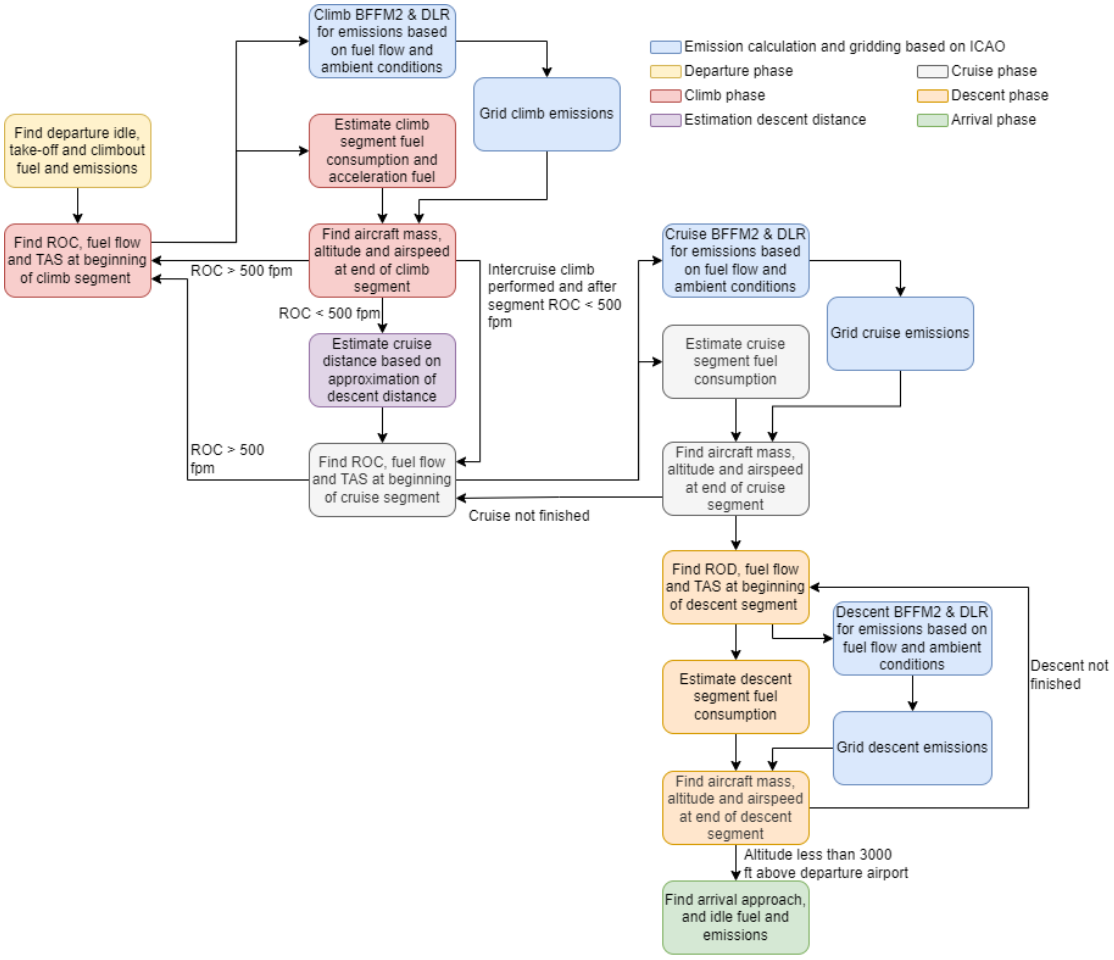

Figure 4.11: Flowchart of the functioning of the performance and the emission model.

5

Uncertainty Analysis

The goal of the uncertainty analysis is to use uncertainties associated to individual parameters to find the uncertainty on a fleet wide level.

5.1. Mathematics of distributions

Before individual parameters and their respective distributions are discussed, the mathematics of these distributions needs to be understood. As will be shown later in this chapter, the probability density functions (PDFs) which are used are: uniform, triangular and normal. The mathematical equations of these probability density functions are presented in Table 5.1. Note that if the domain is specified it can be assumed that the probability density function is 0 outside the domain.

Table 5.1: Probability density functions for three different types of distributions [64].

Type of distribution	Probability density function	Domain
Uniform	$\frac{1}{b-a}$	$x \in [a, b]$
Triangular	$\frac{2(x-a)}{(b-a)(c-a)}$	$x \in [a, c]$
	$\frac{2(b-x)}{(b-a)(c-a)}$	$x \in (c, b]$
Normal	$\frac{1}{\sigma\sqrt{2\pi}e^{-\frac{1}{2}\left(\frac{x-\mu}{\sigma}\right)^2}}$	$x \in (-\infty, \infty)$

In the next sections the PDF distributions will be presented as follows. For a normal distribution it will be shown as [μ; σ] with μ as average and σ as standard deviation, for a triangular distribution it will be shown as [l; m; r] with l being the left boundary of the domain, m being the mode and r being the right border of the domain. Finally, a uniform distribution is presented as [l; r] with definitions the same as mentioned previously.

5.2. Information model uncertainties

The information model in Chapter 2 mainly captures the required information. Some data is added as it was missing based on flights numbers, aircraft types, used, departure airport and arrival airport. For the purpose of this emission inventory, no uncertainty is associated to this.

5.3. Performance model uncertainties

The performance model introduces several uncertainties which are discussed in more detail in the subsections underneath.

5.3.1. En-route multiplier

As mentioned earlier, 4D (latitude, longitude, altitude and time) trajectory information is not available. This means that the flight distance which is used is estimated using the great circle distance. Using the validation data from a renowned airline the uncertainty is quantified by means of Figure 3.4 and Figure 3.5 for short and long haul flights, respectively.

Based on Figure 3.4, it is decided that the probability density function (PDF) that resembles short haul flights' en-route multiplier the best, is a triangular distribution [64] for which the associated values are presented in Table 5.2.

For long haul flights the probability density function is determined based on Figure 3.5. A uniform probability density function [64] is used to resemble the uncertainty of this parameter. Its associated values are shown in Table 5.2.

Table 5.2: Uncertainties associated to the increase in distance with respect to the great circle distance.

Type of flight	Type of distribution	Associated PDF values
Short haul multiplier	Triangular	$[1.01; 1.13; 1.25]$
Long haul multiplier	Uniform	$[1.02; 1.05]$

5.3.2. Payload multiplier

Uncertainty is also associated to the payload multiplier, i.e. the fraction of maximum payload from BADA. The uncertainty associated to this parameter is divided between short haul flights and long haul flights.

For short haul flights the distribution is based on Figure 3.8. Based on the figure and the associated explanation in Section 3.1.4 the chosen PDF is a triangular distribution [64] with bounds as presented in Table 5.3.

For long haul flights the same approach is used, but based on Figure 3.9. The chosen PDF is a normal distribution with bounds presented in Table 5.3.

Table 5.3: Uncertainties associated to the payload fraction with respect to the maximum allowable payload.

Type of flight	Type of distribution	Associated PDF values
Short haul	Triangular	$[0.65; 0.74; 0.83]$
Long haul	Normal	$[0.69; 0.06]$

5.3.3. Engine aging

Another aspect which is taken into account is the increase in thrust specific fuel consumption due to engine aging. The performance of various engine components degrade [65] after use of an aircraft for years.

The functioning of engine components tend to degrade over time [66]. Research has provided the limits of this degradation of components. The limits of degradation of components is provided in Table 5.4. Surge is the process of aerodynamic instability due to air flow oscillatory motion in axial compressor direction [67]. The high turbine temperature is caused by in increase of the exhaust gas temperature from the combustion chamber [67], as also shown by the increase in combustor exit temperature.

The above mentioned uncertainties are limited to operational parameters due to engine aging. Moreover, uncertainty is also associated to the ambient conditions as the ambient conditions are estimated using a model called the International Standard Atmosphere (ISA). Although this is a widely used model, some uncertainty is still associated to it [14]. Summarized, the uncertainties of the different components and the temperature of the ISA are presented in Table 5.5. Note

Table 5.4: Degradation of component performance due to engine aging [66] [67].

Component	Limit	Reason
Fan mass flow	-5%	LPC surge
LPC mass flow	-8%	High turbine temperature
Fan efficiency	-5%	High turbine temperature
HPC efficiency	-4.5%	High turbine temperature
HPT efficiency	-5%	High turbine temperature
Combustor exit temperature	2.5%	Turbine life

that triangular distributions are chosen for component degradation as this maximum degradation only occurs at the end of life, hence very few aircraft/engines have to deal with those maximum degradations.

Table 5.5: Uncertainties associated to engine aging and atmospheric conditions [14] [66] [67].

Component/reason	Type of distribution	Associated PDF values
Fan mass flow multiplier	Triangular	$[0.95; 1; 1]$
LPC mass flow multiplier	Triangular	$[0.92; 1; 1]$
Fan efficiency multiplier	Triangular	$[0.95; 1; 1]$
HPC efficiency multiplier	Triangular	$[0.955; 1; 1]$
HPT efficiency multiplier	Triangular	$[0.95; 1; 1]$
Combustor exit temperature multiplier	Triangular	$[1; 1; 1.025]$
Ambient temperature correction	One-sided normal	$[0, 3.3K]$

Based on the uncertainties of individual sources, the governing uncertainty concerning thrust specific fuel consumption is estimated. This is based on fundamental equations provided by K. Hünecke [68] and T. Young [68]. The distributions presented in Table 5.5 are applied to four different engine models: CFM56 (used on Airbus A320 family and Boeing 737 family), Leap 1A (used on Airbus A320neo family), GE90-94B (used on Boeing 777 family) and GEnx-1B64 (used on Boeing 747-8 and Boeing 787 family). The performance of the CFM56 engine is obtained from research by D.A.R. Martins [69]. The rest of the engine information is obtained from simulations conducted using GasTurb[1].

The following figures show a Monte Carlo simulation (2000 simulations) of the four different engine models where the obtained $TSFC$ is normalized for the $TSFC$ of the components' nominal performance. Furthermore, the convergence of both the average $TSFC$ and the associated standard deviation is presented in the other graphs for all four engine models (Figure 5.1 - Figure 5.4) in Appendix A. Both parameters are calculated as follows [64]:

$$TSFC_{mean,j} = \frac{1}{n}\sum_{i=1}^{n} TSFC_i \tag{5.1}$$

$$\sigma_{TSFC,j} = \sqrt{\frac{1}{n}\left(\sum_{i=1}^{n} TSFC_i - TSFC_{mean,j}\right)^2} \tag{5.2}$$

[1] `https://www.gasturb.de/` (accessed 16-11-2022)

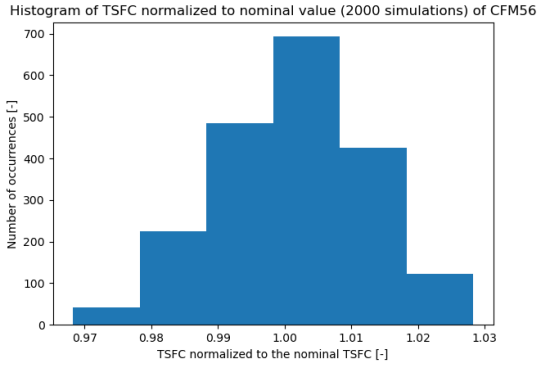

Figure 5.1: Histogram of normalized $TSFC$ for the CFM56 engine.

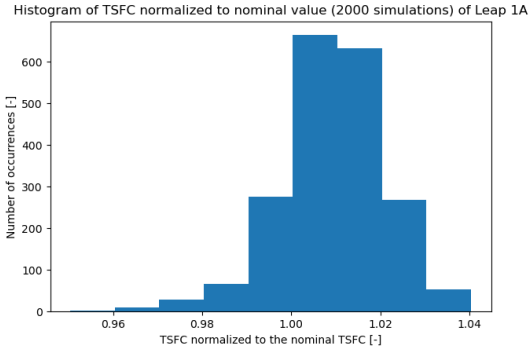

Figure 5.2: Histogram of normalized $TSFC$ for the Leap 1A engine.

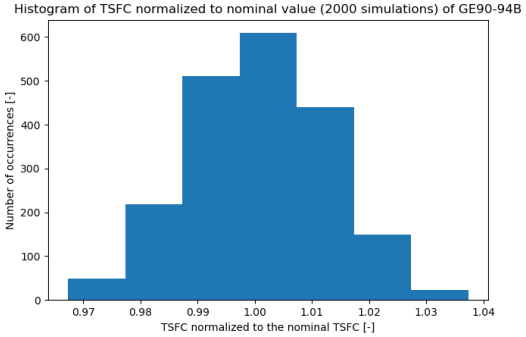

Figure 5.3: Histogram of normalized $TSFC$ for the GE90-94B engine.

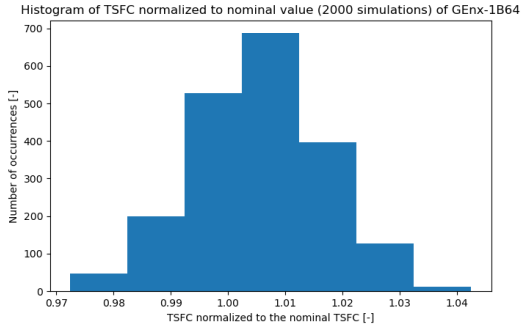

Figure 5.4: Histogram of normalized $TSFC$ for the GEnx-1B64 engine.

The results of all four engine models is presented numerically in Table 5.6.

Table 5.6: Results of $TSFC$ distribution by the monte carlo simulation due to engine component degradation.

Engine model	Mean $TSFC$ multiplier	Standard deviation $TSFC$ multiplier
CFM56	1.001	0.011
Leap 1A	1.009	0.012
GE90-94B	1.001	0.012
GEnx-1B64	1.005	0.011

The result is logical as it is clearly shown that engine aging increases the $TSFC$ on average. All four histograms (Figure 5.1, Figure 5.2, Figure 5.3, Figure 5.4) represent normal distributions. First, given random variable X, the linearity of expectation [70] provides:

$$E[aX + b] = aE[X] + b \tag{5.3}$$

where a and b are constants. Furthermore, the variance of random variables provides [70]:

$$Var(aX + b) = a^2 Var(X) \tag{5.4}$$

Lastly, the new expectation is simply the mean of the four averages. Using this, the properties of the $TSFC$ multiplier due to engine aging is provided in Table 5.7.

5.3.4. Operating empty weight

The uncertainty associated to the operating empty weight is directly taken from the analysis performed in Section 3.1.4, with $\sigma_{OEM} = 0.025$. To convert this to a multiplier distribution, the value of the standard deviation needs to be normalized with respect to the empty weight factor. This hence

Table 5.7: Uncertainty associated to engine aging.

Reason	Type of distribution	Associated PDF values
Engine aging $TSFC$ multiplier	Normal	$[1.004, 0.006]$

means a multiplier standard deviation $\sigma_{f,OEM} = \frac{0.025}{0.500} = 0.05$. This uncertainty takes into account the uncertainty due to the operating empty weight factor, different aircraft seating/galley/lavatories configurations and weight changes due to repairs and maintenance.

5.3.5. Fuel flow model uncertainty

The BADA database also introduces uncertainty. Extensive research by the FAA [71] has been conducted, using a Monte Carlo simulation, into the parametric uncertainty of elements within the BADA database. Ultimately, the uncertainty multiplier with respect to the fuel flow is required. Instead, the consulted research uses two sample route lengths (stage length 1 and stage length 4) for which the fuel consumption and nitrogen oxide emission are determined including all uncertainties. This uncertainty in itself cannot be used to determine confidence intervals as these intervals are not known for the other emitted species. Therefore, the distributions found in the paper [71] need to be converted to a fuel flow uncertainty due to the direct link between fuel flow and emission index discussed in Section 4.2. Two stage lengths, called stage length 1 and stage length 4, are used which are $350\ nm$ and $2200\ nm$ respectively classified according to Table 5.8.

Table 5.8: Discussed aircraft classes (data obtained from *Aviation Environmental Design Tool Version 2b Uncertainty Quantification Report* [71]).

Vehicle class	Maximum stage length	Representative stage length
Regional jet	3 $(1350\ nm)$	1 $(350\ nm)$
Large single aisle	5 $(3200\ nm)$	1 $(350\ nm)$
Small twin aisle	7 $(5200\ nm)$	4 $(2200\ nm)$
Large twin aisle	7 $(5200\ nm)$	6 $(4200\ nm)$

Based on the uncertainty in the parameters within the BADA computation, the uncertainty associated with representative stage lengths 1 and 4 is presented in Figure 5.5 and Figure 5.6, for large single aisles and Figure 5.7 and Figure 5.8 for small twin aisles, respectively, with number fuel consumption on the horizontal axis and number of simulation occurrences on the vertical axis. From these figures, one can conclude that the BADA database is relatively uncertain. Furthermore, since the distributions are skewed towards the left, on average, a flight uses more fuel compared to the observed mode from the distributions.

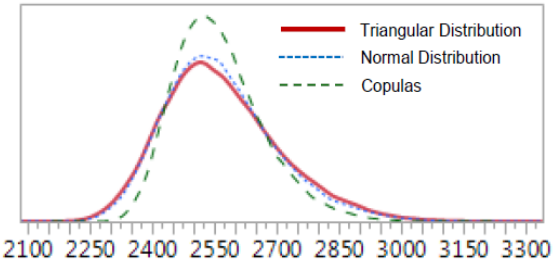

Figure 5.5: Uncertainty in fuel consumption for stage length 1 large single aisle aircraft (figure obtained from *Aviation Environmental Design Tool Version 2b Uncertainty Quantification Report* [71]).

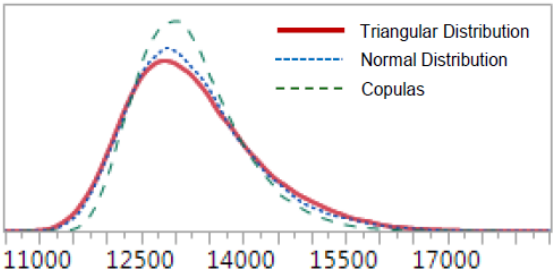

Figure 5.6: Uncertainty in fuel consumption for stage length 4 large single aisle aircraft (figure obtained from *Aviation Environmental Design Tool Version 2b Uncertainty Quantification Report* [71]).

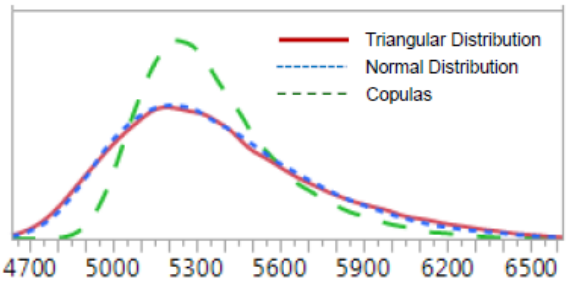

Figure 5.7: Uncertainty in fuel consumption for stage length 1 small twin aisle aircraft (figure obtained from *Aviation Environmental Design Tool Version 2b Uncertainty Quantification Report* [71]).

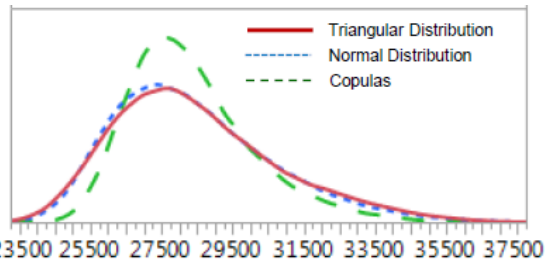

Figure 5.8: Uncertainty in fuel consumption for stage length 4 small twin aisle aircraft (figure obtained from *Aviation Environmental Design Tool Version 2b Uncertainty Quantification Report* [71]).

It is decided that the Airbus A320 and the Boeing 737-800 represent large single aisle aircraft (as mentioned in the research [71]) while the Airbus A330-200 and Boeing 767-300ER represent small twin aisle aircraft. The fuel flow multiplier distribution is presented in Table 5.9.

Table 5.9: Uncertainty associated with the BADA fuel flow model.

Type of uncertainty	Type of distribution	Associated PDF values
BADA multiplier fuel flow	Triangular	$[0.92; 0.98; 1.2]$

For brevity's sake, the distributions of only the Airbus aircraft are presented underneath, the Boeing distributions can be found in Appendix B.

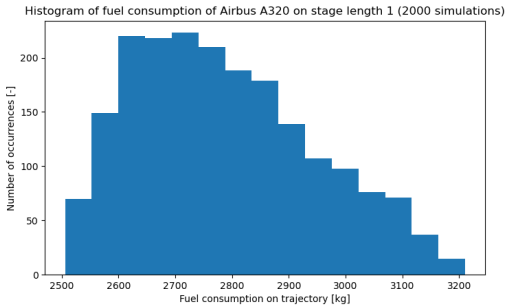

Figure 5.9: Uncertainty in fuel consumption for stage length 1 Airbus A320.

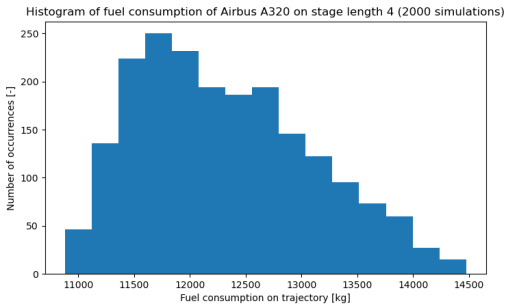

Figure 5.10: Uncertainty in fuel consumption for stage length 4 Airbus A320.

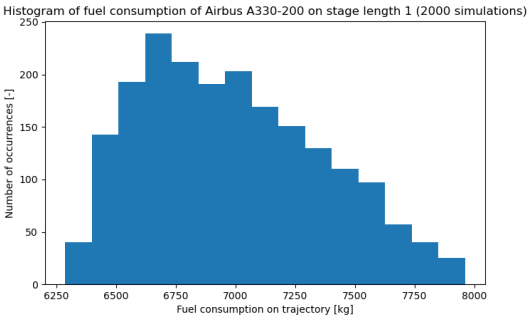

Figure 5.11: Uncertainty in fuel consumption for stage length 1 Airbus A330-200.

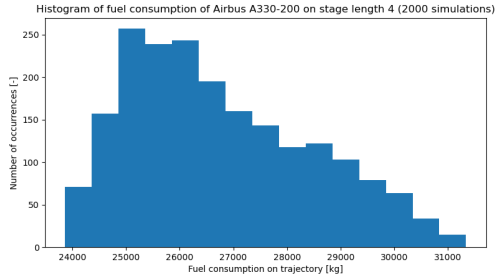

Figure 5.12: Uncertainty in fuel consumption for stage length 4 Airbus A330-200.

Note that the distributions show some dissimilarities due to the fact that the actual aircraft type used for the analysis is not provided in the research [71]. Still the distributions follow roughly the same lines. In addition, the mean and standard deviation of all discussed distributions is provided in Table 5.10.

Table 5.10: Mean and standard deviation for various aircraft for stage length 1 and stage length 4 (data for large single aisle and small twin aisle obtained from *Aviation Environmental Design Tool Version 2b Uncertainty Quantification Report* [71]).

Aircraft and stage length	Mean fuel use [kg]	σ [kg]
Airbus A320 stage length 1	$2,788$	158
Airbus A320 stage length 4	$12,323$	775
Airbus A330-200 stage length 1	$6,986$	376
Airbus A330-200 stage length 4	$26,774$	1696
Boeing 737-800 stage length 1	$2,968$	164
Boeing 737-800 stage length 4	$12,795$	842
Boeing 767-300ER stage length 1	$5,891$	332
Boeing 767-300ER stage length 4	$24,147$	1544
Reference large single aisle aircraft stage length 1	$2,568$	143
Reference large single aisle aircraft stage length 4	$13,248$	950
Reference small twin aisle aircraft stage length 1	$5,372$	366
Reference small twin aisle aircraft stage length 4	$28,470$	$2,352$

Note that there is some difference in the mean fuel consumption on the different trajectories but the standard deviations are not very different. This shows that the uncertainty placed on the fuel flow is quantitatively logical. Furthermore, the different mean fuel consumption can simply be explained by the non-mentioned aircraft types in the report and hence specific large single aisle/small twin aisle modelling is poor in this analysis.

In addition, the conclusion that can be drawn from the model fuel flow uncertainty distribution is in line with the analysis from Section 3.1.1 stating that, in general, the fuel flow estimated by BADA is lower compared to PianoX and openAP.

5.4. Emission model uncertainties

The use of fuel flow models creates uncertainty as these models cannot model the emissions perfectly. Furthermore, the constant emission indices contain parametric uncertainties. This sections aims to provide some understanding on the emission uncertainties associated to constant emission indices, the BFFM2 and the DLR/FOA fuel flow method.

5.4.1. Constant emission index uncertainty

The constant emission indices are limited to sulphur oxides and water vapor as the carbon dioxide emission index is corrected for the emission index of carbon monoxide. The uncertainties on the emission index of these two species are specified in Table 5.11 [29].

Table 5.11: Uncertainty associated with the constant emission index [29].

Type of uncertainty	Type of distribution	Associated PDF values
Emission index multiplier of sulphur oxides	Uniform	$[0.33; 2.33]$
Emission index multiplier of water vapor	Uniform	$[0.98; 1.02]$

5.4.2. BFFM2 emission index uncertainty

Analysing the uncertainty associated with the BFFM2 requires more insight into validation data and data obtained using the BFFM2. D. DuBois [50] has performed an extensive analysis on comparing the BFFM2, using the four ICAO data points, and the p3-T3 method. A comparison of the

calculated emission index of nitrogen oxides of the p3-T3 and BFFM2 methods is presented in Figure 5.13 for a variety of engines (including PW4090, Trent892, JT9D-7R4E and CFM56-7B).

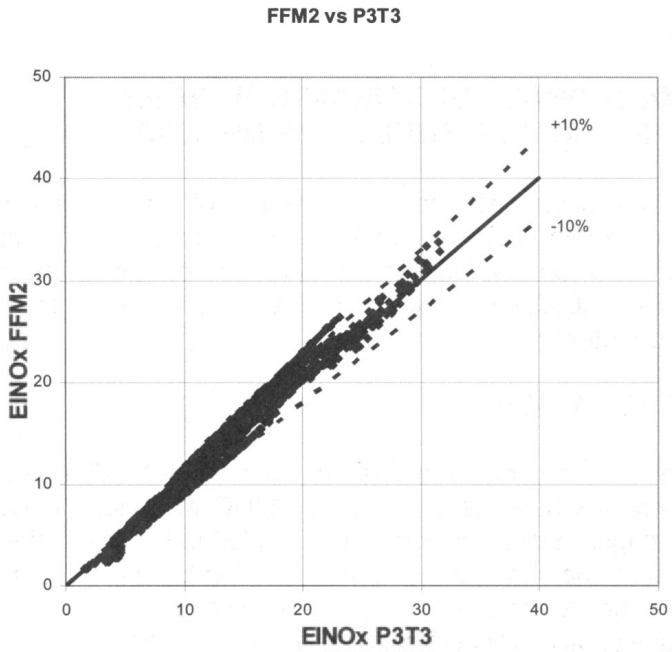

Figure 5.13: Comparison of emission index of NO_x obtained using BFFM2 and p3-T3 methods (figure obtained from *"Fuel Flow Method2" for Estimating Aircraft Emissions* [50]).

Note that all the datapoints in the graph represent different engines, operating conditions and thrust settings. In general, it can be concluded that the prediction by the BFFM2 compared to p3-T3 methods of the emission index of nitrogen oxides is good. The same graph has been created for the emission index of unburned hydrocarbons and carbon monoxide in Figure 5.14 and Figure 5.15 respectively.

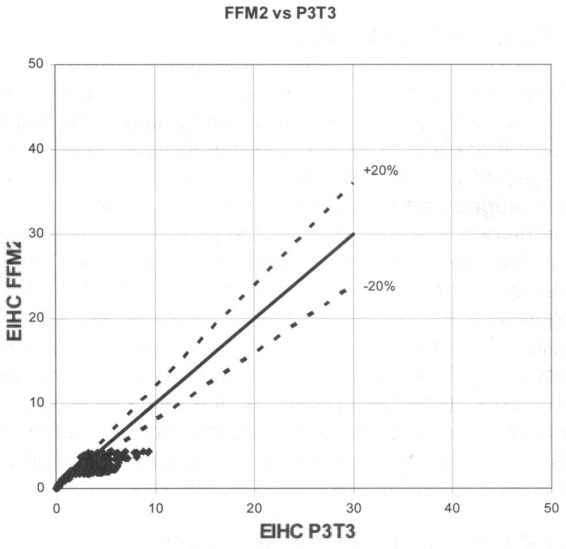

Figure 5.14: Comparison of emission index of HC obtained using BFFM2 and p3-T3 methods (figure obtained from *"Fuel Flow Method2" for Estimating Aircraft Emissions* [50]).

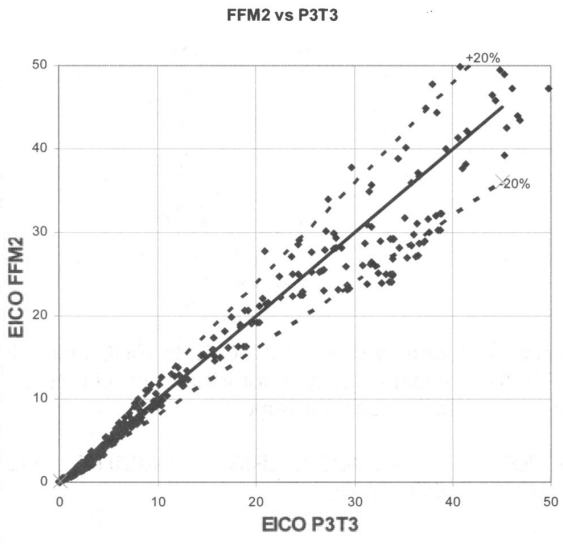

Figure 5.15: Comparison of emission index of CO obtained using BFFM2 and p3-T3 methods (figure obtained from *"Fuel Flow Method2" for Estimating Aircraft Emissions* [50]).

The figure describing the emission index of unburned hydrocarbons shows great deviation from the BFFM2, a significant underestimation occurs compared to the p3-T3 method. Based on the

above figures, the following distributions (Table 5.12) have been formulated as being suitable to describe the uncertainty associated with using the BFFM2.

Table 5.12: Uncertainty associated with the BFFM2.

Type of uncertainty	Type of distribution	Associated PDF values
Emission index multiplier of nitrogen oxides	Triangular	$[0.9; 1; 1.1]$
Emission index multiplier of unburned hydrocarbons	Triangular	$[0.9; 1; 1.8]$
Emission index multiplier of carbon monoxide	Triangular	$[0.8; 1; 1.2]$

Note that the uncertainty provided in the table also takes into account the uncertainty associated with the emission index of carbon dioxide as they are related by Equation 4.10.

5.4.3. DLR/FOA emission index uncertainty

No studies have yet been performed into estimating the uncertainty of the DLR/FOA black carbon model. However, the ICAO database can be used to estimate the uncertainty due to measurements. The database, for some engines, provides the standard deviation for smoke number. It has been decided to convert this standard deviation to a multiplication factor of the take-off emission index smoke number to derive the standard deviation distribution. The underlying reason is simple: due to the large differences in engine sizes in the database the standard deviations are very different, this is less the case looking at this multiplication factor $f_{BC,i}$. Hence, the first step is to normalize the standard deviation as described in Equation 5.5:

$$f_{BC,i} = \frac{\sigma_{SN,i}}{SN_{T/O,i}} \tag{5.5}$$

When all these factors are averaged from the entire database, the normalized standard deviation for black carbon is found. One condition is used, which is the fact that the multiplication factor $f_{BC,i}$ cannot exceed 1. A value of 1 would mean that a negative smoke number could be obtained in approximately 15% of the cases if a normal distributions is assumed. With this provided, the used distribution is shown in Table 5.13 based on the standard deviations in the ICAO database. Lastly, the standard deviation is only provided for the smoke number and not in the updated ICAO databank (explained in Section 4.2.2) where the actual soot emission indices are provided. This subsubsection also shows that the emission index/black carbon concentration at sea level is linearly related to the emission index/black carbon concentration at the considered altitude. This means that it does not matter whether the uncertainty found at sea level is taken into account before or after the extrapolation to the required altitude.

Table 5.13: Uncertainty associated with using the ICAO database for black carbon emission index.

Type of uncertainty	Type of distribution	Associated PDF values
Emission index multiplier of black carbon	Normal	$[1; 0.275]$

5.5. Monte Carlo Simulation

Based on all the discussed uncertainties a Monte Carlo simulation is conducted with 100 simulations, covering the first 2000 flights (with aircraft and airports available in the respective databases) in order to ensure convergence within each simulation. First, the simulation is conducted with all nominal variables as a baseline. Then, the uncertainties discussed in the rest of this chapter are applied for that simulation (thus the same uncertainty used for those 2000 flights). After every flight the respective parameters (either being the fuel consumption or one of the emission species) is converted to a multiplier by normalizing with the sum of fuel consumption/emissions until the applicable flight. Finally, after 2000 simulations a multiplier is obtained which has converged. These 100 multipliers are then presented in a histogram. Furthermore, the average of the final multipliers and their respective standard deviation is presented graphically to show that convergence has been achieved after 100 simulations. Lastly, all of the above is performed on a fleet wide basis as

well as for short haul flights ($< 1000\ nm$) and long haul flights separately. For brevity's sake this section only presents the graphs on a fleet wide basis while the short haul and long haul graphs are presented in Appendix D and Appendix E respectively.

5.5.1. Fuel consumption

Figure 5.16 shows the convergence of the mean fuel multiplier for the 2000 flights and 100 simulations. Even though it a diagram which is difficult to comprehend, clear convergence in every simulation is observed as the mean fuel consumption multiplier does not change significantly after approximately 500 flights. This result was observed by moving a three dimensional graph and hence the convergence is difficult to see in this two dimensional figure.

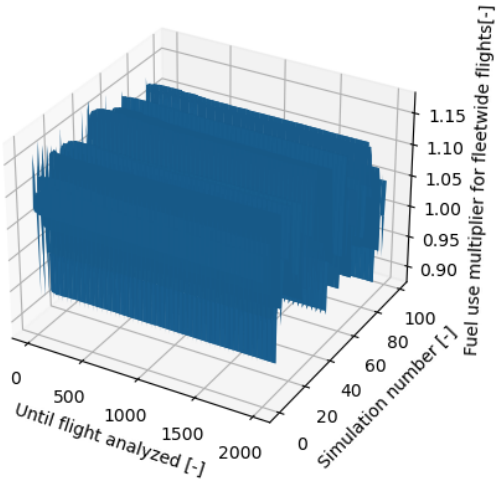

Figure 5.16: Convergence of mean fuel multiplier for all 2000 flights in all 100 simulations.

As convergence within each simulation is obtained the results of each simulation are presented. Figure 5.17 shows a histogram with the fuel consumption multipliers, while the convergence of the simulation is attached in Appendix C. Note that the quantitative results are presented at the end of this section.

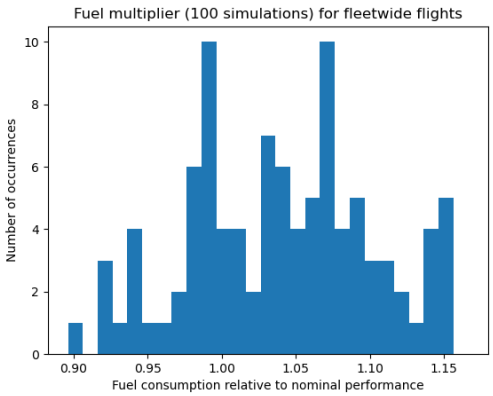

Figure 5.17: Histogram representing the fuel consumption multipliers of the 100 simulations.

5.5.2. Emissions

With similar reasoning the previous figures are constructed for the various emission species: carbon dioxide, carbon monoxide, unburned hydrocarbons, nitrogen oxides, sulfur oxides, water vapor and black carbon. This requires no substantial explanations and therefore the emission uncertainty multiplier graphs are simply presented underneath. Note that the convergence graphs are provided in Appendix C for brevity's sake.

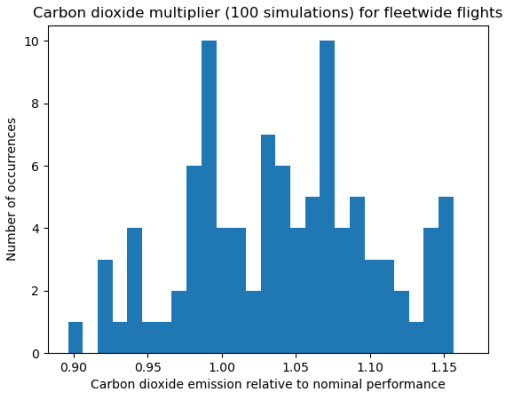

Figure 5.18: Histogram representing the carbon dioxide emission multipliers of the 100 simulations.

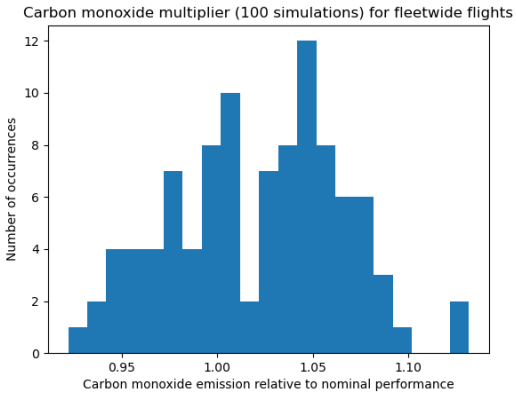

Figure 5.19: Histogram representing the carbon monoxide emission multipliers of the 100 simulations.

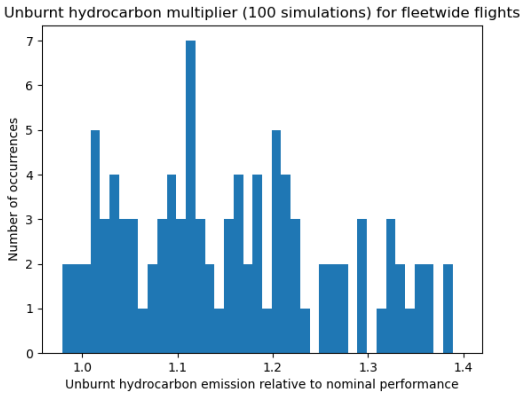

Figure 5.20: Histogram representing the unburned hydrocarbon emission multipliers of the 100 simulations.

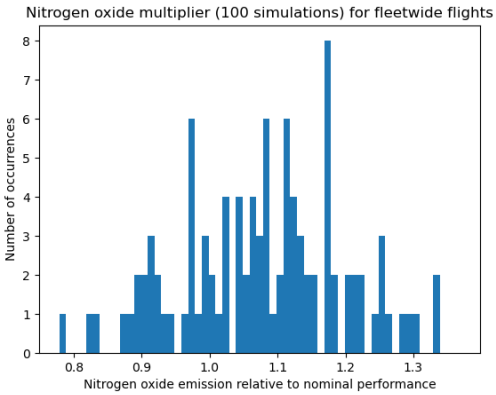

Figure 5.21: Histogram representing the nitrogen oxide emission multipliers of the 100 simulations.

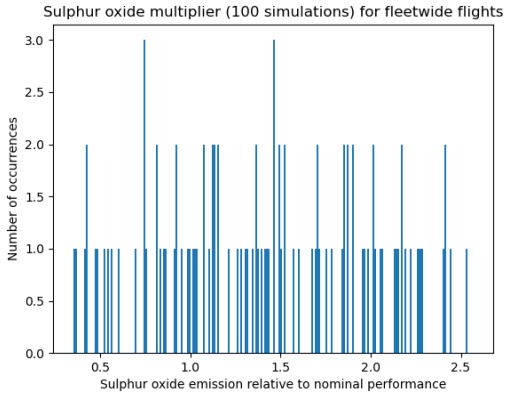

Figure 5.22: Histogram representing the sulfur oxide emission multipliers of the 100 simulations.

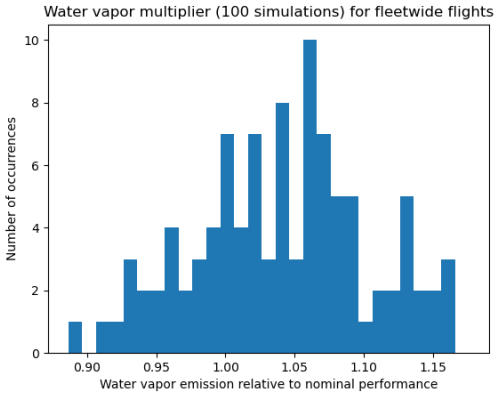

Figure 5.23: Histogram representing the water vapor emission multipliers of the 100 simulations.

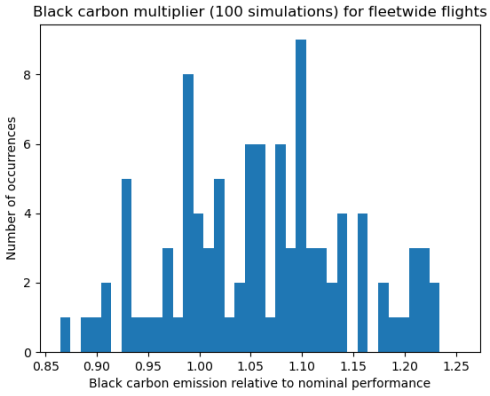

Figure 5.24: Histogram representing the black carbon emission multipliers of the 100 simulations.

5.5.3. Summary

Based on the obtained multipliers an increase or decrease in fuel consumption/emission compared to the model is obtained. This multiplier is used directly in the model to make a correction based on this uncertainty analysis. Furthermore, to account for the uncertainty, the concept of confidence intervals is used. The boundaries of this confidence interval are determined using Equation 5.6 [64]:

$$X = \overline{x} \pm z_{critvalue} \frac{\sigma}{\sqrt{n}} \tag{5.6}$$

where $\overline{x}$ represents the mean multiplier, $z_{critvalue}$ is a value dependent on the chosen confidence, σ represents the standard deviation and n represents the number of simulations. Four confidence intervals are used in this analysis:

- 50%
- 90%
- 95%
- 99%

The results of all species, mean multipliers and the four different confidence intervals are presented in Table 5.14 where the confidence intervals (CIs) are denoted as [left boundary; right boundary].

Note the similarities between CIs and mean multiplier of fuel, carbon dioxide and water vapor. Logically this is caused by the fact that the uncertainty of the emission index of water vapor is very low. In addition, the influence of the emission index of carbon monoxide to the emission index of carbon dioxide, as presented in Equation 4.10, is not substantial. Lastly, the sulfur oxide multiplier

Table 5.14: Mean multiplier and confidence intervals of total aviation fleet.

Species	Mean	50% CI	90% CI	95% CI	99% CI
Fuel consumption	1.042	[1.038; 1.047]	[1.032; 1.053]	[1.030; 1.055]	[1.026; 1.059]
CO_2 *emission*	1.042	[1.038; 1.047]	[1.032; 1.053]	[1.030; 1.055]	[1.026; 1.059]
CO *emission*	1.023	[1.019; 1.026]	[1.015; 1.030]	[1.013; 1.032]	[1.011; 1.035]
HC *emission*	1.158	[1.150; 1.166]	[1.140; 1.176]	[1.136; 1.180]	[1.129; 1.187]
NO_x *emission*	1.081	[1.073; 1.089]	[1.060; 1.101]	[1.057; 1.105]	[1.049; 1.113]
SO_x *emission*	1.424	[1.384; 1.464]	[1.326; 1.522]	[1.307; 1.542]	[1.269; 1.580]
H_2O *emission*	1.042	[1.038; 1.046]	[1.031; 1.053]	[1.029; 1.055]	[1.025; 1.059]
BC *emission*	1.063	[1.057; 1.069]	[1.048; 1.077]	[1.045; 1.080]	[1.039; 1.086]

is very high, this is directly caused by the very large uncertainty specified in Chapter 4. Due to these large multipliers very limited confidence is placed in the source of this uncertainty [29]. This is explained and verified in more detail in Chapter 6.

6

Verification & Validation

This chapter aims to verify and validate the performance and emission model. This will be done based on unit tests as system tests are barely possible since the emission inventories of 2019 have not yet been published. Note that in Chapter 7 a comparison will be made to previous emission inventory results. Furthermore, the overall mean uncertainties from Chapter 5 are used in this chapter rather than the individual uncertainties for short and long haul flights.

6.1. Verification

To find out whether the model makes sense a variety of verification tests are performed, which are all discussed extensively in the next subsections.

6.1.1. Payload-range diagrams

A simple method to evaluate whether the results from the performance model are logical is to verify the payload-range diagram from manuals with data from the code. This process has been performed for four aircraft models: Airbus A320, Airbus A340-600, Boeing 737-800 and Boeing 787-9. The reason behind these aircraft being that large variety was required between size, aircraft generation and number of engines. For brevity's sake, the payload-range diagrams, both from the model calculation and from the aircraft manual, of the Airbus A320 and the Boeing 787-9 are presented in Appendix F, the rest of the comparison will be discussed later in this chapter. The data required for the payload-range diagrams, maximum take-off mass ($MTOM$), maximum zero-fuel-mass ($MZFM$), operating empty mass (OEM), maximum fuel and maximum payload, is presented in Table 6.1.

Table 6.1: Payload-range parameters required for the analysis (all parameters obtained from their respective manuals).

Parameter	Airbus A320	Airbus A340-600	Boeing 737-800	Boeing 787-9
$MTOM$ *[kg]*	$78,000$	$365,000$	$79,000$	$254,000$
$MZFM$ *[kg]*	$64,300$	$242,000$	$62,732$	$181,436$
OEM *[kg]*	$42,600$	$177,000$	$41,413$	$128,850$
Max fuel [kg]	$18,729$	$153,082$	$23,817$	$101,444$
Max payload [kg]	$21,700$	$65,000$	$21,319$	$52,586$

The performance model has been re-constructed in such a way that the range and payload mass are both used as an input and the boundaries of the payload-range diagram are checked. If these are not violated, this point can be used and the range is increased by $10\ nm$. If a violation occurs, the range will be kept constant but the payload mass will be reduced by $100\ kg$. Logically, the starting point is the maximum payload and $10\ nm$ of range.

In addition it is important to distinguish between the methodology used for the emission code and the normal methodology for a payload-range diagram code. For a payload-range diagram

code it is not yet known what the limits of the aircraft performance are, in other words, the maximum range is not known. For an emission inventory code it is known that all the trajectories have been flown and are hence possible within the payload-range diagram boundaries.

As can be seen in Figure 3.11 an initial estimation is made of the take-off weight before a detailed analysis is performed of the flight. A condition is placed on this initial estimation that the initially calculated take-off mass cannot exceed the $MTOM$ (obtained from BADA) of the aircraft. Furthermore, the emission inventory code focuses on obtaining the trip fuel, for which contingency fuel is taken into account in the initially calculated take-off mass. To evaluate the maximum take-off mass limit, the empty mass, payload mass and trip fuel are summed because the original take-off mass is known to be too high due to the relatively high fuel flow assumed in the initial calculation. The effect of this on fuel flows during the flight (and hence emissions) has been considered low [4] but this has a substantial effect on the payload-range diagram. Similarly, to evaluate the maximum fuel capacity boundary, the trip fuel is compared to the maximum fuel capacity hence not taking into account the contingency fuel.

Please note that all the parameters from Table 6.1 can also be estimated using data from BADA. The only variable which is not specified in BADA is the maximum fuel capacity of an aircraft. This does not pose a problem as it is known that all flights in the *flightradar24* database have been flown and hence the maximum fuel capacity has not been a limiting factor.

To observe the effect of all the above reasoning, the payload-range diagrams obtained from *Python* provide four lines:

- Only trip fuel is considered, no reserves are taken into account. The masses used are from Table 6.1 to verify as accurately as possible the uncertainty associated with the fuel flow model and hence not have to deal with uncertainties presented in Section 3.1.4.
- To account for contingency fuels, 10% fuel is added as contingency fuel, the masses used are from Table 6.1.
- Only trip fuel is considered, all the masses are from BADA.
- The statement concerning no exceeding of the maximum take-off mass is deleted. This results in the kink being removed between the maximum take-off mass boundary and the maximum fuel capacity boundary.

Four payload-range diagrams, for the Boeing 737-800 and Airbus A340-600 both from the aircraft manual and obtained from the *Python* code, are presented in Figure 6.1a, Figure 6.1b, Figure 6.2a and Figure 6.2b respectively. The obtained payload-range diagrams from *Python* show some clear discrepancies from normal payload-range diagrams. A kink can be observed between the maximum take-off weight and maximum fuel capacity lines. This is caused by the maximum take-off weight statement in the code mentioned earlier. This is clearly visible as the green line does not show this effect. Fundamentally, this kink also represents a maximum take-off weight limit as two different definitions are used of take-off weight as mentioned earlier. Furthermore, please note that Figure 6.1a provides limits for various maximum take-off masses and various maximum fuel capacities. For the below analysis the values as presented in Table 6.1 are used.

For the Boeing 737-800 the maximum payload mass coming from the maximum zero-fuel mass is matched well for BADA data. The maximum take-off mass boundary is not strict enough, meaning that, according to *Python*, higher payload-range combinations are deemed possible. For all cases the maximum fuel capacity boundary predicted by *Python* is too far to the right. This makes sense if no reserves are taken into account, the case where 10% extra fuel (based on 5% extra during flight, holding and diversion fuel) is used is considered a relatively good match. In general, for the Boeing 737-800, it can be concluded that the performance is marginally overestimated by *Python* compared to the aircraft operating manual [72]. This conclusion is in line with statements formulated in Table 5.9, Figure 3.1 and Figure 3.2 but is limited due to the factor obtained from the uncertainty analysis.

For the Airbus A340-600 the maximum structural payload is modelled well by BADA. After that, the maximum take-off mass boundary is also modelled good by the red line. Unfortunately, due

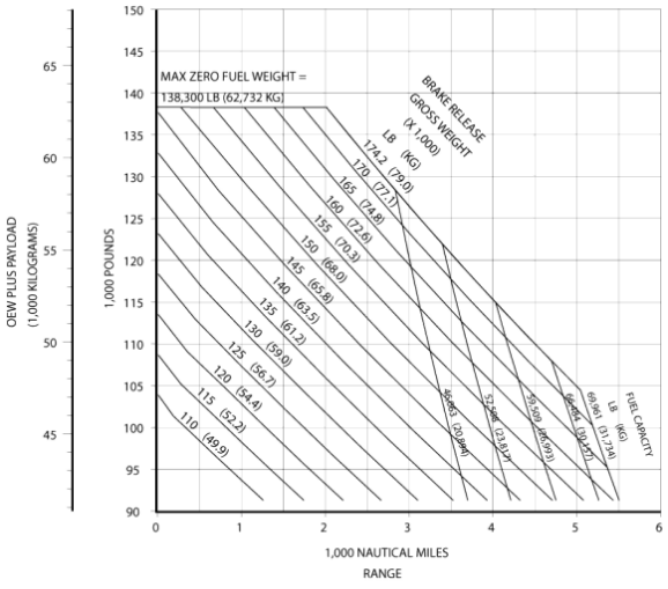

(a) Payload-range diagram of Boeing 737-800 from manual (figure obtained from *737 Airplane Characteristics for Airport Planning* [72]).

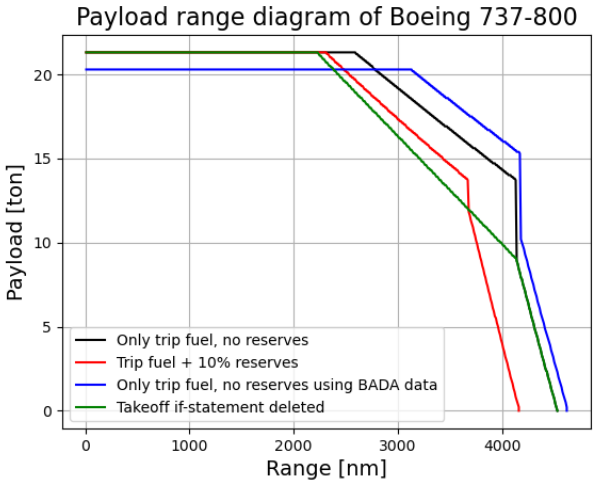

(b) Payload-range diagram of Boeing 737-800 obtained using *Python*.

Figure 6.1: Payload range diagrams of the Boeing 737-800.

to the different take-off masses definitions, the maximum fuel capacity boundary is not modelled very accurately. In general, especially for the non-ultra-long flights, the modelling of this aircraft type is considered excellent.

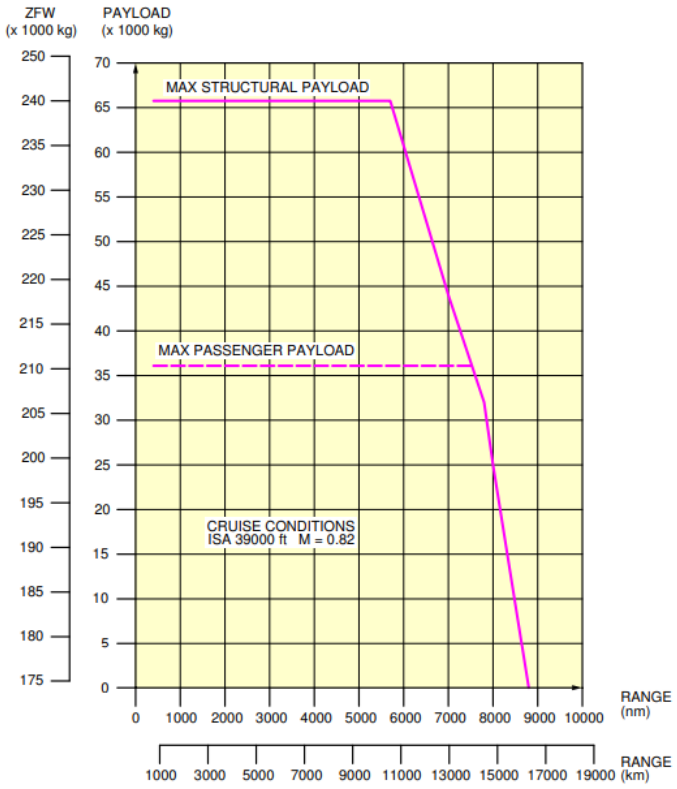

(a) Payload-range diagram of Airbus A340-600 from manual (figure obtained from *A340-500/-600 Aircraft Characteristics Airport and Maintenance Planning* [73]).

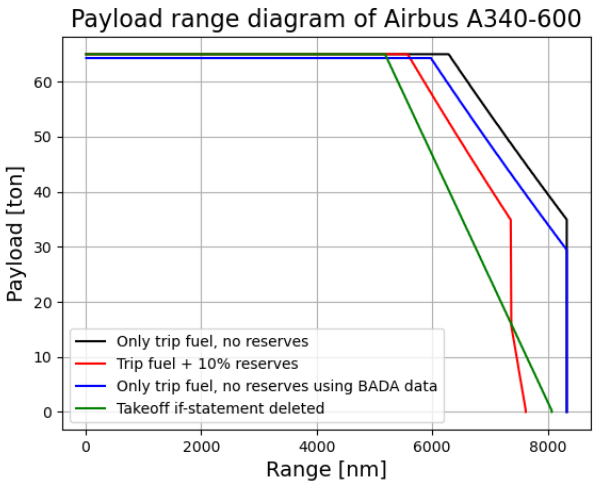

(b) Payload-range diagram of Airbus A340-600 obtained using *Python*.

Figure 6.2: Payload range diagrams of the Airbus A340-600.

The other two considered aircraft payload-range diagrams are presented in Appendix F but are discussed here. For the Airbus A320, the green line in the manual diagram should be consulted as the parameters used are associated to those conditions. Under all conditions, the maximum payload mass is marginally overestimated by *Python*. The maximum take-off mass boundary is matched well by the red line predicted by *Python*. This is similar to the maximum fuel capacity boundary for which the modelling is also excellent. In general, the A320 modelling, is considered very good.

The last considered aircraft is the Boeing 787-9. The maximum payload specified in BADA is too large compared to the aircraft manual. The transition from maximum payload boundary to maximum take-off boundary occurs too far to the right in *Python*. The transition to maximum fuel capacity also occurs slightly more to the right than required. Unfortunately, by reasons mentioned previously associated with the double definition of the maximum take-off mass, the maximum fuel capacity boundary is not modelled very well. In general, the modelling is good, but an underestimation of the fuel flow during flight is observed. This is in line with conclusions that can be drawn from Table 5.9, Figure 3.1 and Figure 3.2.

The modelling of Airbus aircraft is better compared to the Boeing aircraft. It is expected that this is associated with the age of the aircraft. The two Boeing aircraft are the youngest of the aircraft discussed in this section (especially the Boeing 787-9). BADA updates their database routinely and occasionally fuel flows are adapted based on new insights and customers' feedback [7].

6.1.2. Trip fuel burn comparison

To verify the calculated fuel burn from the current model, PianoX is used. For a large variety of aircraft and different ranges the fuel consumption is plotted for the PianoX data (including $+10\%$ and -0% deviation) and the *Python* model. This comparison is presented in Figure 6.3.

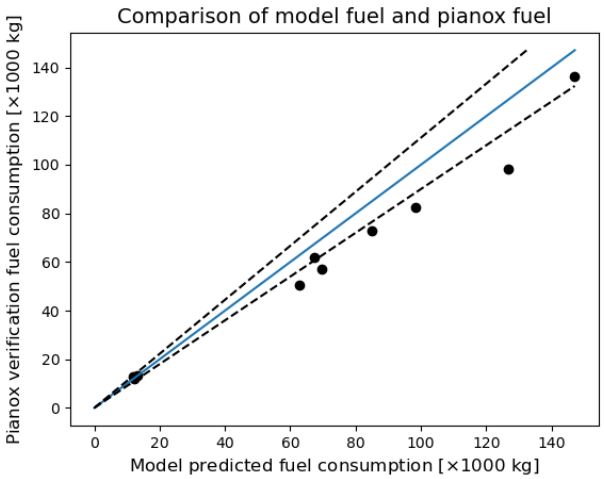

Figure 6.3: Verification of model results compared with PianoX data.

In general the trend is considered good but some discrepancies are found at higher fuel consumption. The model clearly predicts higher fuel consumption compared to the data obtained from PianoX, note that the baseline is different compared to previous comparisons as the mean uncertainty factor is applied. A conclusion about the validity will be drawn later, also consulting the validation with airline fuel consumption.

6.1.3. Emissions

It is very difficult to verify emissions from the model. The European Environment Agency (EEA) [74] provides a model which calculates the fuel consumption and various species of emissions of most aircraft as only a function of CCD (climb, cruise, descent) length. For a large variety of aircraft and mission lengths the fuel consumption and emission quantities are calculated. This subsection

aims to present all the results (including $+10\%$ and -0% deviation) and critically evaluate the found discrepancies. The used aircraft for this analysis are:

- Boeing 737-800, Boeing 747-400, Boeing 757-300, Boeing 767-400, Boeing 777-300ER and Boeing 787-9.
- Airbus A320, Airbus A330-200, Airbus A340-600, Airbus A350-900 and Airbus A380-800.
- Embraer E170 and Embraer E190.

Similar to this analysis, the EEA aims to predict the fuel consumption of a mission and the quantity of emissions of seven species: carbon dioxide, nitrogen oxides, sulphur oxides, water vapor, carbon monoxide, unburned hydrocarbons and black carbon.

The fuel consumption and carbon dioxide emissions of the discussed aircraft for various missions is presented in Figure 6.4 and Figure 6.5 respectively.

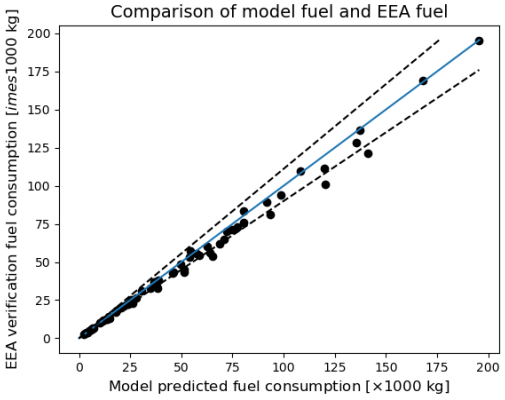

Figure 6.4: Comparison of fuel consumption prediction by the *Python* model and the EEA model.

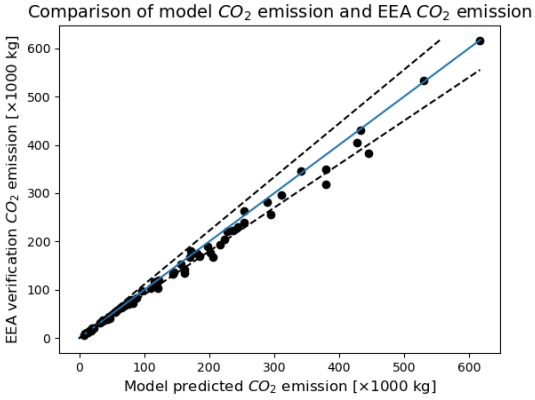

Figure 6.5: Comparison of carbon dioxide emission prediction by the *Python* model and the EEA model.

In the above figures there is a large similarity, this is due to the fact that the carbon monoxide emission index from Equation 4.10 is a very small number and hence the relation between the fuel consumption and the carbon dioxide emission is almost perfectly linear. Based on the comparison in Figure 6.4 and Figure 6.5 both parameters of the *Python* model are considered verified.

The next comparison is made between the nitrogen oxide emission predicted by *Python* and the EEA model and for sulphur oxide emissions predicted by both models. This comparison is presented in Figure 6.6 and Figure 6.7 respectively.

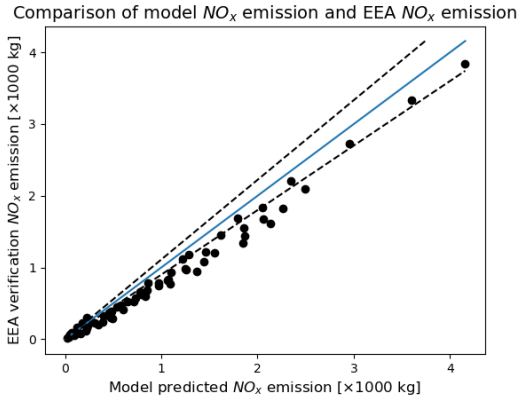

Figure 6.6: Comparison of nitrogen oxide emission prediction by the *Python* model and the EEA model.

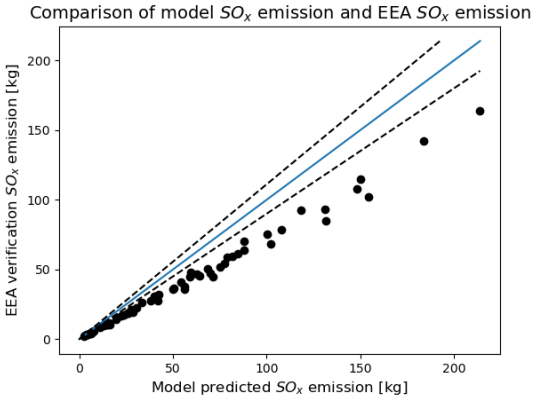

Figure 6.7: Comparison of sulphur oxide emission prediction by the *Python* model and the EEA model.

The nitrogen oxide emission in the *Python* model is computed using the BFFM2. Figure 6.6

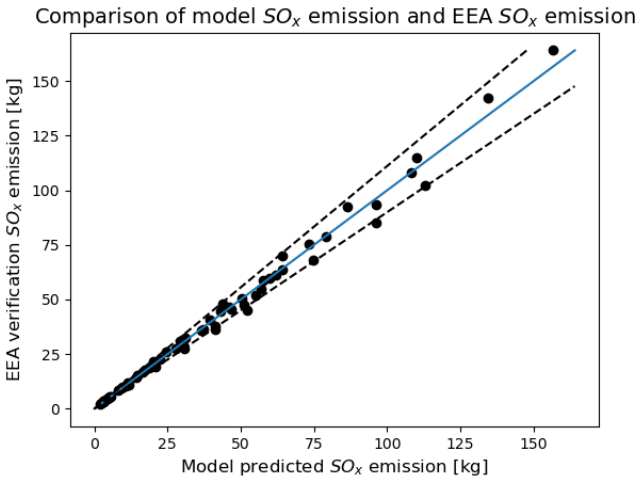

Figure 6.8: Sulphur oxide emission using constant emission index without mean uncertainty applied.

shows that the similarity is good (11% overestimation on average) compared to the EEA model. For sulphur oxides the shape of the graph is identical to Figure 6.4 as a constant emission index and constant uncertainty multiplication factor is used. For sulphur oxide emission the match is considered poor. This is caused by the large uncertainty probability distribution function as specified in Table 5.11. If this uncertainty is not taken into account, the result is presented in Figure 6.8.

Based on Figure 6.8 the match for sulphur oxides is considered excellent. Based on this reasoning it has been decided to neglect the very large uncertainty as specified in Chapter 5 and in stead use the uncertainty associated with the fuel consumption, hence maintaining the proportionality with the fuel consumption.

The next emission species which will be compared to the EEA model are water vapor and carbon monoxide. This comparison is presented in Figure 6.9 and Figure 6.10 respectively.

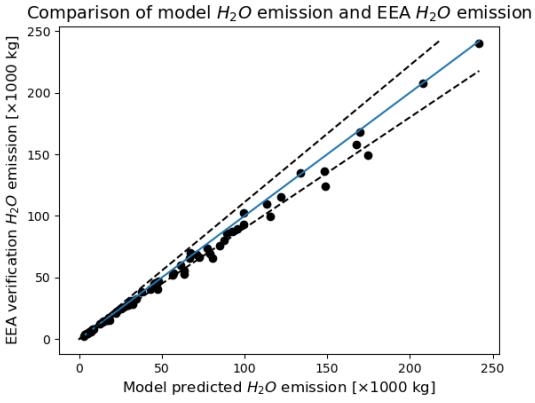

Figure 6.9: Comparison of water vapor emission prediction by the *Python* model and the EEA model.

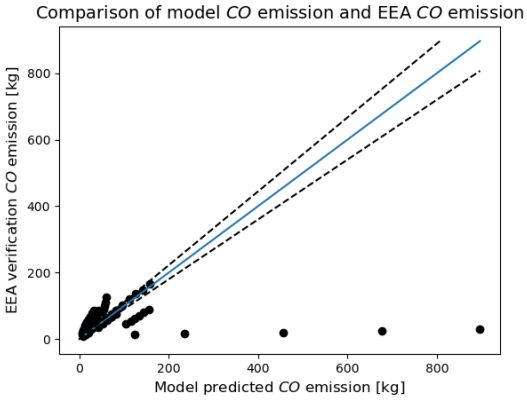

Figure 6.10: Comparison of carbon monoxide emission prediction by the *Python* model and the EEA model.

The verification of water vapor emission is relatively simple due to the fact that a constant emission index is used combined with low uncertainty. Therefore a similar line of reasoning applies as for sulphur oxides. The carbon monoxide emission shows a very large deviation from the values provided by the EEA. The datapoints which show the strong discrepancy all belong to the points associated with the Boeing 737-800. BADA states that the most often used engine model for this aircraft is the CFM56-7B26/27 while the EEA is more specific stating that the 8CM051 is

used which belongs to the same family. Due to the line of reasoning provided in Section 3.1.5 about limiting the length of the name of an engine, the engine that the *Python* program selects is the CFM56-7B26/2. This engine has significantly different emission indices belonging to carbon monoxide emission. Specifically for this case, the figure has been reconstructed and is shown in Figure 6.11 where the exact same engine is used as the EEA uses.

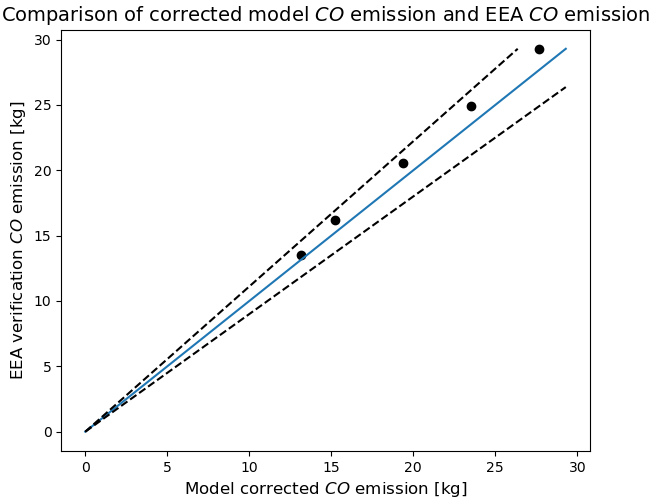

Figure 6.11: Comparison of carbon monoxide emission for the corrected Boeing 737-800 datapoints.

In the diagram the match is considered very good. The easiest method to correct this in the code is to adapt the BADA file and specify the engine model specifically as the CFM56-7B26 which corresponds to the 8CM051 model used by the EEA. This is therefore not considered a shortcoming in methodology. Logically, the previous results for the Boeing 737-800 make no sense as they are higher than the highest carbon monoxide emission of the biggest airplanes (by a factor of approximately 10). The result, however, could be significant as the Boeing 737-800 is a very popular aircraft worldwide.

The last comparison to be made is for unburned hydrocarbons and black carbon. This comparison is presented in Figure 6.12 and Figure 6.13 respectively.

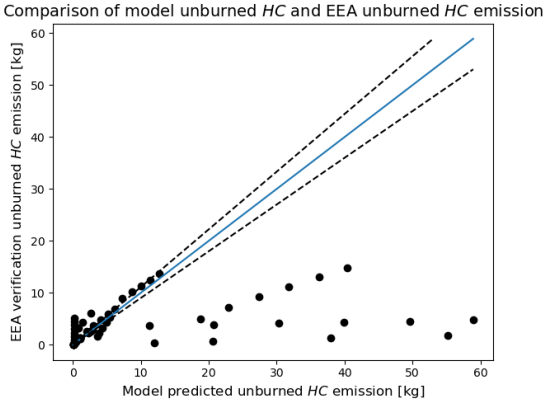

Figure 6.12: Comparison of unburned hydrocarbons emission prediction by the *Python* model and the EEA model.

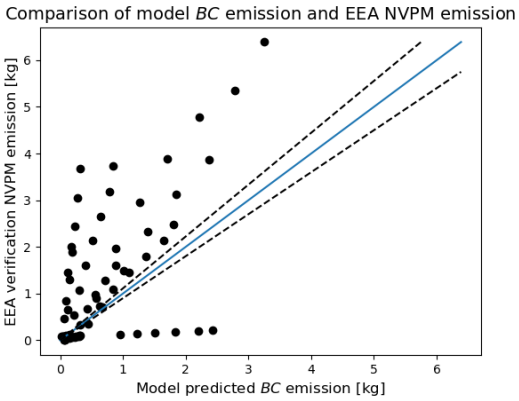

Figure 6.13: Comparison of black carbon emission prediction by the *Python* model and the EEA model.

In the above figures large inconsistency is visible, especially for the unburned hydrocarbons. This discrepancy is caused by the fact that the wrong engine is selected in the *Python* code for

three aircraft types: Boeing 747-400, Boeing 757-300 and Airbus A330-200. Strangely, various engine models are available more than once in the ICAO emission database. The EEA model uses the model which is lowest in the list while the *Python* program selects the model which is found earliest, starting its search at the beginning of the list. If this is changed, and the same engine model as specified by the EEA is used in the *Python* program, the results change significantly. The corrected results are presented in Figure 6.14.

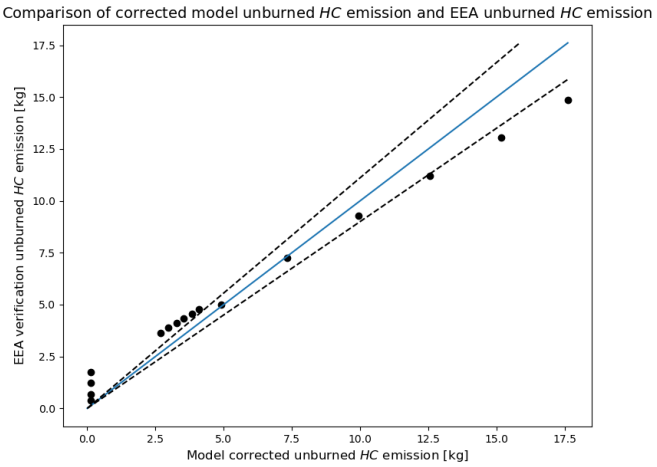

Figure 6.14: Comparison of unburned hydrocarbon emission for the corrected Boeing 747-400, Boeing 757-300 and Airbus A330-200 datapoints.

Based on the above figure, the match is considered very good. Furthermore, it has been decided to change the *Python* code permanently to start the search for the correct engine model at the bottom of the list moving up, rather than vice versa.

For the black carbon emissions, the process is different. The EEA provides the non-volatile particulate matter emission while the *Python* program predicts the black carbon emission. Black carbon belongs to the family of non-volatile particulate matter and makes up a large part of it [75]. This thus means that, in principle, the emission of black carbon should always be lower than the emission of non-volatile particulate matter. It is clearly visible, from Figure 6.13, that this is true in most cases. No explanation has been found for the cases where the model predicts a higher black carbon emission than the EEA model's predicted non-volatile particulate matter emission (this is the case for the Boeing 747-400 datapoints).

6.2. Validation

For the purpose of validating the program the data mentioned previously from the renowned airline is compared to the model. This comparison is presented in Figure 6.15 and Figure 6.16. Figure 6.15 presents a comparison of the validation data and data from the *Python* program. Rather than using the multipliers for payload mass and increase in great circle distance as specified in Chapter 3, the actual payload mass and ground distance of the validation flights were used. The difference between the program fuel and model fuel is thus defined as:

- Program fuel: using the actual flown distance and actual payload from airline validation data, the fuel consumption is obtained.
- Model fuel: using the assumptions from this report on payload fraction and en-route distance multiplier, the fuel consumption is obtained.

With this provided, the actual program can be validated. Figure 6.16 presents a comparison of the validation data and the model data (thus using all multipliers provided in Chapter 3). This figure is thus more representative in order to validate the entire model, including all assumptions.

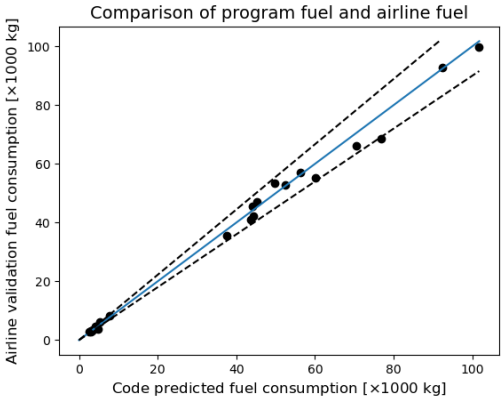

Figure 6.15: Fuel consumption of the program with the same travelled ground distance and payload weight as the validation data.

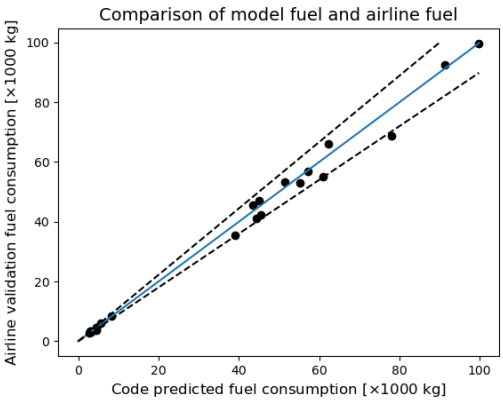

Figure 6.16: Fuel consumption of the model compared to validation data.

In both figures the match is considered good. To provide more understanding of this, some statistics are provided in Table 6.2. Note the difference between the word program and model: program is only the *Python* program which uses the same payload mass and ground distance as the validation data while model means that all assumptions mentioned in this report are included in the analysis.

Table 6.2: Validation of program and model.

Type of flight	Program fuel compared to validation [%]	Model fuel compared to validation [%]
Short haul	-1.1	-0.8
Long haul	2.3	2.7
Overall	0.8	1.2

The values from Table 6.2 are considered good and the program is therefore considered validated.

7

Results

As the model has been verified and validated it is ready to find the results of the total year. These results are obtained by analyzing a complete week and multiplying the results of this week with two factors: a factor to account for only analyzing one week ($365/7$) and one factor to account for not having the exact mean number of flights in this week ($808,637/806,631$).

7.1. Considered flight information

As the simulation has been conducted some information about all flights is provided. As mentioned earlier, not all aircraft models are known by the ICAO databases and not all airports are provided in the *flightradar24* databases. Only jet aircraft are considered for this analysis, due to the inability of the BFFM2 to model emission indices of non-jet aircraft. In addition, the *flightradar24* data also covers helicopter data. The aircraft/helicopters which are not analyzed but were provided in the *flightradar24* data are listed in Appendix G. Furthermore, the location of some airports is not provided in the consulted database. Some information concerning these inabilities is provided in Table 7.1. Note that some flights both have an aircraft and airport which are unavailable.

Table 7.1: Number of (unavailable) flights in representative week.

	Number of flights
In representative week	928,840
Aircraft not available	275,925
Departure/Arrival airport not available	139,719
Actual analyzed flights	555,209

7.2. Geographical emissions

As explained in Chapter 3 and Chapter 4 the point performance of the aircraft is used to estimate the trajectory performance along the flight trajectory. The emission on this small trajectory is attributed to the beginning point of the small trajectory in such a way that the emissions are stored in a 3D grid. The limit on cruise ceiling altitude was set at $50,000\ ft$. All emission that occurs above this altitude is attributed to the upper slice of the 3D grid. By visual inspection in the code it was found that this did not occur more than 500 times and is therefore considered insignificant. The resolution for all figures is $1^\circ \times 1^\circ \times 1000\ ft$.

7.2.1. Fuel consumption

The global fuel consumption is presented in Figure 7.1 (enlarged in Appendix H) and the summation per flight level is presented in Figure 7.2. A darker color reflects higher fuel consumption.

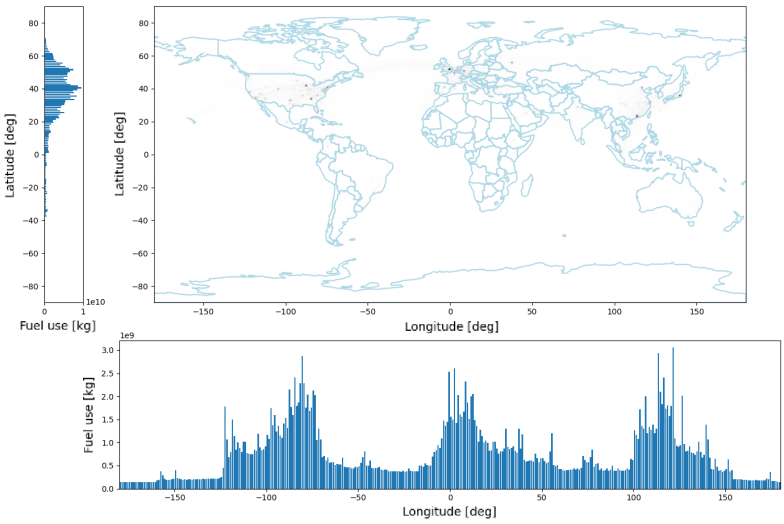

Figure 7.1: Fuel consumption on a worldwide map also depicting the summation per longitude and latitude.

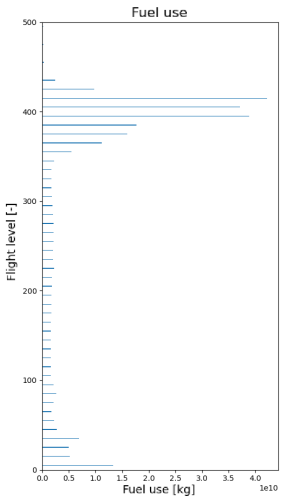

Figure 7.2: Fuel consumption as a function of flight level.

From Figure 7.1 it is very clear that most emission occurs in roughly three geographical areas: North-America, Europe and South-East Asia. In addition, significantly less fuel burn takes place on the southern hemisphere compared to the northern hemisphere which is a logical result of the size of economies and prosperity of the respective continents. Finally, from Figure 7.2, it becomes clear that most of the fuel is burned at relatively high altitudes. This is a logical result as most of the flights have a significantly longer cruise segment compared to their climb/descent segment. This is presented in more detail in Section 7.4.

7.2.2. Carbon dioxide emission

The global map and summations per latitude/longitude are presented in Figure 7.3 while the summations per flight level are presented in Figure 7.4.

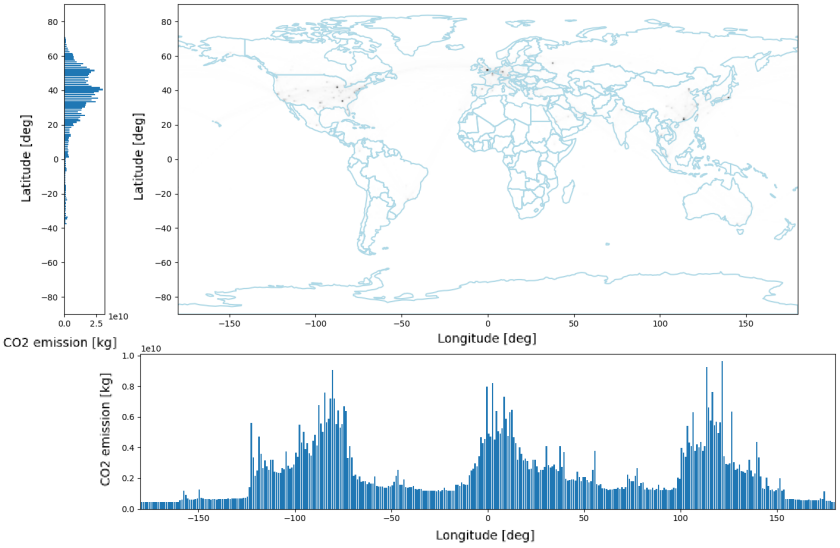

Figure 7.3: Carbon dioxide emission on a worldwide map also depicting the summation per longitude and latitude.

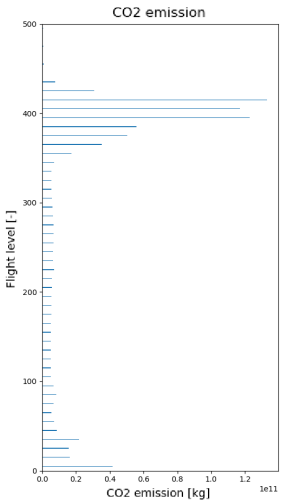

Figure 7.4: Carbon dioxide emission as a function of flight level.

The figure closely resembles the fuel consumption figure as the influence of emission index of carbon monoxide in Equation 4.10 is very limited. The three main regions for air traffic are, again, clearly distinguished by the large peaks of carbon dioxide emission.

7.2.3. Carbon monoxide

The carbon monoxide emission on a global scale is presented in Figure 7.5 and the summation of emissions per flight level is presented in Figure 7.6.

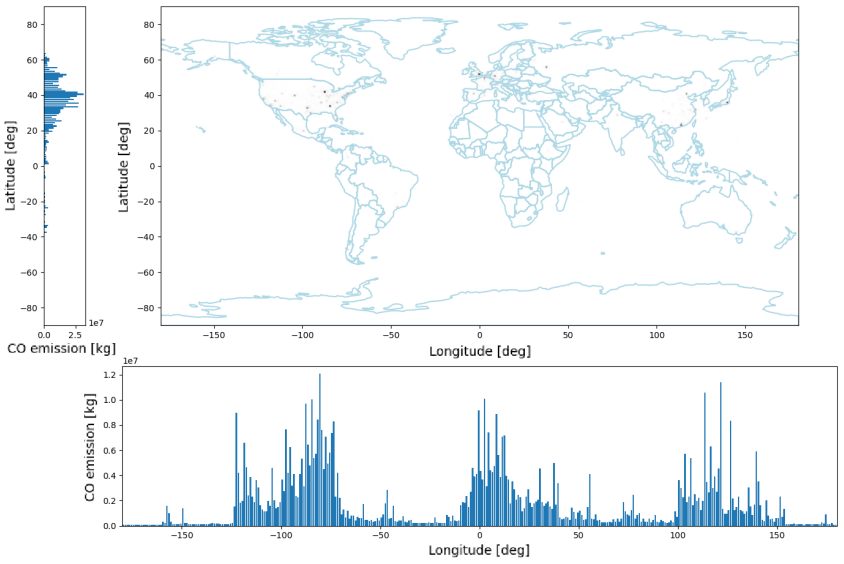

Figure 7.5: Carbon monoxide emission on a worldwide map also depicting the summation per longitude and latitude.

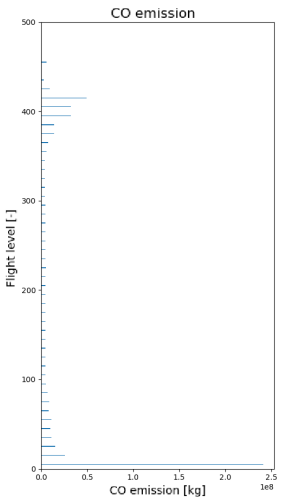

Figure 7.6: Carbon monoxide emission as a function of flight level.

These figures are significantly different compared to the fuel consumption and carbon dioxide figures. As clearly seen in Figure 7.6 most of the carbon monoxide emission occurs at very low altitudes. This is hence attributed to the LTO cycles and is mostly emitted in the vicinity of airports. From Figure 7.5 clear peaks are visible rather than a relatively rounded distribution. These large peaks resemble the main airport hubs located at those longitudes.

7.2.4. Unburned hydrocarbons

The unburned hydrocarbon emission on a global scale is presented in Figure 7.7 and the summation per flight level is presented in Figure 7.8.

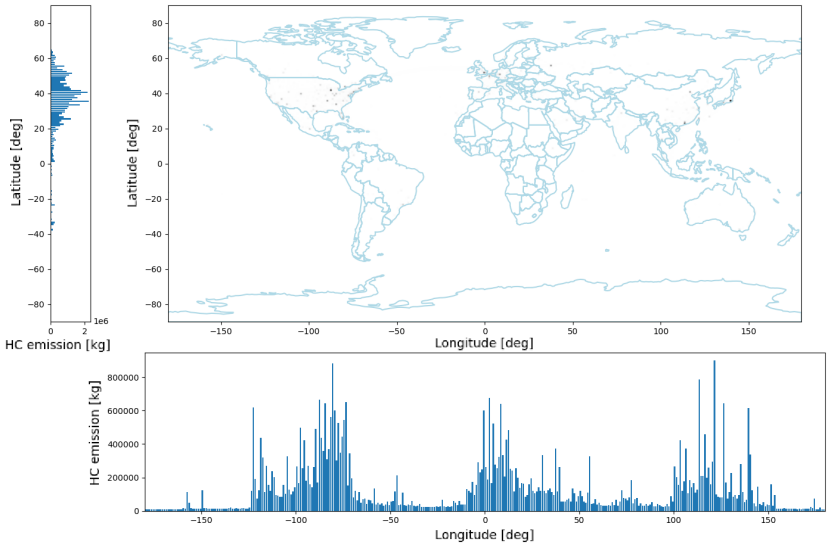

Figure 7.7: Unburned hydrocarbon emission on a worldwide map also depicting the summation per longitude and latitude.

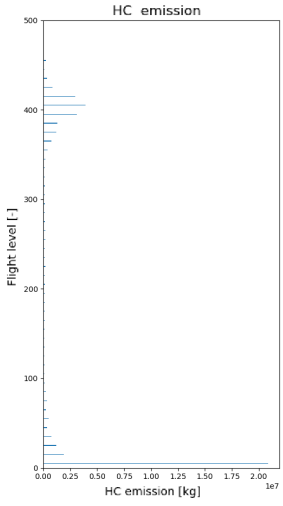

Figure 7.8: Unburned hydrocarbon emission as a function of flight level.

From Figure 7.8 one can conclude that most HC emission occurs in the vicinity of airports

during the LTO cycle. The clear peaks in Figure 7.7 resemble the main airport hubs such as London, Amsterdam, Paris and Frankfurt close to $0°$ longitude.

7.2.5. Nitrogen oxides

The emission of nitrogen oxides on a global scale is presented in Figure 7.9 and the summation of nitrogen oxide emission per flight level is presented Figure 7.10.

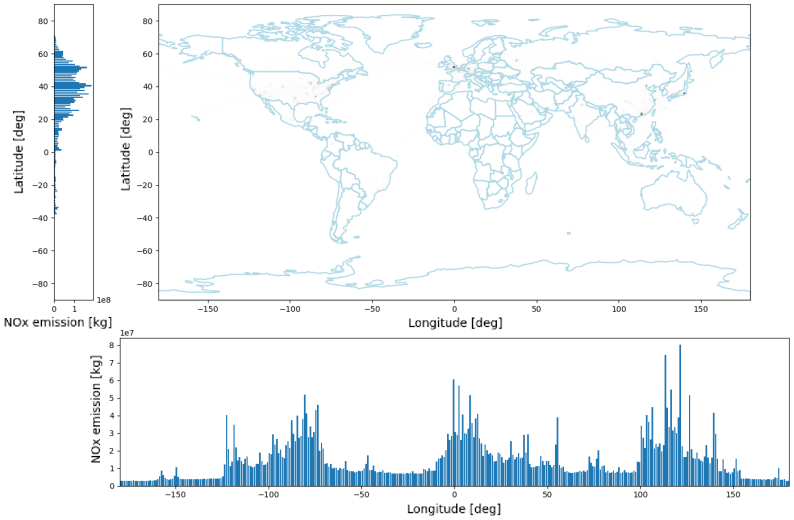

Figure 7.9: Nitrogen oxide emission on a worldwide map also depicting the summation per longitude and latitude.

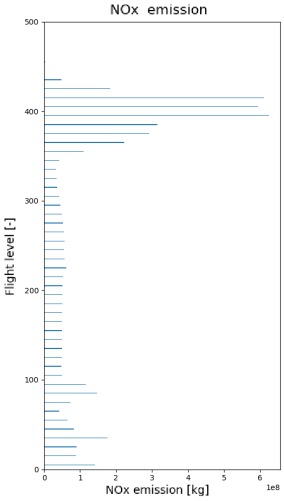

Figure 7.10: Nitrogen oxide emission as a function of flight level.

Interestingly, most nitrogen oxide emission occurs at cruise altitude. The emissions occurring on the north-Atlantic corridor are significant but most emission still occurs in North-America, Europe and South-East Asia. This is due to the relatively large influence of regional, short, and medium haul flights which do not cover very large distances.

7.2.6. Sulfur oxides

The global emission of sulfur oxides and the summation of sulfur oxide emission per flight altitude is presented in Figure 7.11 and Figure 7.12 respectively.

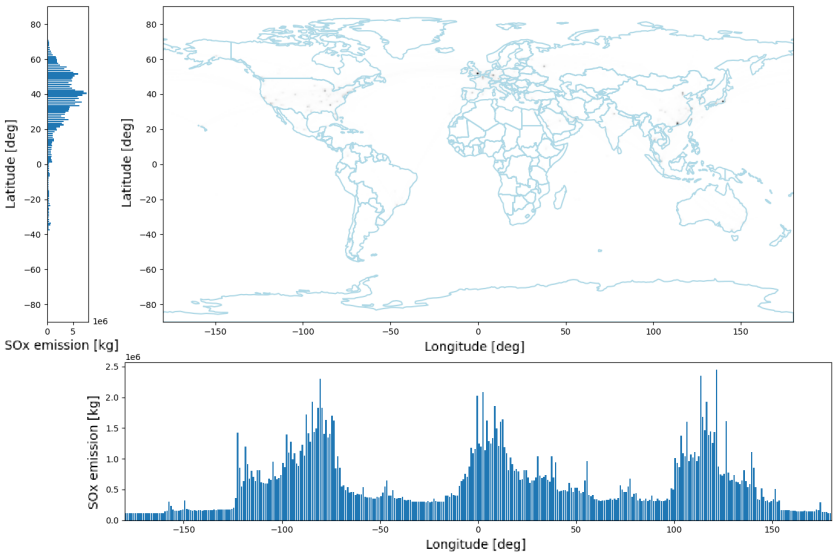

Figure 7.11: Sulfur oxide emission on a worldwide map also depicting the summation per longitude and latitude.

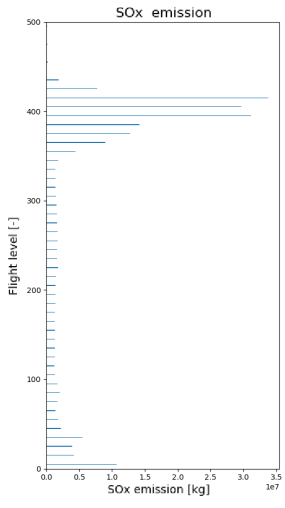

Figure 7.12: Sulfur oxide emission as a function of flight level.

The shape of the above diagrams closely resembles the shape of the fuel consumption and carbon dioxide figures. This is a logical result due to the constant emission index caused by the assumed constant sulfur content in kerosene.

7.2.7. Water vapor

The emissions of water vapor on a global scale are presented in Figure 7.13 with the summation per flight level presented in Figure 7.14.

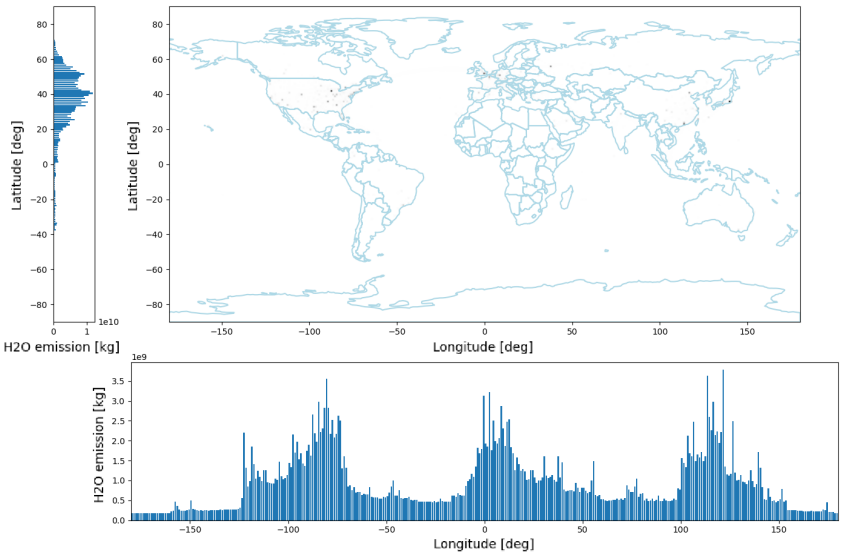

Figure 7.13: Water vapor emission on a worldwide map also depicting the summation per longitude and latitude.

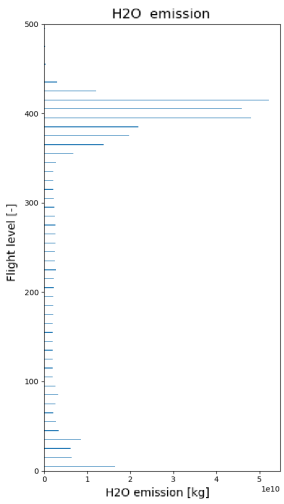

Figure 7.14: Water vapor emission as a function of flight level.

The figure closely resembles the fuel consumption figures due to the constant emission index of water vapor.

7.2.8. Black carbon

The emission of black carbon geographically is presented in Figure 7.15 with the summation per flight level presented in Figure 7.16.

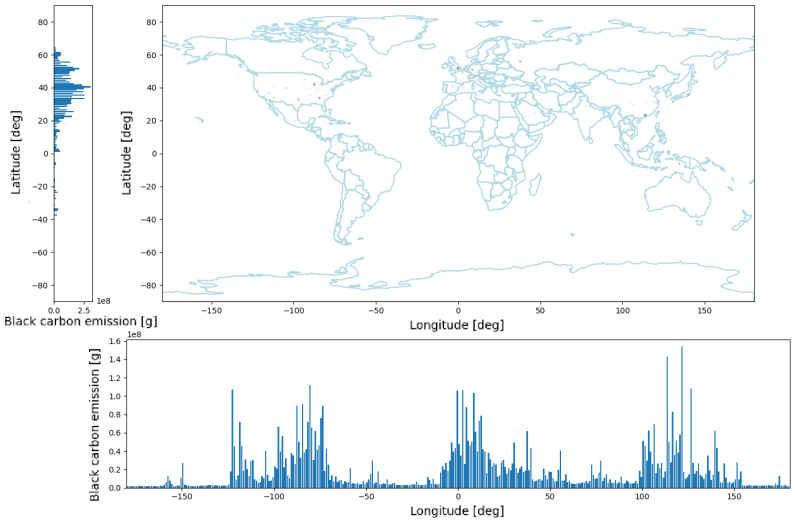

Figure 7.15: Black carbon emission on a worldwide map also depicting the summation per longitude and latitude.

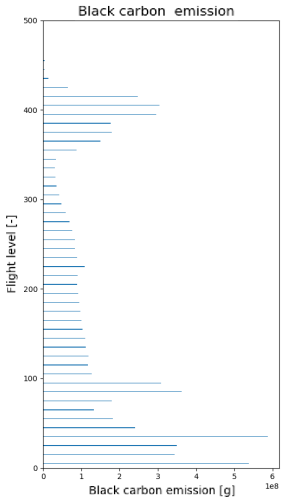

Figure 7.16: Black carbon emission as a function of flight level.

Most black carbon emission occurs at lower flight levels (below $10,000\ ft$). This is especially

important for local air quality as black carbon emission and concentration is strongly correlated with heart disease and lung conditions [47]. The black carbon emission occurring at cruise altitude, which is a significant amount concluding from Figure 7.16, is important for cloud formation combined with the emission of water vapor [45].

7.3. Confidence

Based on the uncertainty analysis certain confidence is placed in the results. A distinguishment was made between four different confidences but for brevity's sake only 90% confidence is used in this section. The conversion to different confidences can easily be made using the factors provided in Table 5.14. The nominal fuel consumption and emissions with the lower and upper boundary of the 90% confidence interval are presented in Table 7.2.

Table 7.2: Quantity of fuel consumption and emissions with 90% confidence for the year 2019.

Species	Nominal	Lower boundary	Upper boundary
Fuel [Tg]	272.0	269.4	274.9
CO_2 *[Tg]*	857.1	848.9	866.1
CO *[Gg]*	634.2	629.2	638.5
HC *[Gg]*	45.6	44.9	46.3
NO_x *[Tg]*	5.3	5.2	5.4
SO_x *[Gg]*	217.6	215.5	219.9
H_2O *[Tg]*	336.3	332.7	339.9
BC *[Gg]*	6.8	6.7	6.9

Please note that certain uncertainties are not addressed in this analysis as listed below:

- Uncertainty due to not having all aircraft in the database analyzed.
- Uncertainty due to missing out on analysis of some flights from unknown airports.
- Uncertainty associated to deleting the flights where departure and arrival airport is the same.
- Uncertainty of *flightradar24* possibly missing some flights.
- Uncertainty associated with complementing the database as presented in Figure 2.4.
- Uncertainty due to the use of representative aircraft when BADA performance file is unavailable.
- Uncertainty due to engine modelling using the engine model provided by BADA and not the actual aircraft model on the aircraft.
- Uncertainty in different kind of flights (more short/long haul flights) outside the representative week.

7.4. Aircraft categories

In addition to the total fuel consumption and emissions the program provides the fuel consumption and emissions for five categories of aircraft: regional, short haul, medium haul, long haul and very long haul. Note that these are not the same as the categories of aircraft distinguished by ICAO which distinguishes mainly based on aircraft speed. The aircraft categories in this research are distinguished as follows:

- Regional: less than $300\ nm$.
- Short haul: between $300\ nm$ and $1,000\ nm$.
- Medium haul: between $1,000\ nm$ and $2,000\ nm$.
- Long haul: between $2,000\ nm$ and $4,000\ nm$.
- Very long haul: more than $4,000\ nm$.

The confidence intervals can also be used for this data, however the short haul confidence intervals should be used for regional and short haul flights while the long haul confidence intervals should be used for the other data. The nominal fuel consumption and emissions of the five categories of aircraft (and the total) is presented in Table 7.3.

Interestingly enough, short haul flights make up a considerable portion of the carbon monoxide and black carbon emission. This is caused by the relatively high emission index of these species

Table 7.3: Quantity of fuel consumption and emissions per aircraft category.

	Fuel $[Tg]$	CO_2 $[Tg]$	CO $[Gg]$	HC $[Gg]$	NO_x $[Tg]$	SO_x $[Gg]$	H_2O $[Tg]$	BC $[Gg]$
Regional	15.8	49.6	88.7	5.8	0.3	12.6	19.5	0.8
Short	79.9	251.5	290.3	17.7	1.4	63.9	98.7	2.8
Medium	53.3	168.0	131.7	9.6	0.9	42.6	65.9	1.3
Long	57.3	180.6	69.4	6.6	1.2	45.8	70.8	0.9
Very long	65.8	207.6	53.9	5.3	1.5	52.7	81.4	1.0
Total	272.0	857.1	634.2	45.6	5.3	217.6	336.3	6.8

during the LTO cycle. Even though the fuel consumption might not be very high compared to the total, the emissions of some species are very significant due to the relatively large number of LTO cycles of these aircraft compared to longer haul aircraft.
Another very interesting fact is the emission of nitrogen oxides of very long haul aircraft compared to short haul aircraft. Even though very long haul flights consume less fuel globally compared to short haul flights, the emission of nitrogen oxides is higher. This is directly caused by the relatively high emission index at cruise altitude.

A comparison to research by EASA and the EEA [76] is made for carbon dioxide and nitrogen oxide share of emissions. Note that this research distinguishes between five different kinds of flight lengths (and that their definition is marginally different), while EASA and the EEA distinguish four kinds of flight lengths. This comparison is made in Figure 7.17 with data from this research and Figure 7.18 with data from EASA and the EEA.

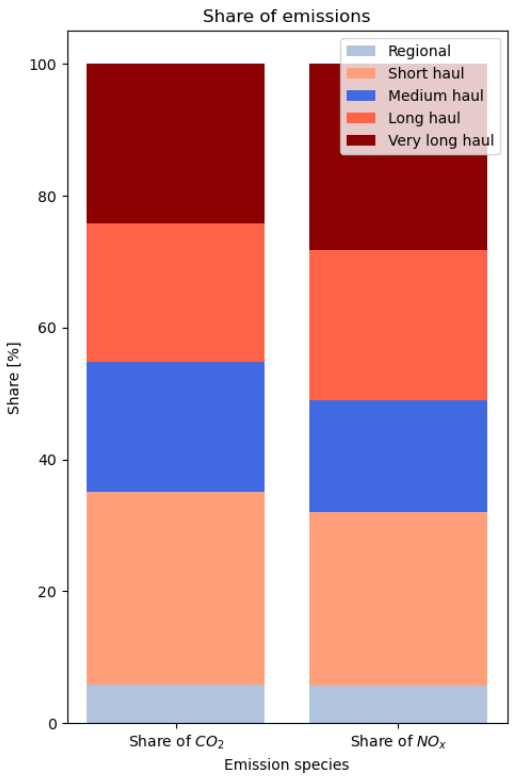

Figure 7.17: Stacked bar chart of carbon dioxide emission and nitrogen oxide emission per flight category.

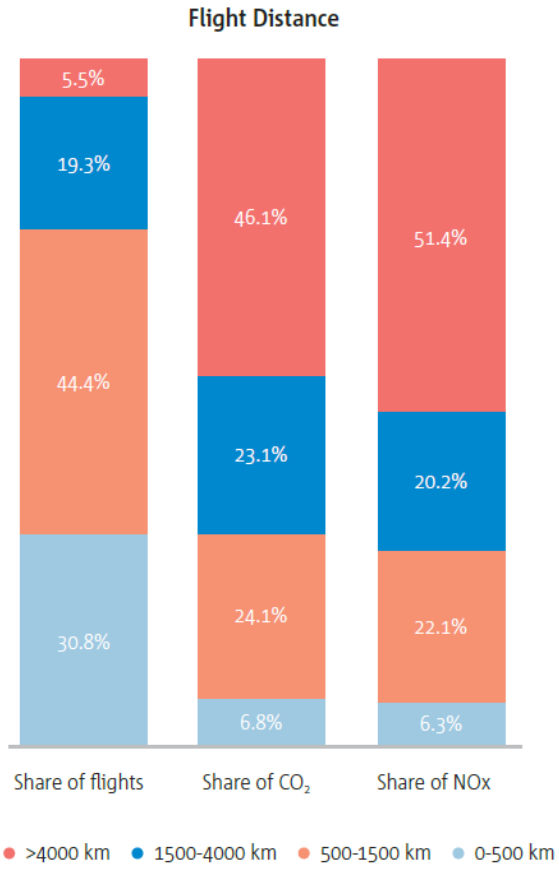

Figure 7.18: Fuel consumption and nitrogen oxide emission per aircraft category according to the EEA/EASA (figure obtained from EASA [76]).

Please note the different aircraft categories based on flight distance. The definitions used

in this research and in the EASA/EEA research are very similar with the exception that this research distinguishes long haul and very long haul flights while these are the same category in the EASA/EEA research. Both figures are almost the same and the observed differences are expected to be caused by the marginal different boundaries on flight distance. The nitrogen oxide emission can also be compared to the values from Table 7.3 where the percentual values are almost identical to Figure 7.18.

7.5. Comparison

As mentioned in Chapter 6 the total emissions and fuel consumption require verification and validation. No emission inventories have been created for 2019 yet and therefore a variety of research is considered including predictions for the future based on those inventories. Unfortunately, no emission inventories have been found where the emission of black carbon is estimated and therefore the verification and validation of the complete results is limited to all species except black carbon. This comparison is presented in Table 7.4 also with the quantity of fuel sold based on results of the *U.S. Energy Information Administration*[1] (EIA) (assuming $159\ l/barrel$ and kerosene density of $780\ kg/m^3$). Lastly, all the other researches state that NO_x is regarded as NO_2 and SO_x is regarded as SO_2 and n/a means no available data.

In general the results are close to research which has already been conducted. For the fuel consumption, the estimation in this research is relatively close to the validation fuel sold according to the EIA. The difference is attributed to several factors: smaller aviation is not included in this research (such as turboprop aircraft), the fuel policy of airlines is not included in the uncertainty analysis and hence elements like fuel tankering are not corrected for. The result, however, is consistent with the increase in fuel consumption as seen from the years previous 2019.

The differences in carbon dioxide can directly be attributed to the difference in fuel consumption due to the low influence of carbon monoxide emission index.

The emission of carbon monoxide seems relatively low at first. However, when compared to results from 2005 and 2008, respectively $203\ Tg$ of fuel and $0.55\ Tg$ of carbon monoxide and $229\ Tg$ of fuel and $0.69\ Tg$ of carbon monoxide, the difference is relatively small normalizing for the fuel consumption. Using the fleet wide emission index of carbon monoxide of 2005 would yield a carbon monoxide emission of $0.74\ Tg$ in 2019 and for the fleet wide emission index of carbon monoxide in 2008 this would mean a carbon monoxide emission of $0.82\ Tg$. The carbon monoxide emission in this research is, however, still lower compared to other research.

The emission of hydrocarbon found in this research is relatively high thus showing a relatively low combustion efficiency on a fleet wide basis. Comparing the results with data from 2005, 2006 and 2007 with emissions of $0.28\ Tg$, $0.24\ Tg$ and $0.23\ Tg$ of unburned hydrocarbons and normalizing with respect to the fuel consumption, the result is quite good. However, one would expect considerable progress on combustion efficiency on a fleet wide scale.

The estimation of emission of nitrogen oxides is considered good using the historical trend. Especially based on relatively new results from 2010 and 2011, again normalizing with respect to the fuel consumption, the match is almost identical. However, for next generation combustors new methods should be developed to account for these new technologies. This is especially true for lean burn engines such as the GEnx engines used on the Boeing 787 and the Boeing 737 Max.

The emission of sulfur oxides and water vapor is modelled well. This is also logical as the emission indices for these two species are widely used by researchers. Furthermore, the sulfur content in kerosene has not changed significantly in recent years according to the IPCC [86] which is also clear from the results.

[1] `https://www.eia.gov/` (accessed 21-10-2022)

Table 7.4: Comparison to previous emission inventories.

Year	Fuel [Tg]	CO_2 [Tg]	CO [Tg]	HC [Tg]	NO_x [Tg]	SO_x [Tg]	H_2O [Tg]	Research
1990	92.8	293.0	0.53	0.14	1.2	0.074	115.0	[77]
1992	110.0	347.0	n/a	n/a	n/a	0.13	135.0	[78]
1992	94.9	423.0	0.50	0.195	1.2	n/a	165.0	[8]
1999	128.0	n/a	0.69	0.19	1.7	n/a	n/a	[79]
1999	136.0	430.0	0.67	0.23	1.4	0.16	167.0	[78]
2000	181.0	572.0	0.54	0.08	2.5	0.15	224.0	[80]
2000	214.0	677.0	n/a	n/a	2.9	n/a	n/a	[12]
2000	152.0	480.0	n/a	n/a	2.0	0.18	187.0	[78]
2001	170.0	536.0	0.46	0.06	2.4	0.14	210.0	[80]
2002	171.0	539.0	0.48	0.06	2.4	0.14	211.0	[80]
2002	156.0	492.0	0.51	0.06	2.1	n/a	193.0	[7]
2002	154.0	486.0	n/a	n/a	n/a	0.18	190.0	[78]
2003	176.0	557.0	0.49	0.06	2.5	0.14	218.0	[80]
2004	188.0	595.0	0.51	0.06	2.7	0.15	233.0	[80]
2004	174.1	549.7	0.63	0.09	2.5	0.20	215.3	[81]
2005	203.0	641.0	0.55	0.07	2.9	0.16	251.0	[82]
2005	180.6	570.5	0.75	0.2	2.7	0.22	n/a	[23]
2005	147.6	464.7	0.78	0.28	3.4	0.12	181.5	[10]
2006	188.2	594.3	0.68	0.10	2.7	0.22	232.8	[78], [81]
2006	152.2	479.3	0.74	0.24	3.5	0.13	187.2	[10]
2007	160.9	506.8	0.75	0.23	3.7	0.14	198.0	[10]
2008	229.0	725.0	0.69	0.09	3.2	0.18	282.0	[83]
2008	163.0	513.4	0.74	0.21	3.8	0.14	200.5	[10]
2009	158.1	498.0	0.69	0.18	3.7	0.13	194.5	[10]
2010	240.0	n/a	1.92	0.3	3.02	n/a	n/a	[84]
2010	163.9	516.0	0.69	0.17	3.9	0.14	201.5	[10]
2011	173.2	545.3	0.70	0.16	4.1	0.15	213.0	[10]
2015	255.0	803.0	1.14	0.10	2.3	0.10	315.0	[77]
2015	282.0	n/a	1.44	0.23	3.9	n/a	n/a	[85]
2019	**272.0**	**857.1**	**0.63**	**0.45**	**5.3**	**0.22**	**336.3**	**This study**
2019	322.3	n/a	n/a	n/a	n/a	n/a	n/a	U.S. EIA
2020	336.0	n/a	1.39	0.23	4.9	n/a	n/a	[85]
2025	327.0	1029.0	1.15	0.15	3.3	n/a	404.0	[7]
2030	440.0	n/a	2.33	0.29	4.95	n/a	n/a	[84]
2050	770.0	n/a	2.64	0.25	7.5	n/a	n/a	[84]

8

Conclusions & Discussion

The main accomplishments and conclusions drawn from this thesis are:

- Emission inventories contain many assumptions which change significantly over time due to new routing possibilities and changes in demand. It is therefore essential to keep these assumptions updated by collaborating with airlines.
- The uncertainties used in previous emission inventories are very large and have mainly been taken from relatively old research. New research should be performed, in addition to the uncertainty analysis from this report, which cover all aspects of the uncertainty analysis.
- Modelling of engine performance is a difficult process largely dependent on the available information. The BFFM2 is still valid for the current world fleet even using new combustion technology.
- Predictions on global kerosene consumption based on the expected increase in traffic and the increase in (global) fleet efficiency have yielded results which are in line with conclusions drawn in this report.

8.1. Conclusions

The objective of this research was to create an updated emission inventory for climate assessment of aviation using new or updated methods to model aircraft and engine performance. This objective was successfully executed by means of answering the main research questions and its respective sub-questions. These are formulated again and answered underneath.

- What research can be used off the shelf and be complemented by this research in order to increase reliability of the data?

No previous research has been used off the shelf but this research has been strongly influenced by research that has been performed previously. Increasing the reliability of data mainly means decreasing the uncertainty associated with that same data. The most comprehensive uncertainty analysis associated with emission inventories has been conducted by Lee et al. [14] in 2005. This research by Lee et al., although of great importance, was conducted in a time where the uncertainty on individual aircraft operating parameters was relatively large. This means that the overall uncertainty on the outcome of an emission inventory is also significant, hence reducing the confidence in the results. This report and research, however, have been strongly influenced by the work of N.W. Simone [4], mainly concerning the performance model and the emission model. In addition, the airport database was taken off-the-shelf from this research.

- How can the uncertainty analysis be improved and the confidence in the results be increased?

This research has been aimed at reducing the uncertainty on the analysis of a large number of flights. This has been conducted in a bottom up approach, meaning that flight patterns were analyzed rather than fuel sales. The applied methodology is not completely new, nevertheless the uncertainty on individual parameters has been quantified and based on these uncertainties, the overall confidence in the results is established. Since the uncertainty on an individual parameter

basis is lower, the overall confidence in the results is increased. In addition, Lee et al. [14] only provides the uncertainty on fuel consumption while the uncertainty analysis in this research covers all elements of an emission inventory, hence including all the emission species too. This provides a significant advantage for policy makers and other researchers as they are provided with more accurate results taking into account uncertainty of emission index estimation methodologies.

- Taking into account the updated emission inventory model, what are the emissions of aviation?

The result of an emission inventory seems relatively simple, although the comprehensiveness of the data establishes its importance. The outcome of this emission inventory is a three dimensional grid which includes all major emission species, the quantity of emission and their geographical location. This provides other researchers with a starting point for climate impact assessment. As the altitude and geographical location are included, the climate impact assessment can be modelled more accurately compared to a situation where only the total emission is known. In addition, these three dimensional grids are also obtained for five categories of aircraft, categorized according to the flown distances. This also allows researchers to accurately model climate impact assessment of engine improvements limited to certain aircraft categories. The example could be including certain technological improvements to regional aircraft, such as electrifying this fleet or using sustainable aviation fuel (SAF) for very long haul aircraft. Summarized, the total emission of all major emission species is provided in Table 8.1 including the 90% confidence interval. Note that this is a simple copy of Table 7.2.

Table 8.1: Quantity of fuel consumption and emissions with 90% confidence.

Species	Nominal	Lower boundary	Upper boundary
Fuel [Tg]	272.0	269.4	274.9
CO_2 *[Tg]*	857.1	848.9	866.1
CO *[Gg]*	634.2	629.2	638.5
HC *[Gg]*	45.6	44.9	46.3
NO_x *[Tg]*	5.3	5.2	5.4
SO_x *[Gg]*	217.6	215.5	219.9
H_2O *[Tg]*	336.3	332.7	339.9
BC *[Gg]*	6.8	6.7	6.9

8.2. Discussion

Logically, this research allows for some significant improvements to be made. Similarly to the rest of this research and its methodology, the points of improvement are provided per discussed model as used in this research.

8.2.1. Information model

The information model is the starting point of the emission inventory, and associated with it are some improvements that can be made.

Use of a representative week

As mentioned extensively in this report, one representative week is used to compute the fuel consumption and emissions for the entire year. This method has its drawbacks as it reduces the accuracy of the results. Logically fluctuations occur relating to supply/demand and the types of routes flown throughout the entire year. This decision is still considered justified due to limitations placed on computing power, however as a recommendation it is advised to use multiple representative weeks throughout the year to account for demand variations and routing variations.

Complementing of *flightradar24* database

Ideally, one does not need to complement the provided database. In this research, a thorough analysis of the database of flights in the representative week was performed and limitations concerning availability of data were found. Complementing of this data was performed mainly based

on flight numbers. It is strongly advised to perform the analysis again, using the same week with data from a different source to find whether significant differences are found.

The same departure and arrival airports
Based on a visual analysis it was found that certain flights had the same departure and arrival airport. This concerned mainly general aviation flights. It was decided to delete those flights as no estimation could be made on the covered flight distance. *Flightradar24*, however, also provides the take-off time and landing time (many gaps in the database also occur for this information). One could argue that this information provides some degree of knowledge on the covered distance and a rough estimation on the covered distance could be made based on the airborne time.

Airport database
The airport database used in this research has been duplicated from the MIT Aviation Emission Inventory Code [23] which was developed in 2013. Although some very limited research has been conducted to find major airport developments opening in the 2013-2019 time frame, none have been found. It is, nevertheless, possible that a major airport is missing from the database which could have an impact on the outcome of the emission inventory.

Military flights
The *flightradar24* barely contains any military flights (in january 2019 only ten General Dynamics F-16 flights were found). This severely limits the computation of military fuel consumption and emissions. It is therefore recommended for future emission inventories to make an estimation on military fuel consumption and emissions based on historical trends. However, it will remain very difficult to estimate the location and altitude of the fuel consumption and emissions. As mentioned in Chapter 2 the quantity of fuel consumption and emission might not be negligible.

8.2.2. Performance model
The performance model uses data from the information model to compute the point performance and fuel consumption at various points of the trajectory.

Jet aircraft
This emission inventory is mainly limited to civil commercial aviation, which, in turn, mostly utilize jet aircraft. For this reason, the methodology is based around jet aircraft. This means that all piston and turboprop flights are discarded. Although these flights surely do not make up a majority of flights they could have some minor impact and explain the difference in fuel consumption found in this research and the quantity of fuel sold according to the U.S. EIA.

ICAO engine models
As became clear from Chapter 6 some problems were found relating to engine models provided in BADA and in the ICAO database. Sometimes a wrong engine model was selected in the ICAO database due to some engine models occuring more than once. Although this was checked for the discussed aircraft in Chapter 6, this has not been checked for all aircraft provided in BADA. This could mean that for some flights/aircraft types, the wrong engine is selected from the ICAO database.

Additionally, aircraft manufacturers often provide an aircraft with various options for engines of different manufacturers. These engines are comparable in performance but do have different fuel consumption and emission characteristics. It is recommended, in future research, to use the registration to find the exact engine model from an aircraft database. It is expected that the differences are very minor but the confidence in the results will be increased.

Fuel policy
Some uncertainty is also introduced by political/board influences. A clear example of this is the fuel policy of airlines. Some airlines use the concept of fuel tankering [87] to tank fuel for the return trip already at the point of departure. As this departure point is often their hub significant discounts can be negotiated if large quantities of fuel are to be supplied. This, however, does increase the fuel burn due to the increase in aircraft weight. This is, hence, an economical opportunity at the expense of increased climate impact.

Influence of weather
No weather information was used in the analysis of this emission inventory. Particularly wind is of significant interest as this increases the flight time (if head wind is encountered). Wind always has a negative effect on a round trip as the disadvantages of head wind are encountered for a longer time than the benefits of tail wind. It is therefore recommended to use the uncertainty associated to this in the uncertainty analysis.

8.2.3. Emission model
The last step to obtain the emissions is to apply the emission model to the results of the performance model.

Interpolation methods
As discussed in Chapter 4 different interpolation methods provide different emission index results. It was concluded that for one instance of comparison to a p3-T3 method, other interpolation methods than described by the BFFM2 provided a more representative result. It is therefore recommended to conduct research to improve the BFFM2 by changing the interpolation method.

Lean burn engines
The BFFM2 places a limitation on the combustion technology and states that lean burn engines, such as the GEnx engine family, are not suitable to be modelled by the BFFM2. This research has compared the BFFM2 to p3-T3 methods to show the differences for one specific instance. It is strongly recommended to use a different method for lean burn combustion engine modelling or adapt the BFFM2 for these engines. This is especially important in future works as many 'regular' aircraft will be phased out in coming years and replaced by Boeing 787s or Boeing 737 MAXs which utilize this combustion technology. It is therefore expected that the influence of the decision to model these engines using the BFFM2 in this research is very limited but it could become significant when this subfleet increases.

DLR/FOA method
The DLR/FOA method has been specially developed to work in a similar way compared to the BFFM2: use non-proprietary engine information to model black carbon emission. The conducted research is from 2001 and black carbon emission is one of the focus points of engine manufacturers. Logically this affects the datapoints in the ICAO database, but this could also affect the emission at cruise altitude. It is therefore recommended to compare the method to other proprietary methods for various flight instances to make a direct comparison and find how suitable this model is for current generation engine black carbon emission modelling.

8.2.4. Uncertainty analysis
A significant element in this report is the uncertainty analysis. Some improvements can also be made relating to this element.

DLR/FOA method uncertainty
No information has been found relating to the uncertainties attributed to use of the DLR/FOA method. It is therefore recommended to compare this method to proprietary engine methods to find the uncertainty related to this emission index estimation method.

Cruise altitude uncertainty
For the purpose of this emission inventory it has been decided not to include the uncertainty associated with cruise altitude. The underlying reason was that it is very difficult to quantify this uncertainty and no pluralistic information was available to compute this uncertainty. It is therefore strongly recommended to use data from a variety of airlines to quantify the uncertainty related to cruise altitude. In addition, one could also conduct a variety of simulations to find the minimum fuel consumption for various trajectories. Logically, this is the preferable case for airlines as well.

Sulfur oxide emission index uncertainty
The uncertainty associated to the emission index of sulfur oxides is very large and it was therefore decided to use the fuel consumption uncertainties to account for the variations in sulfur oxide emission. To account for this individual uncertainty it is recommended to compare fuel samples from distributors around the world to validate the sulfur content. Large scientific consensus exists around the constant sulfur emission index but the uncertainty associated to this is not unanimous.

Compressor efficiency and black carbon emission index
The degradation of engine components taken into account for the engine aging thrust specific fuel consumption increase is limited to only this part of the uncertainty analysis. The black carbon emission index calculation also utilizes the component efficiency of the compressor. It is recommended to find the probability density function associated with black carbon emission index due to compressor degradation using the probability density function of component degradation as prescribed in Chapter 5.

A

Convergence engine aging simulation

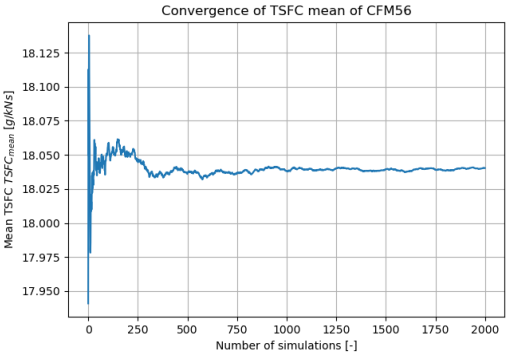

Figure A.1: Convergence of the mean $TSFC$ for the CFM56 engine.

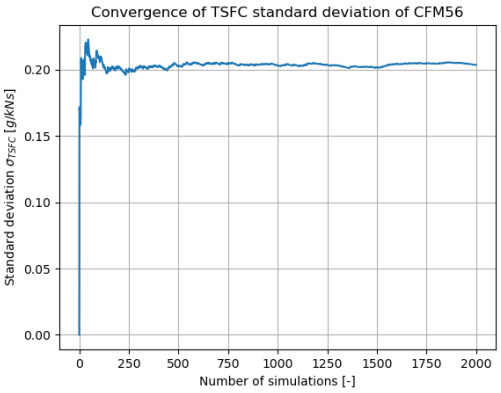

Figure A.2: Convergence of the standard deviation of $TSFC$ for the CFM56 engine.

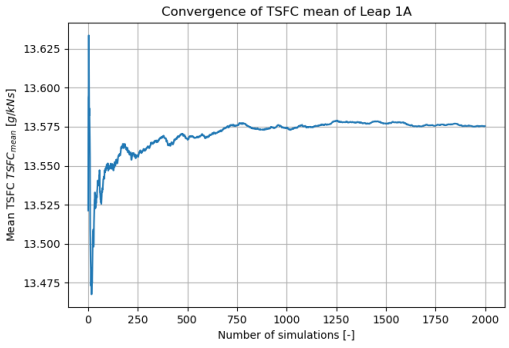

Figure A.3: Convergence of the mean $TSFC$ for the Leap 1A engine.

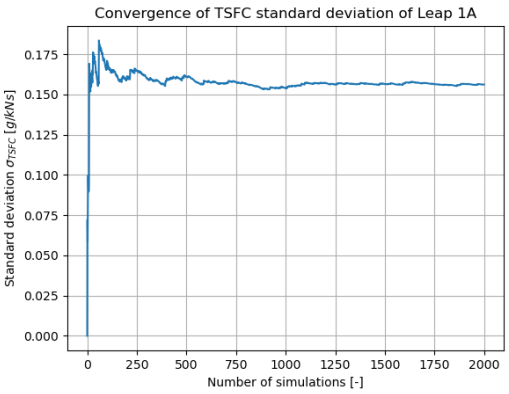

Figure A.4: Convergence of the standard deviation of $TSFC$ for the Leap 1A engine.

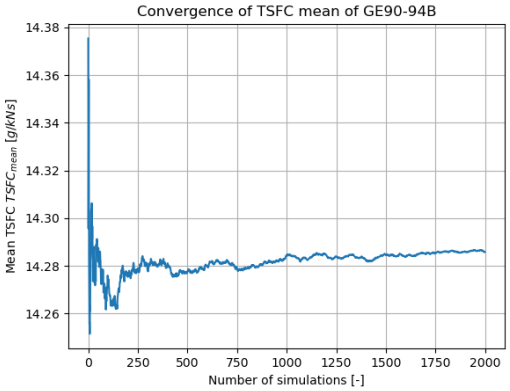

Figure A.5: Convergence of the mean $TSFC$ for the GE90-94B engine.

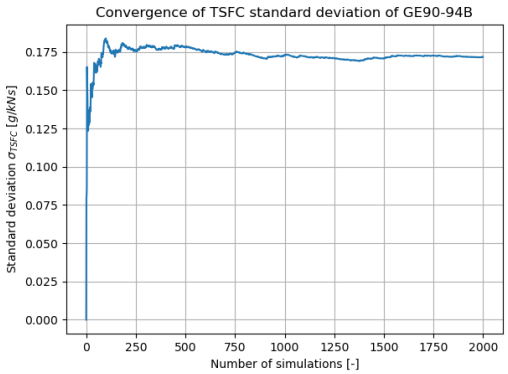

Figure A.6: Convergence of the standard deviation of $TSFC$ for the GE90-94B engine.

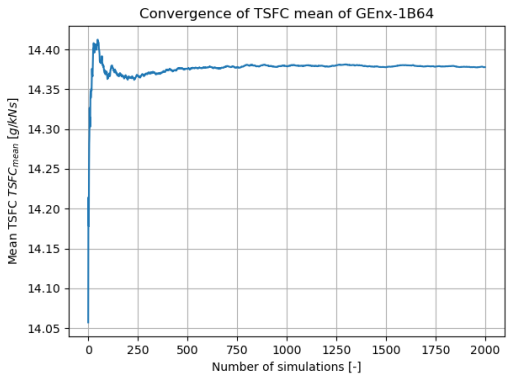

Figure A.7: Convergence of the mean $TSFC$ for the GEnx-1B64 engine.

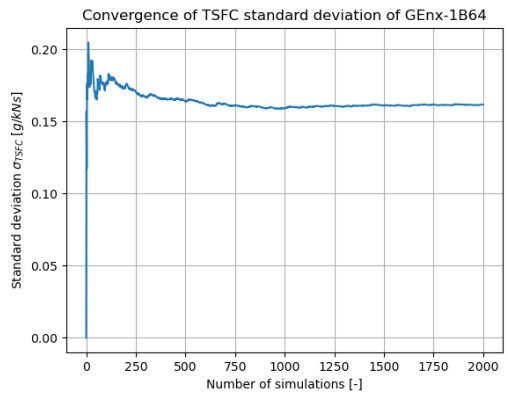

Figure A.8: Convergence of the standard deviation of $TSFC$ for the GEnx-1B64 engine.

B

BADA fuel flow uncertainty

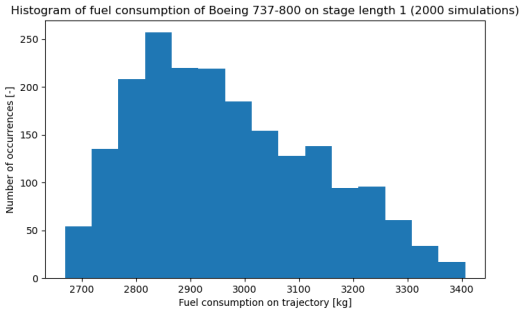

Figure B.1: Uncertainty in fuel consumption for stage length 1 Boeing 737-800.

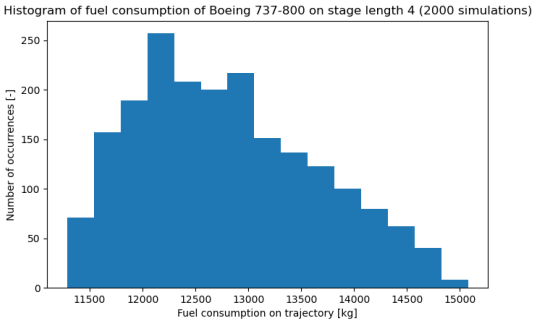

Figure B.2: Uncertainty in fuel consumption for stage length 4 Boeing 737-800.

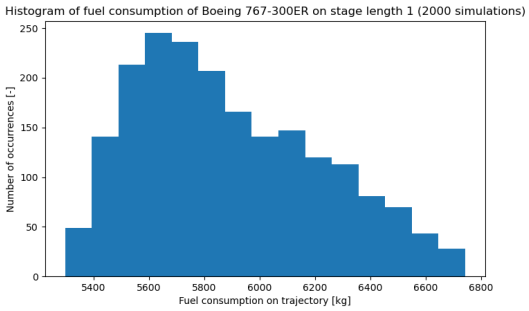

Figure B.3: Uncertainty in fuel consumption for stage length 1 Boeing 767-300ER.

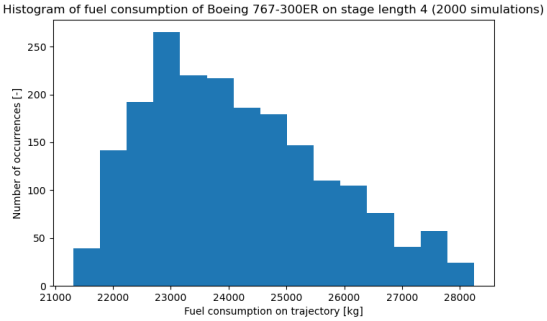

Figure B.4: Uncertainty in fuel consumption for stage length 4 Boeing 767-300ER.

C

Convergence total fleet

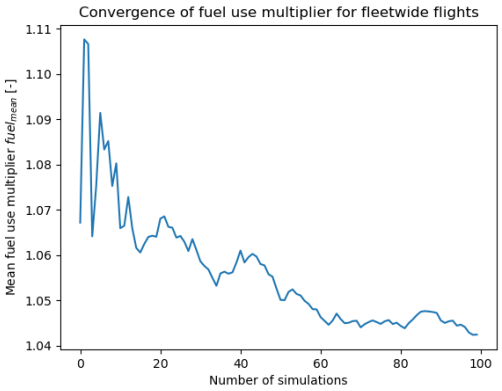

Figure C.1: Convergence of the mean fuel consumption multiplier until every simulation.

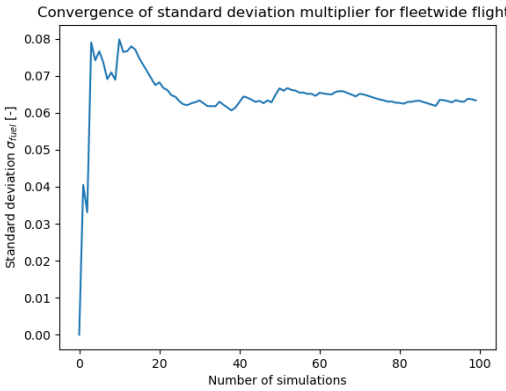

Figure C.2: Convergence of the fuel consumption standard deviation until every simulation.

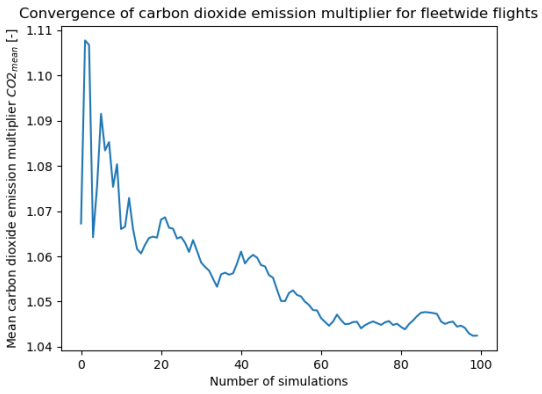

Figure C.3: Convergence of the mean carbon dioxide emission multiplier until every simulation.

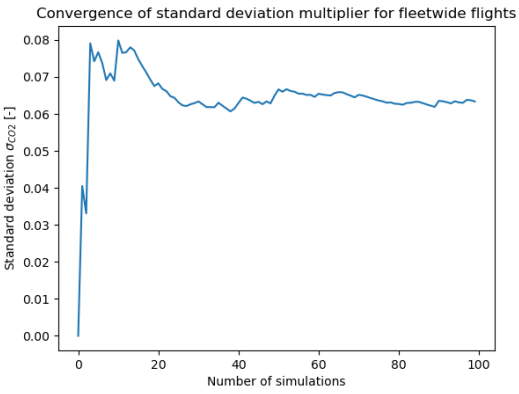

Figure C.4: Convergence of the carbon dioxide emission standard deviation until every simulation.

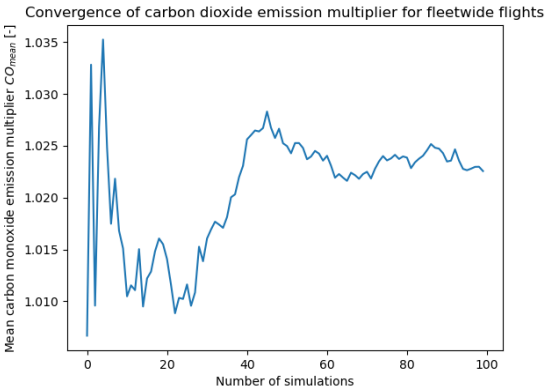

Figure C.5: Convergence of the mean carbon monoxide emission multiplier until every simulation.

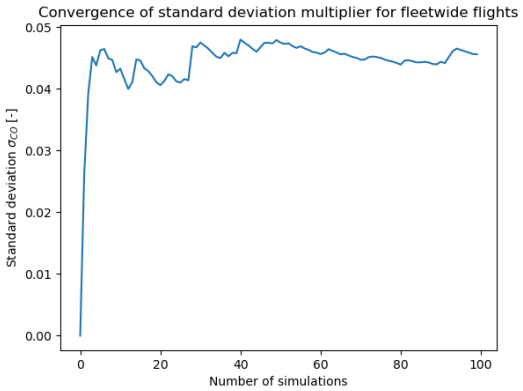

Figure C.6: Convergence of the carbon monoxide emission standard deviation until every simulation.

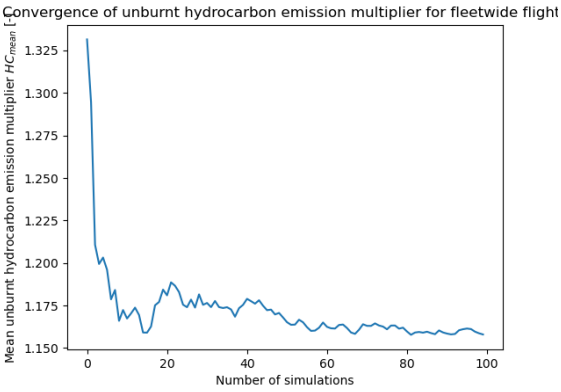

Figure C.7: Convergence of the mean unburned hydrocarbon emission multiplier until every simulation.

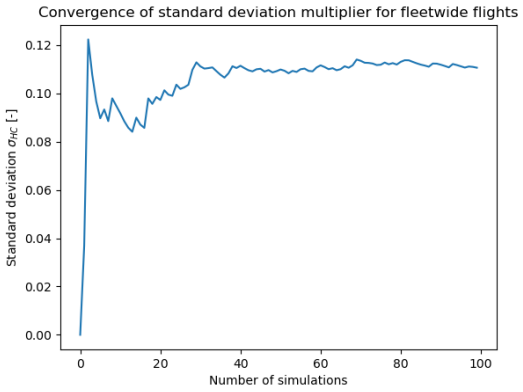

Figure C.8: Convergence of the unburned hydrocarbon emission standard deviation until every simulation.

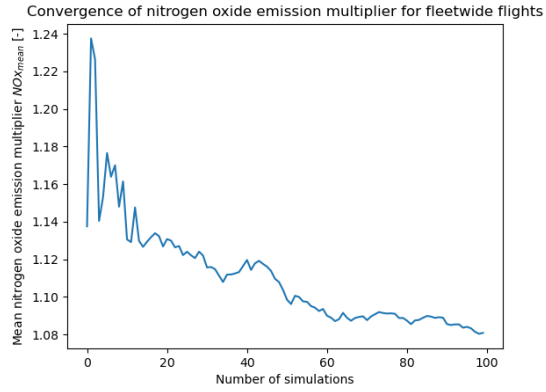

Figure C.9: Convergence of the mean nitrogen oxide emission multiplier until every simulation.

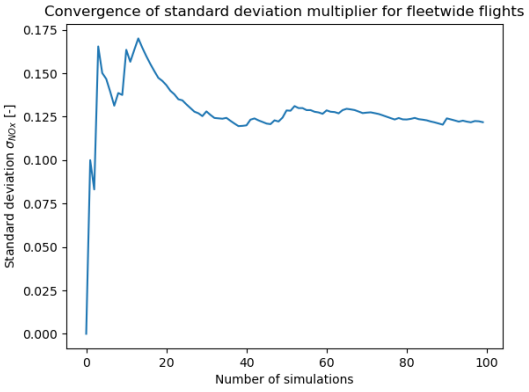

Figure C.10: Convergence of the nitrogen oxide emission standard deviation until every simulation.

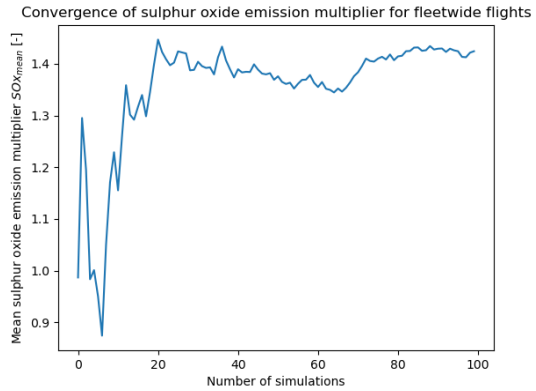

Figure C.11: Convergence of the mean sulfur oxide emission multiplier until every simulation.

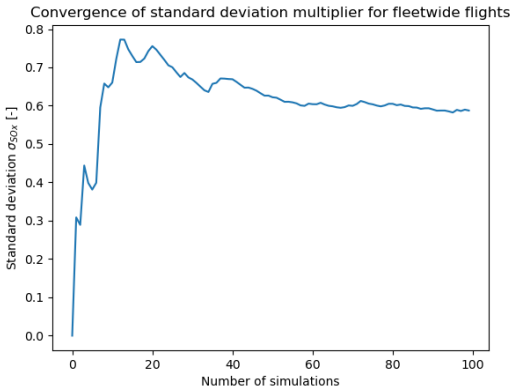

Figure C.12: Convergence of the sulfur oxide emission standard deviation until every simulation.

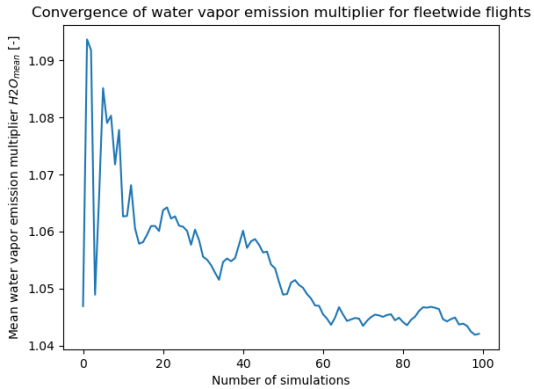

Figure C.13: Convergence of the mean water vapor emission multiplier until every simulation.

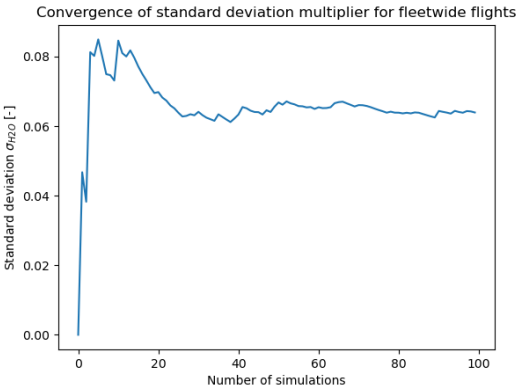

Figure C.14: Convergence of the water vapor emission standard deviation until every simulation.

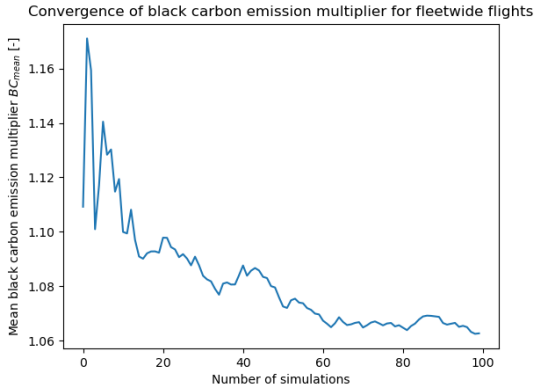

Figure C.15: Convergence of the mean black carbon emission multiplier until every simulation.

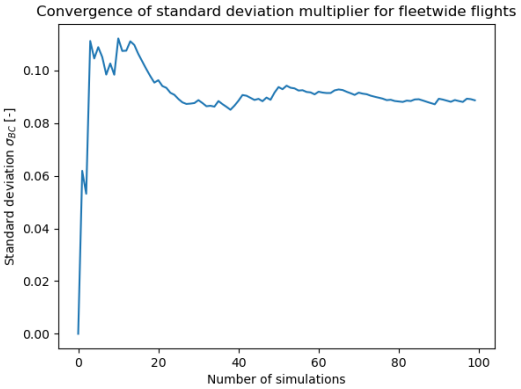

Figure C.16: Convergence of the black carbon emission standard deviation until every simulation.

D

Uncertainty short haul

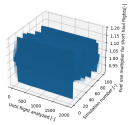

Figure D.1: Convergence of mean fuel multiplier for all 2000 flights in all 100 simulations.

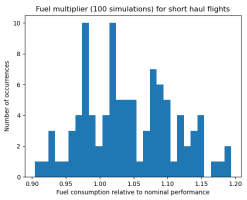

Figure D.2: Histogram representing the fuel consumption multipliers of the 100 simulations.

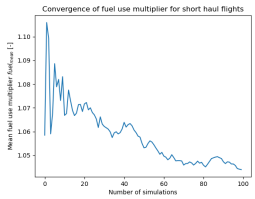

Figure D.3: Convergence of the mean fuel consumption multiplier until every simulation.

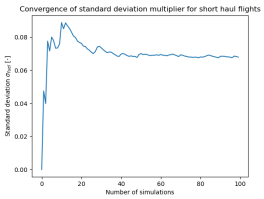

Figure D.4: Convergence of the fuel consumption standard deviation until every simulation.

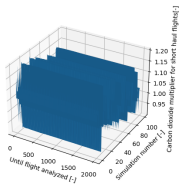

Figure D.5: Histogram representing the carbon dioxide emission multipliers of the 100 simulations.

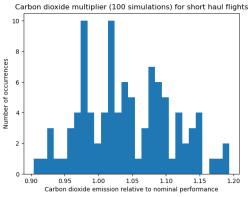

Figure D.6: Histogram representing the carbon dioxide emission multipliers of the 100 simulations.

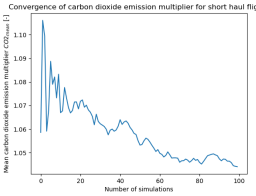

Figure D.7: Convergence of the mean carbon dioxide emission multiplier until every simulation.

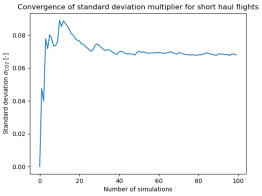

Figure D.8: Convergence of the carbon dioxide emission standard deviation until every simulation.

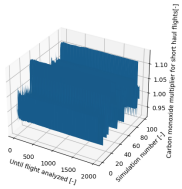

Figure D.9: Histogram representing the carbon monoxide emission multipliers of the 100 simulations.

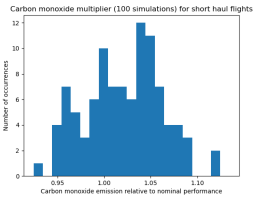

Figure D.10: Histogram representing the carbon monoxide emission multipliers of the 100 simulations.

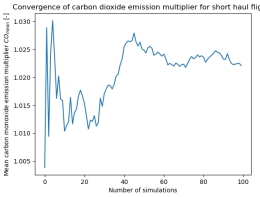

Figure D.11: Convergence of the mean carbon monoxide emission multiplier until every simulation.

Figure D.12: Convergence of the carbon monoxide emission standard deviation until every simulation.

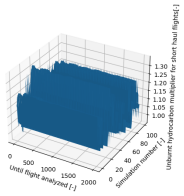

Figure D.13: Histogram representing the unburned hydrocarbon emission multipliers of the 100 simulations.

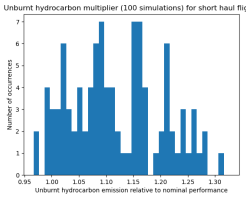

Figure D.14: Histogram representing the unburned hydrocarbon emission multipliers of the 100 simulations.

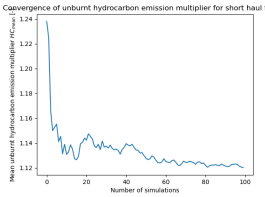

Figure D.15: Convergence of the mean unburned hydrocarbon emission multiplier until every simulation.

Figure D.16: Convergence of the unburned hydrocarbon emission standard deviation until every simulation.

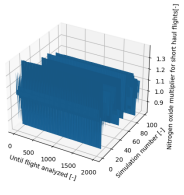

Figure D.17: Histogram representing the nitrogen oxide emission multipliers of the 100 simulations.

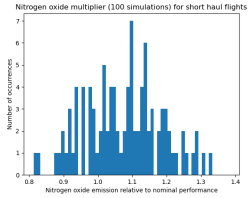

Figure D.18: Histogram representing the nitrogen oxide emission multipliers of the 100 simulations.

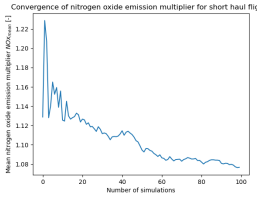

Figure D.19: Convergence of the mean nitrogen oxide emission multiplier until every simulation.

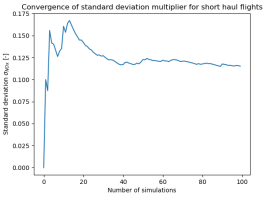

Figure D.20: Convergence of the nitrogen oxide emission standard deviation until every simulation.

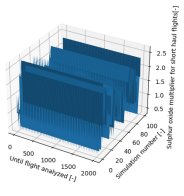

Figure D.21: Histogram representing the sulfur oxide emission multipliers of the 100 simulations.

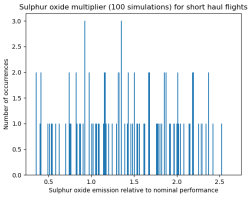

Figure D.22: Histogram representing the sulfur oxide emission multipliers of the 100 simulations.

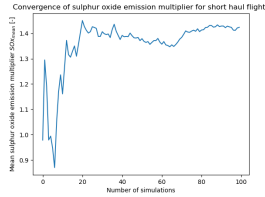

Figure D.23: Convergence of the mean sulfur oxide emission multiplier until every simulation.

Figure D.24: Convergence of the sulfur oxide emission standard deviation until every simulation.

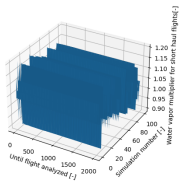

Figure D.25: Histogram representing the water vapor emission multipliers of the 100 simulations.

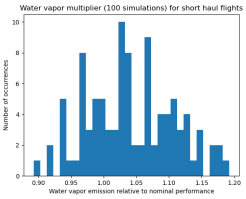

Figure D.26: Histogram representing the water vapor emission multipliers of the 100 simulations.

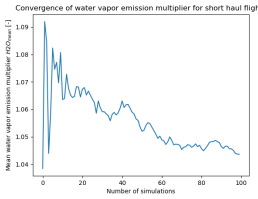

Figure D.27: Convergence of the mean water vapor emission multiplier until every simulation.

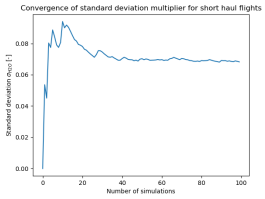

Figure D.28: Convergence of the water vapor emission standard deviation until every simulation.

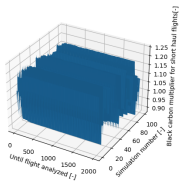

Figure D.29: Histogram representing the black carbon emission multipliers of the 100 simulations.

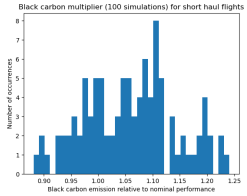

Figure D.30: Histogram representing the black carbon emission multipliers of the 100 simulations.

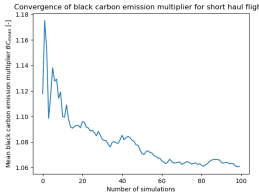

Figure D.31: Convergence of the mean black carbon emission multiplier until every simulation.

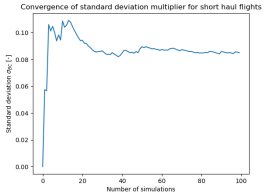

Figure D.32: Convergence of the black carbon emission standard deviation until every simulation.

Table D.1: Mean multiplier and confidence intervals of short haul flights.

Species	Mean	50% CI	90% CI	95% CI	99% CI
Fuel consumption	1.044	[1.039; 1.049]	[1.033; 1.055]	[1.030; 1.058]	[1.026; 1.062]
CO_2 *emission*	1.044	[1.039; 1.049]	[1.033; 1.055]	[1.030; 1.058]	[1.026; 1.062]
CO *emission*	1.022	[1.019; 1.025]	[1.015; 1.029]	[1.014; 1.030]	[1.011; 1.033]
HC *emission*	1.120	[1.114; 1.126]	[1.106; 1.135]	[1.103; 1.137]	[1.097; 1.143]
NO_x *emission*	1.077	[1.069; 1.085]	[1.057; 1.096]	[1.054; 1.100]	[1.046; 1.107]
SO_x *emission*	1.424	[1.384; 1.464]	[1.327; 1.521]	[1.308; 1.540]	[1.270; 1.578]
H_2O *emission*	1.044	[1.039; 1.048]	[1.032; 1.055]	[1.030; 1.057]	[1.026; 1.062]
BC *emission*	1.061	[1.055; 1.067]	[1.047; 1.075]	[1.044; 1.078]	[1.038; 1.083]

E

Uncertainty long haul

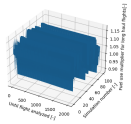

Figure E.1: Convergence of mean fuel multiplier for all 2000 flights in all 100 simulations.

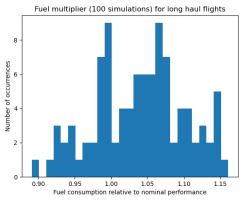

Figure E.2: Histogram representing the fuel consumption multipliers of the 100 simulations.

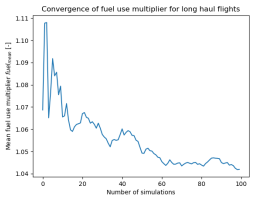

Figure E.3: Convergence of the mean fuel consumption multiplier until every simulation.

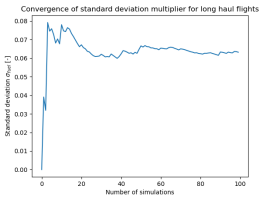

Figure E.4: Convergence of the fuel consumption standard deviation until every simulation.

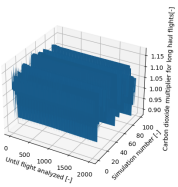

Figure E.5: Histogram representing the carbon dioxide emission multipliers of the 100 simulations.

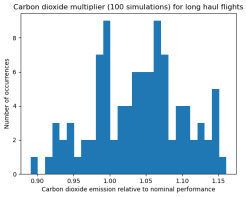

Figure E.6: Histogram representing the carbon dioxide emission multipliers of the 100 simulations.

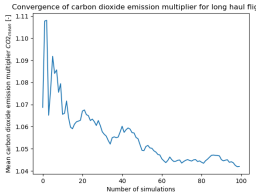

Figure E.7: Convergence of the mean carbon dioxide emission multiplier until every simulation.

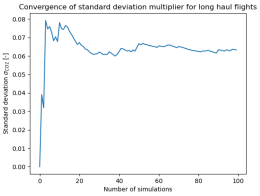

Figure E.8: Convergence of the carbon dioxide emission standard deviation until every simulation.

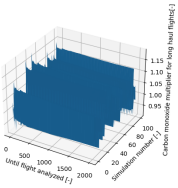

Figure E.9: Histogram representing the carbon monoxide emission multipliers of the 100 simulations.

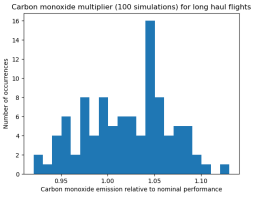

Figure E.10: Histogram representing the carbon monoxide emission multipliers of the 100 simulations.

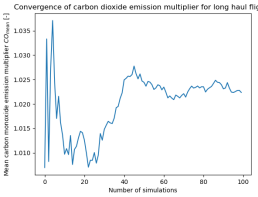

Figure E.11: Convergence of the mean carbon monoxide emission multiplier until every simulation.

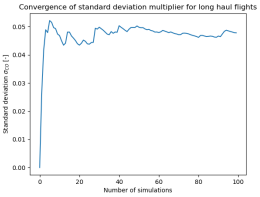

Figure E.12: Convergence of the carbon monoxide emission standard deviation until every simulation.

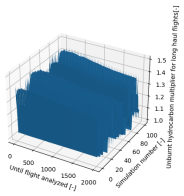

Figure E.13: Histogram representing the unburned hydrocarbon emission multipliers of the 100 simulations.

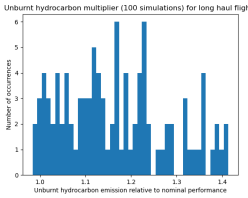

Figure E.14: Histogram representing the unburned hydrocarbon emission multipliers of the 100 simulations.

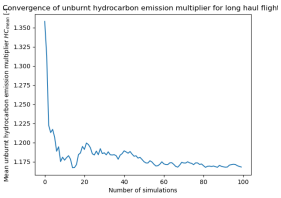

Figure E.15: Convergence of the mean unburned hydrocarbon emission multiplier until every simulation.

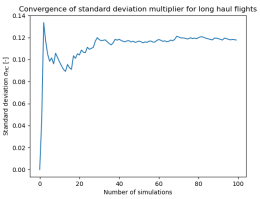

Figure E.16: Convergence of the unburned hydrocarbon emission standard deviation until every simulation.

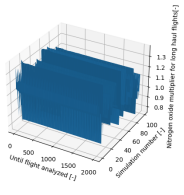

Figure E.17: Histogram representing the nitrogen oxide emission multipliers of the 100 simulations.

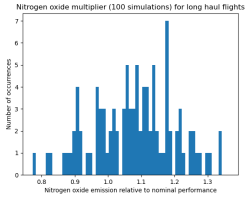

Figure E.18: Histogram representing the nitrogen oxide emission multipliers of the 100 simulations.

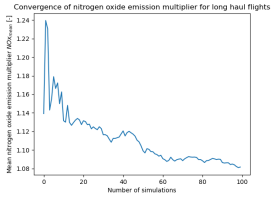

Figure E.19: Convergence of the mean nitrogen oxide emission multiplier until every simulation.

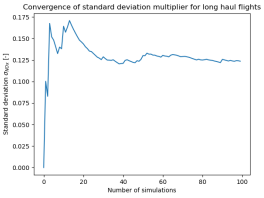

Figure E.20: Convergence of the nitrogen oxide emission standard deviation until every simulation.

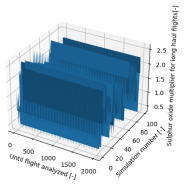

Figure E.21: Histogram representing the sulfur oxide emission multipliers of the 100 simulations.

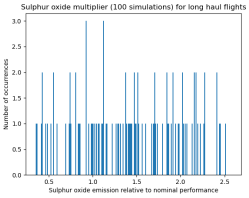

Figure E.22: Histogram representing the sulfur oxide emission multipliers of the 100 simulations.

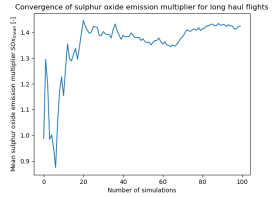

Figure E.23: Convergence of the mean sulfur oxide emission multiplier until every simulation.

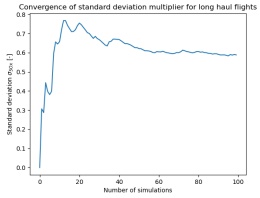

Figure E.24: Convergence of the sulfur oxide emission standard deviation until every simulation.

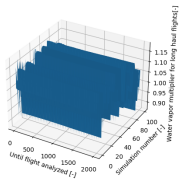

Figure E.25: Histogram representing the water vapor emission multipliers of the 100 simulations.

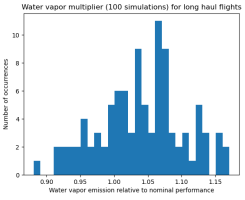

Figure E.26: Histogram representing the water vapor emission multipliers of the 100 simulations.

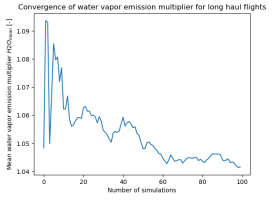

Figure E.27: Convergence of the mean water vapor emission multiplier until every simulation.

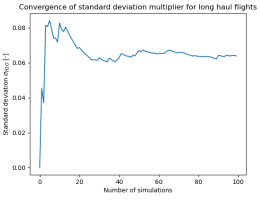

Figure E.28: Convergence of the water vapor emission standard deviation until every simulation.

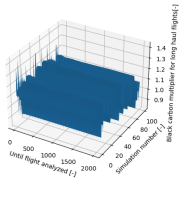

Figure E.29: Histogram representing the black carbon emission multipliers of the 100 simulations.

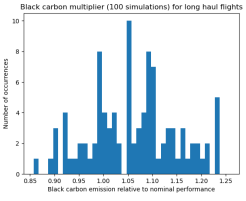

Figure E.30: Histogram representing the black carbon emission multipliers of the 100 simulations.

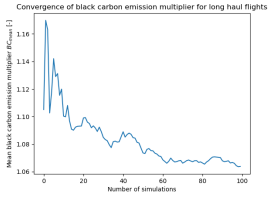

Figure E.31: Convergence of the mean black carbon emission multiplier until every simulation.

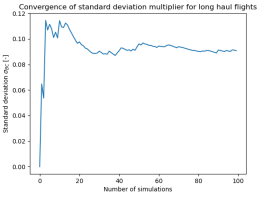

Figure E.32: Convergence of the black carbon emission standard deviation until every simulation.

Table E.1: Mean multiplier and confidence intervals of long haul flights.

Species	Mean	50% CI	90% CI	95% CI	99% CI
Fuel consumption	1.042	[1.038; 1.046]	[1.031; 1.053]	[1.029; 1.055]	[1.025; 1.059]
CO_2 *emission*	1.042	[1.038; 1.046]	[1.031; 1.053]	[1.029; 1.055]	[1.025; 1.059]
CO *emission*	1.022	[1.019; 1.026]	[1.014; 1.030]	[1.013; 1.032]	[1.010; 1.035]
HC *emission*	1.168	[1.160; 1.176]	[1.149; 1.188]	[1.145; 1.192]	[1.137; 1.199]
NO_x *emission*	1.082	[1.073; 1.090]	[1.061; 1.102]	[1.057; 1.106]	[1.049; 1.114]
SO_x *emission*	1.424	[1.384; 1.464]	[1.326; 1.523]	[1.307; 1.542]	[1.269; 1.580]
H_2O *emission*	1.042	[1.037; 1.046]	[1.031; 1.052]	[1.029; 1.054]	[1.025; 1.058]
BC *emission*	1.064	[1.058; 1.070]	[1.049; 1.079]	[1.046; 1.082]	[1.040; 1.088]

F

Payload-range diagrams

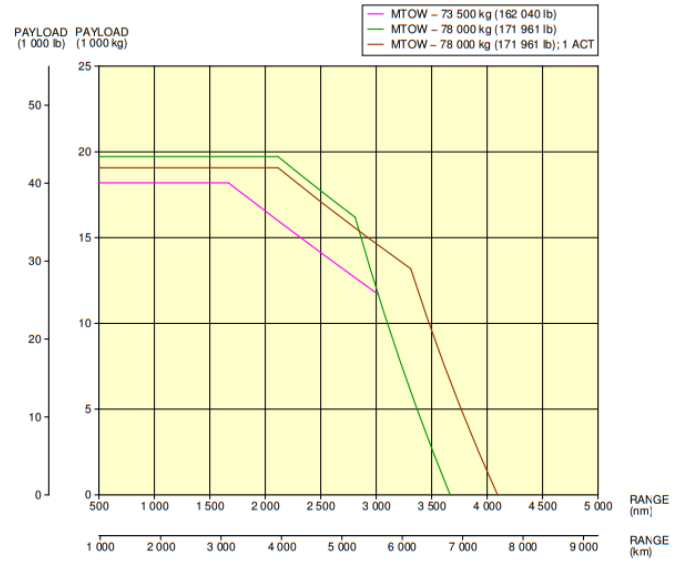

(a) Payload-range diagram of Airbus A320 from manual (figure obtained from *A320 Aircraft Characteristics Airport and Maintenance Planning* [88]).

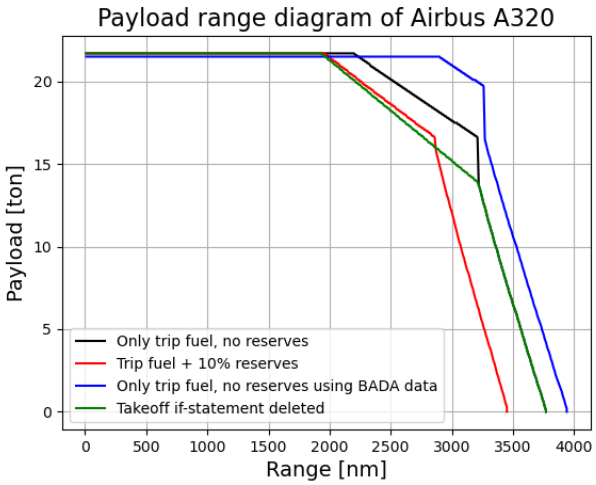

(b) Payload-range diagram of Airbus A320 obtained using *Python*.

Figure F.1: Payload range diagrams of the Airbus A320.

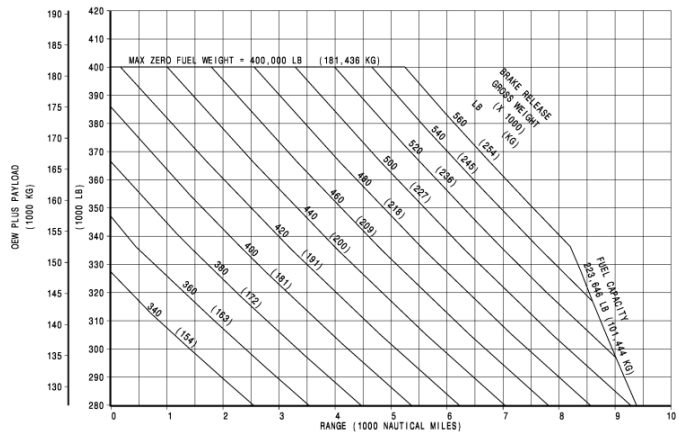

(a) Payload-range diagram of Boeing 787-9 from manual (figure obtained from *787 Airplane Characteristics for Airport Planning* [89]).

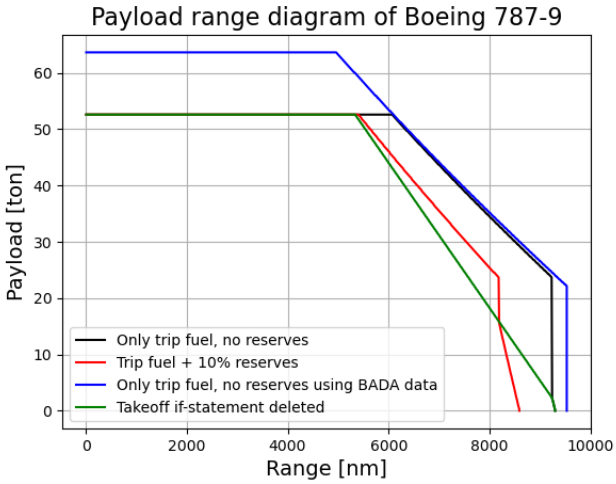

(b) Payload-range diagram of Boeing 787-9 obtained using *Python*.

Figure F.2: Payload range diagrams of the Boeing 787-9.

G

Non-available aircraft

Table G.1: List of aircraft/helicopters not used in the analysis.

0	AS32	BEAR	CH30	DHC1	G200	LA25	P32R	RS18	T34
146	AS50	BEH	CH60	DHC2	G21	LA4	P32T	RS20	T34P
320	AS55	BES	CH65	DHC3	G2CA	LAE1	P337	RV10	T34T
321	AS65	BET	CH7	DHC4	G2T1	LAKR	P3C	RV12	T6
330	ASTO	BK17	CH70	DHC6	G3	LARK	P46T	RV14	TAGO
333	AT3T	BKUT	CH75	DHC7	G44	LEG2	P51	RV3	TAIL
717	AT4	BL07	CH7A	DHT	G6	LEGD	P68	RV4	TAMP
732	AT42	BL17	CH7B	DIMO	G70	LESP	P750	RV6	TARR
734	AT43	BL8	CH80	DISC	G73	LGEZ	PA11	RV7	TAYD
735	AT44	BN2P	CJ6	DR10	G73T	LJ3	PA12	RV8	TB20
737	AT45	BN2T	CJL	DR22	GA7	LJ36	PA14	RV9	TB21
738	AT46	BOLT	CL2P	DR30	GA8	LNC2	PA16	S108	TB30
773	AT5T	BPAT	CL2T	DR40	GAZL	LNC4	PA17	S10S	TBM7
32S	AT6	BRAV	CLON	DRON	GC1	LNCE	PA18	S11	TBM8
73E	AT6T	BREZ	CN35	DUOD	GLAC	LNP4	PA20	S12S	TBM9
73G	AT72	BT36	CN7	DV1	GLAS	LS8	PA22	S20	TEST
73H	AT73	BU31	CNA	DV20	GLID	LS9	PA23	S205	TEX2
73S	AT75	BUSH	CNC	E110	GLST	LYNX	PA24	S208	TEXA
76W	AT76	BX2	COL	E120	GOLF	M10	PA25	S22T	TFUN
A109	AT8T	C06T	COL3	E200	GP4	M108	PA27	S25	TL20
A119	ATP	C10T	COL4	E300	GRND	M200	PA30	S2P	TL30
A139	ATR	C120	COUG	E314	GROU	M20P	PA31	S2T	TLEG
A140	AUS5	C130	COUR	E390	GUEP	M20T	PA32	S32M	TNDR
A169	AUS6	C140	COY2	E400	GX	M28	PA34	S330	TOBA
A189	AVID	C150	COZY	E500	GY20	M346	PA38	S450	TOUR
A210	AVTR	C152	CP10	EA30	GY80	M4	PA44	S58T	TRAL
A211	B06	C162	CP23	EAGL	GYRO	M5	PA46	S61	TRF1
A26	B06T	C170	CR10	EB29	H160	M6	PAG	S64	TRIM
A4	B105	C172	CRER	EC20	H25	M600	PAR1	S76	TRIN
A5	B14A	C175	CRUZ	EC25	H25X	M7	PAT	S76B	TRIS
A500	B17	C177	CT	EC30	H269	M82	PAT4	S92	TS1J
A748	B18T	C180	CT4	EC35	H40	MA5	PAY1	SAPH	TUCA
AA1	B190	C182	CTAH	EC45	H47	MA60	PAY2	SASP	TWEN
AA5	B209	C185	CVLP	EC55	H4AT	MAVR	PAY3	SAVG	TWST
AAT3	B212	C188	CVLT	EC75	H500	MC01	PAY4	SB20	U15
AAT4	B214	C190	D11	ECHO	H60	MC10	PC12	SB91	U21
AB18	B222	C195	D140	EDGE	HIGH	MCR1	PC21	SC01	UCLA

AB6	B23	C205	D150	EFOX	HN70	MCR4	PC6T	SC7	UF13
AC11	B24	C206	D18	EH10	HR10	MCRR	PC7	SCOU	UH1
AC4	B25	C207	D228	EL10	HR20	MD3R	PC9	SD4	UHEL
AC50	B26	C208	D250	EN28	HROC	MD60	PELI	SF25	UL45
AC68	B29	C210	D253	EN48	HUML	MESS	PETR	SF34	ULAC
AC6L	B300	C212	D28D	EPIC	HUSK	MF17	PIAE	SF36	V10
AC90	B350	C240	D28G	ER4	HYPR	MI8	PIAT	SF50	V22
AC95	B36T	C25A	D28T	ERCO	IL78	MIRA	PISI	SG92	VALI
ACAM	B407	C25B	D2SL	ERJ	IR23	MM16	PITA	SH09	VELO
ACR2	B412	C25C	D31	ESCP	ISPT	MM24	PIVI	SH33	VENT
AEST	B427	C25M	D328	EUPA	J2	MOR2	PK20	SH36	VEZE
AFOX	B429	C27J	D4	EV97	J3	MP02	PL2	SHIP	VIX
AG5B	B430	C28	D40	EVOT	J300	MR25	PNR2	SHRK	VL3
AKRO	B505	C295	D4SL	EVSS	J4	MS23	PNR3	SIRA	VNTR
ALGR	B58T	C303	D6CR	EXEC	J5	MSQ2	PNR4	SKAR	VR7
ALIG	B609	C30J	D6F	EXPL	JAB2	MT	PP2	SKRA	VTOR
ALO2	BALL	C310	D6SL	EXPR	JAB4	MU2	PP3	SLG2	VTRA
ALO3	BD4	C320	D9F	F15	JABI	MUS2	PRIM	SLG4	VTUR
ALSL	BDOG	C335	DA40	F16	JANU	MX1T	PRM1	SO5R	W3
ALTO	BE1	C336	DA42	F18H	JFOX	MX2	PTMS	SONX	WA40
AN12	BE10	C337	DA62	F22	JK05	NAVI	PTS1	SPIT	WA41
AN2	BE17	C340	DAL4	F260	JS31	NG4	PTS2	SR20	WA50
AN24	BE18	C402	DC3	F406	JS32	NG5	PULR	SR22	WACF
AN26	BE19	C404	DC6	F50	JS41	NH90	PULS	SREY	WILT
AN32	BE20	C411	DEFI	F8L	JUNR	NIMB	PUMA	SS2T	WT9
AP20	BE23	C414	DG15	FA04	KA27	NIPR	PUP	ST75	XA41
AP22	BE24	C42	DG1T	FA24	KFIR	NNJA	PZ4M	STAL	XA42
AP32	BE30	C421	DG40	FAET	KIS4	None	R100	STAR	XL2
APM2	BE33	C425	DG50	FALM	KL07	O1	R200	STCH	XNON
AR11	BE35	C441	DG80	FB5	KMAX	ONEX	R22	SUBA	Y12
AR15	BE36	C525	DH1	FBA2	KODI	OSCR	R300	SV4	Y18T
ARCP	BE50	C72R	DH2T	FDCT	KP2	P06T	R44	SVNH	YK11
ARV1	BE55	C77R	DH3	FK14	KP5	P149	R66	SW2	YK3
AS02	BE58	C82R	DH3T	FK9	KR30	P180	R90R	SW3	YK50
AS16	BE60	C82S	DH60	FM25	KT1	P208	RAF2	SW4	YK52
AS21	BE65	C82T	DH8	FOX	KZ7	P210	RALL	SWM	Z26
AS22	BE76	CA41	DH82	FURY	L10	P212	RANG	SX30	Z37P
AS25	BE77	CB1	DH87	G1	L188	P28A	RBEL	SYMP	Z42
AS26	BE80	CC19	DH89	G103	L200	P28B	RELI	T18	Z43
AS28	BE95	CCJ	DH8A	G109	L40	P28R	RF4	T206	ZEPH
AS29	BE99	CDUS	DH8B	G115	L410	P28S	RF5	T210	ZZZX
AS30	BE9L	CE43	DH8C	G120	L5	P28T	RF6	T214	ZZZZ
AS31	BE9T	CH2T	DH8D	G12T	L8	P28U	RODS	T28	

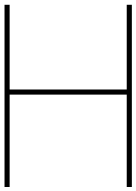

Global fuel consumption

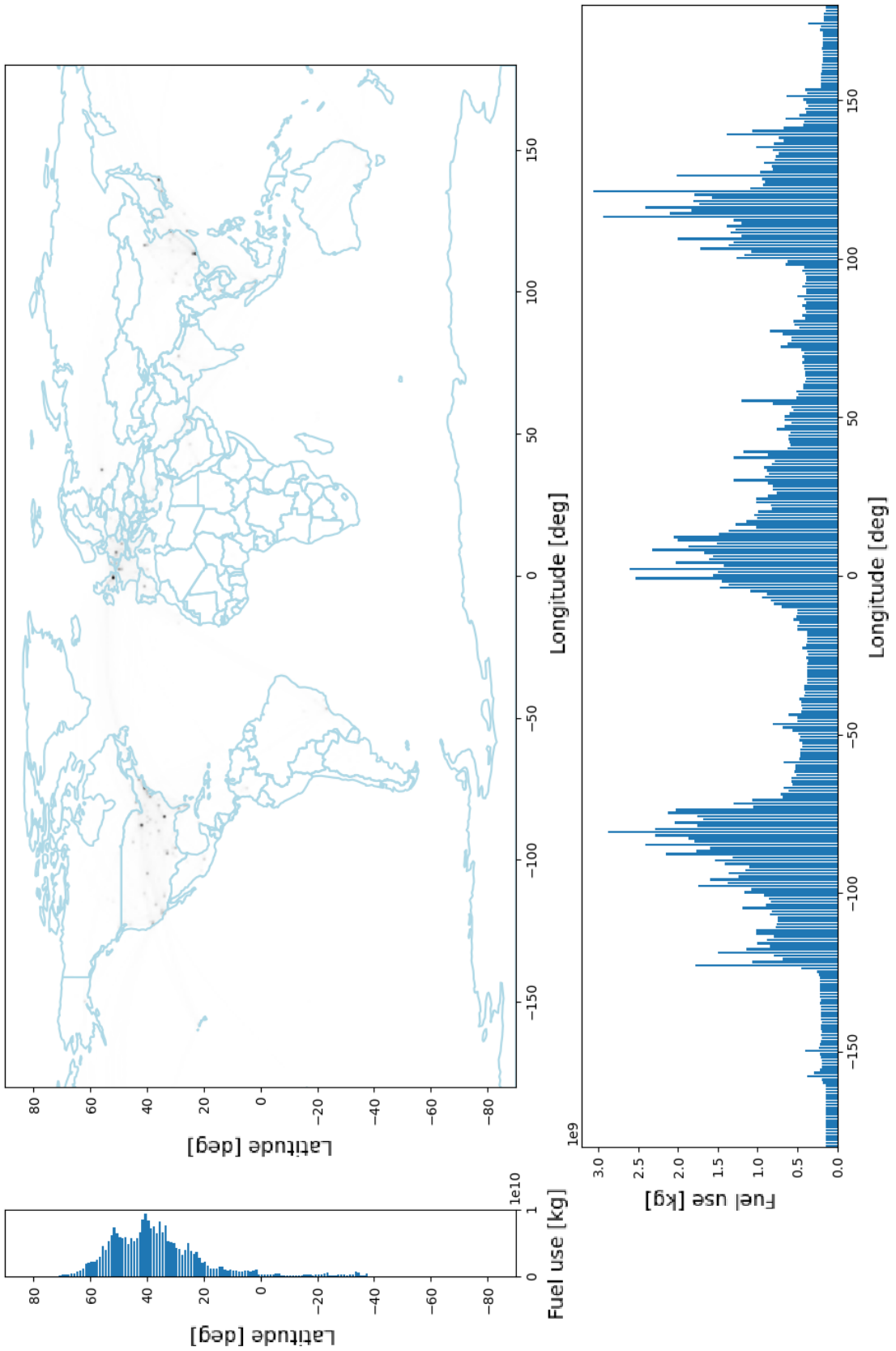

Figure H.1: Fuel consumption on a worldwide map also depicting the summation per longitude and latitude.

References

1. Lee, D. *et al.* The contribution of global aviation to anthropogenic climate forcing for 2000 to 2018. *Atmospheric Environment* **244,** 117834. ISSN: 1352-2310. doi:10.1016/j.atmosenv.2020.117834 (2021).
2. Árnadóttir, Á., Czepkiewicz, M. & Heinonen, J. Climate change concern and the desire to travel: How do I justify my flights? *Travel Behaviour and Society* **24,** 282–290. ISSN: 2214-367X. doi:10.1016/j.tbs.2021.05.002 (2021).
3. Matthes, S. *et al.* Mitigation of Non-CO2 Aviation's Climate Impact by Changing Cruise Altitudes. *Aerospace* **8.** ISSN: 2226-4310. doi:10.3390/aerospace8020036 (2021).
4. Simone, N. W. *Development of a Rapid Global Aircraft Emissions Estimation Tool with Uncertainty Quantification* in (2013).
5. Zhang, H. *et al.* Precipitation and nitrogen application stimulate soil nitrous oxide emission. *Nutrient Cycling in Agroecosystems* **120.** doi:10.1007/s10705-021-10155-4 (June 2021).
6. Gössling, S. & Humpe, A. The global scale, distribution and growth of aviation: Implications for climate change. *Global Environmental Change* **65,** 102194. ISSN: 0959-3780. doi:10.1016/j.gloenvcha.2020.102194 (2020).
7. Eyers, C. J. *et al. AERO2k Global Aviation Emissions Inventories for 2002 and 2025* (European Commission, 2004).
8. Baughcum, S. L., Tritz, T. G., Henderson, S. C. & Pickett, D. C. *Scheduled Civil Aircraft Emission Inventories for 1992: Database Development and Analysis* (NASA, 1996).
9. Fan, W., Sun, Y., Zhu, T. & Wen, Y. Emissions of HC, CO, NO_x, CO_2, and SO_2 from civil aviation in China in 2010. *Atmospheric Environment* **56,** 52–57. doi:10.1016/j.atmosenv.2012.03.052 (2012).
10. Wasiuk, D. K., Khan, M. A. H., Shallcross, D. E. & Lowenberg, M. H. A Commercial Aircraft Fuel Burn and Emissions Inventory for 2005–2011. *Atmosphere* **7.** doi:10.3390/atmos7060078 (2016).
11. Li, J. *et al.* Aircraft Emission Inventory and Characteristics of the Airport Cluster in the Guangdong–Hong Kong–Macao Greater Bay Area, China. *Atmosphere* **11.** doi:10.3390/atmos11040323 (2020).
12. Owen, B., Lee, D. S. & Lim, L. Flying into the Future: Aviation Emissions Scenarios to 2050. *Environmental Science & Technology* **44,** 2255–2260. doi:10.1021/es902530z (2010).
13. Jelinek, F., Carlier, S. & Smith, J. *The Advanced Emission Model (AEM3) - Validation Report - Appendices A, B and C* (Eurocontrol, 2004).
14. Lee, J. J. *Modeling aviation's global emissions, uncertainty analysis, and applications to policy* in (2005).
15. Waitz, I. A., Lukachko, S. P. & Lee, J. J. Military Aviation and the Environment: Historical Trends and Comparison to Civil Aviation. *Journal of Aircraft* **42,** 329–339. doi:10.2514/1.6888 (2005).
16. Spicer, C. W. *et al.* Rapid measurement of emissions from military aircraft turbine engines by downstream extractive sampling of aircraft on the ground: Results for C-130 and F-15 aircraft. *Atmospheric Environment* **43,** 2612–2622. doi:https://doi.org/10.1016/j.atmosenv.2009.02.012 (2009).
17. Kalagireva, K. & Radkov, V. Displaying the Air Situation through the Collection and Processing of Flight Information on Flightradar24 Project. **18,** 267–272. doi:10.19062/2247-3173.2016.18.1.36 (June 2016).

18. Sun, J. & Dedoussi, I. Evaluation of Aviation Emissions and Environmental Costs in Europe Using OpenSky and OpenAP. *Engineering Proceedings* **13.** doi:https://doi.org/10.3390/engproc2021013005 (2021).
19. Eurocontrol. *EUROCONTROL Data Snapshot* 2021.
20. Ghazi, G., Botez, R., Bourrely, C. & Turculet, A.-A. Method for Calculating Aircraft Flight Trajectories in Presence of Winds. *Journal of Aerospace Information Systems* **18.** doi:10.2514/1.I010879 (June 2021).
21. Duncan, J. *Pilot's Handbook of Aeronautical Knowledge* (United States Department of Transportation, Federal Aviation Administration and Airman Testing Standards Branch, AFS-630, P.O. Box 25082, Oklahoma City, OK 73125, 2016).
22. Sun, J., Hoekstra, J. M. & Ellerbroek, J. OpenAP: An Open-Source Aircraft Performance Model for Air Transportation Studies and Simulations. *Aerospace* **13.** doi:10.3390/AEROSPACE7080104 (2020).
23. Simone, N. W., Stettler, M. E. & Barrett, S. R. Rapid estimation of global civil aviation emissions with uncertainty quantification. *Transportation Research Part D: Transport and Environment* **25,** 33–41. ISSN: 1361-9209. doi:10.1016/j.trd.2013.07.001 (2013).
24. Norman, P. & Eyers, C. *AERO2k Flight Profiling and Fuel Determination Validation, Assumptions and Sensitivity* in (Sept. 2004).
25. Agency, E. E. U. A. S. *Introduction to the ICAO Engine Emissions Databank* 2021.
26. Centre, E. E. *Aircraft Performance Summary Tables for the Base of Aircraft Data (BADA)* (Eurocontrol, 1998).
27. Nuic, A., Poles, D. & Mouillet, V. BADA: An advanced aircraft performance model for present and future ATM systems. *International Journal of Adaptive Control and Signal Processing* **24,** 850–866 (2010).
28. Alishahi, N. *What is really Cost Index!* Aug. 2020. doi:10.13140/RG.2.2.26249.06241.
29. Bos, P. *Impact of Uncertainties on the Climate-Optimized Aircraft Design* in (2022).
30. Weaver, C. & Ramanathan, V. Deductions from a simple climate model: Factors governing surface temperature and atmospheric thermal structure. *Journal of Geophysical Research* **1001,** 11585–11592. doi:10.1029/95JD00770 (June 1995).
31. Dobruskin, V. *Impact of humanity on climate change* July 2022. doi:10.48550/arXiv.2207.13694.
32. Gorman, J. & Drisse, M.-N. Air pollution and child health: prescribing clean air (June 2019).
33. Bierwirth, P. *Carbon dioxide toxicity and climate change: a major unapprehended risk for human health* Mar. 2021.
34. Robertson, D. The rise in the atmospheric concentration of carbon dioxide and the effects on human health. *Medical hypotheses* **56,** 513–8. doi:10.1054/mehy.2000.1256 (May 2001).
35. Karnauskas, K., Miller, S. & Schapiro, A. Fossil Fuel Combustion Is Driving Indoor CO2 Toward Levels Harmful to Human Cognition. *GeoHealth* **4.** doi:10.1029/2019GH000237 (May 2020).
36. Pörtner, H.-O., Langenbuch, M. & Reipschläger, A. Biological Impact of Elevated Ocean CO2 Concentrations: Lessons from Animal Physiology and Earth History. *Journal of Oceanography* **60,** 705–718. doi:10.1007/s10872-004-5763-0 (Aug. 2004).
37. Ezraty, B., Chabalier, M., Ducret, A., Maisonneuve, E. & Dukan, S. CO2 exacerbates oxygen toxicity. *EMBO reports* **12,** 321–6. doi:10.1038/embor.2011.7 (Feb. 2011).
38. Mehta, P. Science behind Acid Rain: Analysis of Its Impacts and Advantages on Life and Heritage Structures. *S. Asian J. Tourism and Heritage* **3** (Jan. 2010).
39. Kusumaningtiar, D. & Vionalita, G. Air Pollution of Carbon Monoxide: a Case Study on City Traffic Jam. *Pollution Research* **39** (Dec. 2020).
40. Srivastava, M., Srivastava, A., Yadav, A. & Rawat, V. in (Feb. 2020). ISBN: 978-1-78984-421-4.

41. Boningari, T. & Smirniotis, P. G. Impact of nitrogen oxides on the environment and human health: Mn-based materials for the NOx abatement. *Current Opinion in Chemical Engineering* **13.** Energy and Environmental Engineering / Reaction engineering and catalysis, 133–141. ISSN: 2211-3398. doi:10.1016/j.coche.2016.09.004 (2016).
42. Vries, W. Impacts of nitrogen emissions on ecosystems and human health: A mini review. *Current Opinion in Environmental Science Health* **21,** 100249. doi:10.1016/j.coesh.2021.100249 (Mar. 2021).
43. Group, W. B. *Sulfur Oxides* 1998.
44. Held, I. & Soden, B. Water Vapor Feedback and Global Warming. *Annual Review of Energy and The Environment* **25,** 441–475. doi:10.1146/annurev.energy.25.1.441 (Nov. 2000).
45. Gierens, K., Lim, L. & Eleftheratos, K. A Review of Various Strategies for Contrail Avoidance. *The Open Atmospheric Science Journal* **2,** 1–7. doi:10.2174/1874282300802010001 (Feb. 2008).
46. Bond, T. *et al.* Bounding the role of black carbon in the climate system: A Scientific assessment. *Journal of Geophysical Research: Atmospheres* **118,** 5380–5552. doi:10.1002/jgrd.50171 (June 2013).
47. Bice, K. *et al. Black Carbon: A review and policy recommendations* (Jan. 2009).
48. Dallara, E., Kroo, I. & Waitz, I. Metric for Comparing Lifetime Average Climate Impact of Aircraft. *AIAA Journal* **49,** 1600–1613. doi:10.2514/1.J050763 (Aug. 2011).
49. Schaefer, M. *Methodologies for Aviation Emission Calculation - A comparison of alternative approaches towards 4D global inventories* PhD thesis (May 2006). doi:10.14279/depositonce-1476.
50. DuBois, D. & Paynter, G. C. "Fuel Flow Method2" for Estimating Aircraft Emissions. *SAE Transactions* **115,** 1–14. ISSN: 0096736X, 25771531 (2006).
51. The ignition, oxidation, and combustion of kerosene: A review of experimental and kinetic modeling. *Progress in Energy and Combustion Science* **32,** 48–92. ISSN: 0360-1285. doi:10.1016/j.pecs.2005.10.003 (2006).
52. Döpelheuer, A. Quantities, Characteristics and Reduction Potentials of Aircraft Engine Emissions. *SAE Technical Papers.* doi:10.4271/2001-01-3008 (Sept. 2001).
53. Schaefer, M. & Bartosch, S. *Overview on fuel flow correlation methods for the calculation of NOX, CO and HC emissions and their implementation into aircraft performance software* (DLR Institute of Propulsion Technology, 2013).
54. Sundberg, C.-M. & Forsberg, G. *Analysis of Aircraft Emissions Based on Flight Trajectory* (KTH Royal Institute of Technology, 2022).
55. A NOx Emissions Correlation for Modern RQL Combustors. *Energy Procedia* **75,** 2323–2330. ISSN: 1876-6102. doi:https://doi.org/10.1016/j.egypro.2015.07.433 (2015).
56. Electric, G. *GENX high bypass turbofan engines*
57. Schaefer, M. *Development of a Forecast Model for Global Air Traffic Emissions* PhD thesis (Aug. 2012).
58. Petzold, A., Döpelheuer, A., Brock, C. A. & Schröder, F. In situ observations and model calculations of black carbon emission by aircraft at cruise altitude. *Journal of Geophysical Research* **104,** 22171–22181. doi:10.1029/1999JD900460 (1999).
59. Agarwal, A. *et al.* SCOPE11 Method for Estimating Aircraft Black Carbon Mass and Particle Number Emissions. *Environmental Science Technology* **53.** doi:10.1021/acs.est.8b04060 (Jan. 2019).
60. Peck, J., Oluwole, O. O., Wong, H.-W. & Miake-Lye, R. C. An algorithm to estimate aircraft cruise black carbon emissions for use in developing a cruise emissions inventory. *Journal of the Air & Waste Management Association* **63,** 367–375. doi:10.1080/10962247.2012.751467 (2013).
61. Wayson, R., Fleming, G. G., Kim, B. Y. & Draper, J. A. *Derivation of a first order approximation of particulate matter from aircraft* 2003.

62. Wayson, R. L., Fleming, G. G. & Iovinelli, R. Methodology to Estimate Particulate Matter Emissions from Certified Commercial Aircraft Engines. *Journal of the Air & Waste Management Association* **59,** 91–100. doi:10.3155/1047-3289.59.1.91 (2009).
63. Zahavi, E., Burcat, A. & Gal, O. Effect of Future Jet Fuel Characteristics on Adiabatic Flame Temperatures and Combustion Products Distribution. *Journal of the Energy Institute* **55,** 28–40 (1982).
64. Dekking, F., Kraaikamp, C., Lopuhaä, H. & Meester, L. *A Modern Introduction to Probability and Statistics: Understanding Why and How* ISBN: 9781852338961 (Springer).
65. Verbist, M. *Gas path analysis for enhanced aero-engine condition monitoring and maintenance* PhD thesis (Delft University of Technology, 2017). ISBN: 978-94-6299-536-9. doi:10.4233/uuid:e1079009-84c2-482d-afe4-e1f9fde0d137.
66. *Effects of Engine Aging on Aircraft NOx Emissions* **1** (June 1997). doi:10.1115/97-GT-386.
67. Urban, L. A. Parameter Selection for Multiple Fault Diagnostics of Gas Turbine Engines. *Journal of Engineering for Power* **97,** 225–230. doi:10.1115/1.3445969 (Apr. 1975).
68. Hünecke, K. *Jet Engines: Fundamentals of Theory, Design, and Operation* ISBN: 9780760304594 (Motorbooks International, 1997).
69. Martins, D. A. R. *Off-Design Performance Prediction of the CFM 56-3 Aircraft Engine* in (2015).
70. Minculete, N. Types of Statistical Indicators Characterized by 2-Pre-Hilbert Spaces. *Symmetry* **12,** 1501. doi:10.3390/sym12091501 (Sept. 2020).
71. *Aviation Environmental Design Tool Version 2b Uncertainty Quantification Report* (Federal Aviation Administration, Aug. 2017).
72. *737 Airplane Characteristics for Airport Planning* (Boeing, Oct. 2021).
73. *A340-500/-600 Aircraft Characteristics Airport and Maintenance Planning* (Airbus, Dec. 2020).
74. Winther, M. & Rypdal, K. *EMEP/EEA air pollutant emission inventory guidebook 2019* 2019.
75. Rindlisbacher, T. & Jacob, S. D. *New Particulate Matter Standard for Aircraft Gas Turbine Engines* (ICAO).
76. *European Aviation Environmental Report 2022* (2022).
77. Baughcum, S. & Center, L. R. *Stratospheric Emissions Effects Database Development* (National Aeronautics and Space Administration, Langley Research Center, 1994).
78. Olsen, S., Wuebbles, D. & Owen, B. Comparison of global 3-D aviation emissions datasets. *Atmospheric Chemistry and Physics* **13.** doi:10.5194/acp-13-429-2013 (Jan. 2013).
79. Sutkus, J, D., Baughcum, S. & DuBois, D. Scheduled Civil Aircraft Emission Inventories for 1999: Database Development and Analysis (Nov. 2001).
80. Kim, B. *et al. System for Assessing Aviation's Global Emissions (SAGE), Version 1.5; Global Aviation Emissions Inventories for 2000 through 2004* (Federal Aviation Administration Office of Environment and Energy, 2005).
81. Wilkerson, J. T. *et al.* Analysis of emission data from global commercial aviation: 2004 and 2006. *Atmospheric Chemistry and Physics* **10,** 6391–6408. doi:10.5194/acp-10-6391-2010 (2010).
82. Kim, B. Y. *et al.* System for assessing Aviation's Global Emissions (SAGE), Part 1: Model description and inventory results. *Transportation Research Part D: Transport and Environment* **12,** 325–346. ISSN: 1361-9209. doi:10.1016/j.trd.2007.03.007 (2007).
83. Chèze, B., Gastineau, P. & Chevallier, J. Forecasting world and regional aviation jet fuel demands to the mid-term (2025). *Energy Policy* **39,** 5147–5158. ISSN: 0301-4215. doi:10.1016/j.enpol.2011.05.049 (2011).
84. Yan, F. *et al.* Global emission projections for the transportation sector using dynamic technology modeling. *Atmospheric Chemistry and Physics* **14,** 5709–5733. doi:10.5194/acp-14-5709-2014 (2014).

85. Sutkus, D., Baughcum, S. & DuBois, D. *Commercial Aircraft Emission Scenario for 2020: Database Development and Analysis* (National Aeronautics and Space Administration, Glenn Research Centre: Hanover, MD, USA, 2003).

86. Watson, R. *et al. Aviation and the Global Atmosphere* (1999).

87. *Fuel Tankering: economic benefits and environmental impact* 2019. https://www.eurocontrol.int/sites/default/files/2020-01/eurocontrol-think-paper-1-fuel-tankering.pdf.

88. *A320 Aircraft Characteristics Airport and Maintenance Planning* (Airbus, Dec. 2020).

89. *787 Airplane Characteristics for Airport Planning* (Boeing, Oct. 2021).